Materials Today Chemistry 49 (2025) 103023

Contents lists available at ScienceDirect

Materials Today Chemistry

journal homepage: www.journals.elsevier.com/materials-today-chemistry/

Roughness dependence of cross-plane interfacial phonon transport in multilayer films by discrete ordinates method

Xin Ran, Bingyang Cao *

Key Laboratory of Thermal Science and Power Engineering of Education of Ministry, Department of Engineering Mechanics, Tsinghua University, Beijing, China

ARTICLE INFO

Keywords:
Micro/nanoscale thermal transport
Interfacial phonon transport
Multilayer films
Interface roughness
Discrete ordinates method

ABSTRACT

Although multilayer films widely exist in micro/nanoelectronics and thermoelectrics, the underlying mechanisms of interfacial phonon transport in such structures remain elusive. The present work systematically investigates the impact of interface roughness on cross-plane interfacial phonon transport in multilayer films. To achieve this goal, the discrete ordinates method schemes for interface treatment considering spectral specularity and spectral transmissivity, and for cross-plane interfacial phonon transport across multilayer films are constructed, and validated against Landauer formalism, experiments and Monte Carlo method. Then they are applied into the investigation of roughness dependence of the cross-plane thermal conductivity and thermal boundary conductance in multilayer films. Considering the identical interface roughness for all interfaces, the cross-plane thermal conductivity is found to vary differently with interface roughness from bilayer films, attributed to the spectral feature of interface transmissivity. Considering the nonidentical interface roughness for all interfaces, the cross-plane thermal conductivity is found to be affected significantly differently by different interfaces, attributed to the spectral feature of interface transmissivity as well. And thus setting nonidentical interface roughness is proposed to more effectively manipulate the cross-plane thermal conductivity of multilayer films. For both identical and nonidentical interface roughnesses, it is found that the thermal boundary conductance of each interface varies significantly differently with the roughness of different interfaces. This phenomenon is explained by analyzing the spectral interface transmissivity and the interface scattering strengths along the same and opposite directions of heat flux.

1. Introduction

Phonon transport in multilayer films has attracted great attentions owing to its crucial role in the thermal management of micro/nanoelectronics and the optimization of thermoelectrics [1–3]. Increasing thermal conductivity is pursued to efficiently dissipate waste heat in electronics, whereas lowering thermal conductivity is desirable to enhance the performance of thermoelectrics [4,5]. In multilayer films, interfaces play an important role on affecting phonon transport by posing non-negligible thermal resistance, called thermal boundary resistance [2,6]. The mechanisms of interfacial phonon transport remain elusive at micro/nanoscale, where the classical law, Fourier's law, may fail [7]. Therefore, for highly efficient thermal management of micro/-nanoelectronics and further optimization of thermoelectrics, it is urgent to uncover more knowledge about interfacial phonon transport in multilayer films.

A phonon incident on the interface will either transmit across it or be reflected. The transmissivity is taken to quantify this process, defined as the probability of a phonon transmitting across the interface. Two classical interface models were developed to calculate the transmissivity, namely acoustic mismatch model (AMM) and diffuse mismatch model (DMM) [8,9]. AMM assumed the interface being completely smooth and the phonon as the plane wave being completely specularly scattered by the interface, more suitable at low temperatures [8]. DMM assumed the interface being completely diffuse and the phonon as the particle being completely diffusely scattered by the interface, working better at high temperatures [9]. AMM or DMM cannot accurately describe the interfacial phonon scatterings in real situations, where the interface is neither completely smooth nor completely diffuse. Accordingly mixed mismatch model (MMM) was developed to account for the partial specular and partial diffuse phonon scatterings at interfaces through introducing the specularity, the probability of the specular scattering, which was related to the interface roughness [10]. These interface models treated the specularity and

* Corresponding author.
E-mail address: caoby@tsinghua.edu.cn (B. Cao).

https://doi.org/10.1016/j.mtchem.2025.103023
Received 9 May 2025; Received in revised form 8 August 2025; Accepted 28 August 2025

transmissivity as the gray [8–10]. However, both experiments and theoretical calculations have demonstrated that the specularity and transmissivity strongly depend on the phonon frequency [11–13]. Thus many interface models for either spectral transmissivity or spectral specularity were developed, better predicting the measured thermal boundary conductance and transmissivity but not in accordance with the principle of detailed balance [14,15]. Recently, spectral mixed mismatch model (SMMM) was developed to account for both spectral specularity and spectral transmissivity, which also satisfied the principle of detailed balance [16]. Thereby the present work will adopt SMMM to quantify the interfacial phonon scatterings in multilayer films.

Previous studies have found that coherent and incoherent phonon transport exist in the small- and large-scale multilayer films, respectively [17–20]. Coherent phonon transport is dominated by phonon wave nature and results in increasing thermal conductivity with decreasing size of multilayer films [17–20]. On the contrary, incoherent phonon transport is dominated by phonon particle nature and results in decreasing thermal conductivity with decreasing size of multilayer films [17–20]. For incoherent phonon transport, the cross-plane thermal conductivity of superlattice was calculated using discrete ordinates method with the gray specularity and gray transmissivity, and monotonically decreased with increasing interface roughness, related to the specularity [10]. A theoretical model for the cross-plane thermal conductivity of superlattice was developed considering the gray specularity and gray transmissivity, which also gave the decreasing thermal conductivity with increasing interface roughness [21]. Thermal boundary conductance of trilayer films was calculated using molecular dynamics method and was found to strongly depend on the interface location [22]. Thermal boundary conductance of four-layer films was calculated using Monte Carlo method with the spectral transmissivity, showing a strong dependence on the interface location and thickness of films [23]. Besides, the cross-plane thermal conductivity of four-layer films was calculated using Monte Carlo method with the spectral transmissivity, and the results indicated that the thicknesses of the layers closest to the isothermal boundaries dominated the total thermal conductivity over other layers [24]. Totally, the previous works on multilayer films either considered the gray specularity and gray transmissivity, or considered the spectral transmissivity yet neglected the spectral feature of the specularity. However, as mentioned before, both specularity and transmissivity strongly depend on the phonon frequency [11–13]. Therefore, the present work will investigate the impact of interface roughness on incoherent cross-plane phonon transport in multilayer films considering the spectral specularity and spectral transmissivity.

There are many methods for studying interfacial phonon transport, mainly including microscopic methods [13,25,26], mesoscopic methods [27–33] and experiments [34]. Microscopic methods are suitable for small systems whereas their computational costs are high for large systems, containing molecular dynamics method [26], Green's function method [25] and lattice dynamics method [13], etc. It is difficult for experiments to analyze the detailed mechanisms in interfacial phonon transport. Based on directly solving phonon Boltzmann transport equation, mesoscopic methods are good at the study of large systems, containing deterministic method and Monte Carlo method (MC). MC solves phonon Boltzmann transport equation by random sampling techniques and easily handles complex geometries, whereas its noise error is large and its spectral analysis on heat flux or temperature is difficult [28,29,35]. Deterministic methods mainly contain discrete ordinates method (DOM) [27], lattice Boltzmann method (LBM) [32,33], and discrete unified gas kinetic scheme (DUGKS) [30,31], etc. Up to now, LBM fails to consider the real dispersions of phonons, and DUGKS is immature and under further developments for phonon transport, and both methods are difficult to consider the interface effect on phonon transport, especially with spectral transmissivity. Also as one of the deterministic methods, DOM is successful in considering real phonon dispersions of phonons and the interface effect, particularly with spectral transmissivity, and mature for phonon transport [29]. Additionally, although its handle for complex geometries is difficult, it has high accuracy and easily performs spectral analysis on both heat flux and temperature [29]. Since the multilayer films in the present work are not very complex, DOM is selected to investigate incoherent phonon transport in these structures. DOM for interfacial phonon transport was first developed with the gray specularity and gray transmissivity to study the impact of interface roughness on cross-plane interfacial phonon transport in superlattice [10]. Then the periodic heat flux boundary condition of DOM with completely diffuse interface scattering considering the gray transmissivity was developed to calculate the thermal conductivity of nanocomposite materials [36]. Subsequently the spectral transmissivity was considered in DOM with completely diffuse interface scattering in various films [27,37,38]. Hence it is necessary to develop DOM accounting for spectral specularity and spectral transmissivity to further study interfacial phonon transport.

Herein, this work aims to study the roughness dependence of cross-plane interfacial phonon transport in multilayer films using DOM with SMMM. The rest of this paper is organized as below: First, section 2 introduces the details for DOM, consisted of the theoretical basis, the DOM schemes for bilayer and multilayer films, and the interface treatment for the spectral specularity and spectral transmissivity; then, the numerical methods are validated in bilayer and multilayer films in section 3 through comparisons with Landauer formalism, experiments and MC; next, the detailed results and discussions are presented in section 4, containing the cross-plane thermal conductivity and thermal boundary conductance with the identical and nonidentical interface roughnesses; finally, the conclusions are remarked in section 5.

2. Numerical methods

In this section, the theoretical basis of DOM is introduced, and then the DOM scheme for cross-plane interfacial phonon transport in bilayer films is presented and that in multilayer films is constructed, and finally the DOM scheme for interface treatment with spectral specularity and spectral transmissivity is proposed.

2.1. Phonon Boltzmann transport equation

The phonon Boltzmann transport equation is given as below [39,40]

$$\frac{\partial f}{\partial t}+\mathbf{v}_g(\omega,\mathrm{p})\cdot\nabla f=\frac{\left(f^{\mathrm{pse}}-f^{\mathrm{ref}}\right)-f}{\tau(\omega,\mathrm{p},T)}, \tag{1}$$

where f and f^{pse} are the phonon distribution and Bose-Einstein distribution at pseudo-equilibrium temperature T^{pse}, respectively; $\mathbf{v}_g$ and τ are the group velocity and the relaxation time at phonon frequency ω and polarization p, respectively. After introducing the intensity $I=\hbar\omega f D(\omega,\mathrm{p})v_g(\omega,\mathrm{p})/4\pi$ and the pseudo-equilibrium intensity $I^{\mathrm{pse}}=\hbar\omega f^{\mathrm{pse}}D(\omega,\mathrm{p})v_g(\omega,\mathrm{p})/4\pi$, Eq. (1) is rewritten as [39,40]

$$\frac{\partial I}{\partial t}+\mathbf{v}_g(\omega,\mathrm{p})\cdot\nabla I=\frac{I^{\mathrm{pse}}-I}{\tau(\omega,\mathrm{p},T)}. \tag{2}$$

Eq. (2) is called equation of phonon radiative transfer, similar to equation of photon radiative transfer [39]. Further considering the deviational intensity $\Psi=I-I^{\mathrm{ref}}$ with the referenced equilibrium intensity $I^{\mathrm{ref}}=\hbar\omega f^{\mathrm{ref}}D(\omega,\mathrm{p})v_g(\omega,\mathrm{p})/4\pi$ and Bose-Einstein distribution f^{ref} at referenced equilibrium temperature T^{ref}, the deviational version of equation of phonon radiative transfer is given by [37,39,40]

$$\frac{\partial\Psi}{\partial t}+\mathbf{v}_g(\omega,\mathrm{p})\cdot\nabla\Psi=\frac{\left(I^{\mathrm{pse}}-I^{\mathrm{ref}}\right)-\Psi}{\tau(\omega,\mathrm{p},T)}. \tag{3}$$

The small temperature difference is considered throughout the system in the present work, with temperatures in the whole system close to the referenced temperature. With the deviational intensity, the temperature can be calculated through [37,39,40]

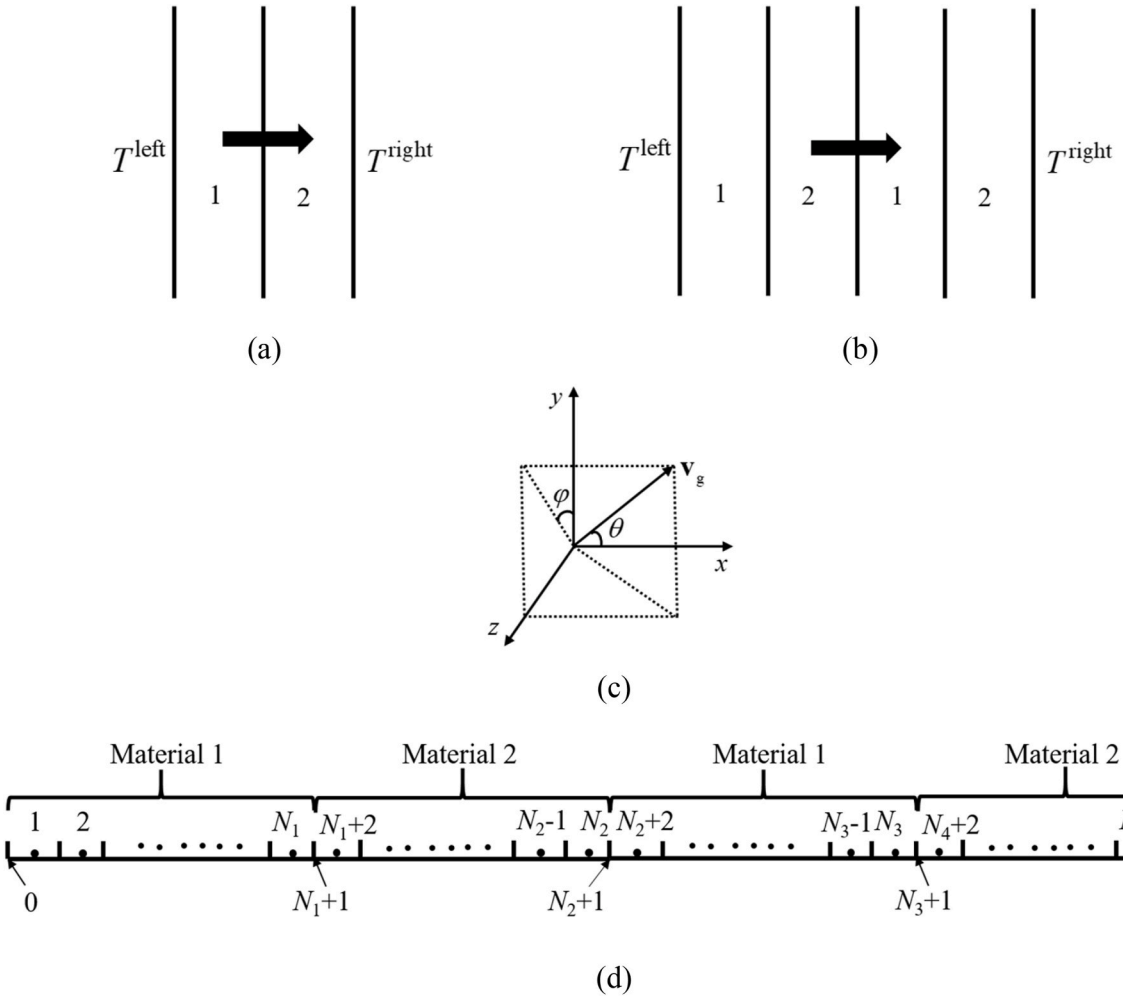

Fig. 1. The physical and numerical models in the present work: (a) the physical model of the bilayer film, (b) the physical model of the multilayer film, (c) the coordinate axis in the present work, and (d) the numerical model of the multilayer film. 1 and 2 are the material indexes; the direction of heat transport is along x axis, denoted by the black bold arrows; 0 and N_4+1 are the spatial indexes for the isothermal boundaries, and N_1+1, N_2+1, and N_3+1 are the spatial indexes for the first, second and third interfaces.

$$T_m = T^{\text{ref}} + \frac{1}{4\pi C_{V,m}} \sum_{\text{p}} \int_0^{4\pi} \int_0^{\omega_{\text{max,p},m}} \frac{\Psi}{v_{\text{g},m}} d\omega d\Omega, \tag{4}$$

and the pseudo-equilibrium temperature can be calculated through [37,39,40]

$$T_m^{\text{loc}} = T^{\text{ref}} + \frac{1}{4\pi C_{V,m}^{\text{loc}}} \sum_{\text{p}} \int_0^{4\pi} \int_0^{\omega_{\text{max,p},m}} \frac{\Psi}{v_{\text{g},m}\tau_m} d\omega d\Omega, \tag{5}$$

where $C_{V,m} = \sum_{\text{p}} \int_0^{\omega_{\text{max,p},m}} \hbar\omega f^{\text{ref}} D_m(\omega, \text{p}) d\omega$ and $C_{V,m}^{\text{loc}} = \sum_{\text{p}} \int_0^{\omega_{\text{max,p},m}} \frac{\hbar\omega f^{\text{ref}} D_m(\omega,\text{p})}{\tau_m} d\omega$; $d\Omega = \sin\theta d\theta d\varphi$ is the solid angle with the polar angle θ and azimuthal angle φ; m is the material index, represented by 1 or 2 in the present work. And the heat flux can be calculated through [37,39,40]

$$q = \sum_{\text{p}} \int_0^{4\pi} \int_0^{\omega_{\text{max,p},m}} \Psi \cos\theta d\omega d\Omega. \tag{6}$$

2.2. Discrete ordinates method schemes

Since the present work only concerns about the thermal properties around the referenced temperature, the one-dimensional cross-plane phonon transport at steady state is considered. The physical models in the present work are shown in Fig. 1(a) and (b), that is, bilayer and multilayer films with left and right boundaries fixed at temperatures T^{left} and T^{right}, respectively. For one-dimensional systems, Eq. (3) is rewritten as [37,39,40]

$$v_{\text{g}}(\omega, \text{p}) \cos\theta \frac{d\Psi}{dx} = \frac{\left(I^{\text{pse}} - I^{\text{ref}}\right) - \Psi}{\tau(\omega, \text{p}, T)}. \tag{7}$$

For convenience, Eq. (7) is rewritten as below after replacing $\cos\theta$ with μ:

$$v_{\text{g}}(\omega, \text{p}) \mu \frac{d\Psi}{dx} = \frac{\left(I^{\text{pse}} - I^{\text{ref}}\right) - \Psi}{\tau(\omega, \text{p}, T)}, \tag{8}$$

and Eqs. (4)–(6) are rewritten as [37,39,40]

$$T_m - T^{\text{ref}} = \frac{1}{2C_{V,m}} \sum_{\text{p}} \int_0^{\pi} \int_0^{\omega_{\text{max,p},m}} \frac{\Psi}{v_{\text{g,m}}} \sin\theta d\omega d\theta, \tag{9}$$

$$T_m^{\text{loc}} - T^{\text{ref}} = \frac{1}{2C_{V,m}^{\text{loc}}} \sum_{\text{p}} \int_0^{\pi} \int_0^{\omega_{\text{max,p},m}} \frac{\Psi}{v_{\text{g,m}}\tau_m} \sin\theta d\omega d\theta, \tag{10}$$

$$q = 2\pi \sum_{\text{p}} \int_0^{\pi} \int_0^{\omega_{\text{max,p},m}} \Psi \sin\theta \cos\theta d\omega d\theta. \tag{11}$$

Referred to Ref. [10,37], the emitted phonon temperatures are

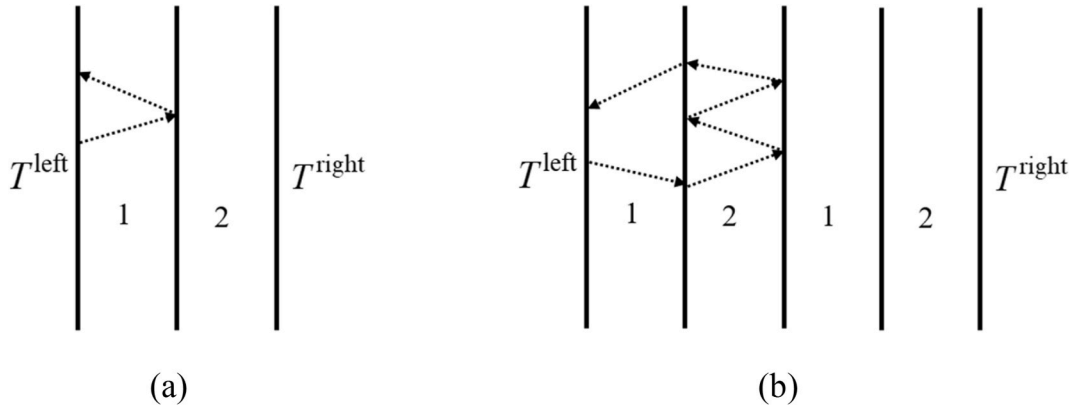

Fig. 2. The schematic diagrams of the interface scattering in two structures: (a) the bilayer film and (b) the multilayer film. The single-interface coupling scattering exists in the bilayer film and the multi-interface coupling scattering exists in the multilayer film. The black dashed arrows in (a) and (b) represent the motion trajectory of a phonon in the bilayer and multilayer films, respectively.

introduced as below for the comparison of thermal boundary conductance with Landauer formalism in bilayer films in Fig. 1 (a):

$$\begin{aligned}
&\sum_{\mathrm{p}}\int_0^{\omega_{\max,\mathrm{p},1}}\int_0^{2\pi}\int_0^{\frac{\pi}{2}}\alpha_{12}(\Psi_1)^{+}\cos\theta\sin\theta d\omega d\theta d\varphi \\
&=\sum_{\mathrm{p}}\int_0^{\omega_{\max,\mathrm{p},1}}\int_0^{2\pi}\int_0^{\frac{\pi}{2}}\frac{\hbar\omega\left(f^{\mathrm{eq}}\left(T_1^{\mathrm{e}}\right)-f^{\mathrm{ref}}\left(T^{\mathrm{ref}}\right)\right)D_1(\omega,\mathrm{p})v_{\mathrm{g},1}\alpha_{12}\cos\theta\sin\theta}{4\pi}d\omega d\theta d\varphi \\
&\simeq\sum_{\mathrm{p}}\int_0^{\omega_{\max,\mathrm{p},1}}\int_0^{2\pi}\int_0^{\frac{\pi}{2}}\frac{\left(T_1^{\mathrm{e}}-T^{\mathrm{ref}}\right)C_{\omega,\mathrm{p},1}v_{\mathrm{g},1}\alpha_{12}\cos\theta\sin\theta}{4\pi}d\omega d\theta d\varphi,
\end{aligned} \tag{12}$$

$$\begin{aligned}
&\sum_{\mathrm{p}}\int_0^{\omega_{\max,\mathrm{p},2}}\int_0^{2\pi}\int_{\frac{\pi}{2}}^{\pi}\alpha_{21}(\Psi_2)^{-}\cos\theta\sin\theta d\omega d\theta d\varphi \\
&=\sum_{\mathrm{p}}\int_0^{\omega_{\max,\mathrm{p},2}}\int_0^{2\pi}\int_{\frac{\pi}{2}}^{\pi}\frac{\hbar\omega\left(f^{\mathrm{eq}}\left(T_2^{\mathrm{e}}\right)-f^{\mathrm{ref}}\left(T^{\mathrm{ref}}\right)\right)D_2(\omega,\mathrm{p})v_{\mathrm{g},2}\alpha_{21}\cos\theta\sin\theta}{4\pi}d\omega d\theta d\varphi \\
&\simeq\sum_{\mathrm{p}}\int_0^{\omega_{\max,\mathrm{p},2}}\int_0^{2\pi}\int_{\frac{\pi}{2}}^{\pi}\frac{\left(T_2^{\mathrm{e}}-T^{\mathrm{ref}}\right)C_{\omega,\mathrm{p},2}v_{\mathrm{g},2}\alpha_{21}\cos\theta\sin\theta}{4\pi}d\omega d\theta d\varphi,
\end{aligned} \tag{13}$$

where T_1^{e} and T_2^{e} are the emitted phonon temperatures in materials 1 and 2 at the interface, respectively; α_{12} and α_{21} are the transmissivities from material 1 to 2 and in the reverse direction; $C_{\omega,\mathrm{p},1}=\hbar\omega D_1(\omega,\mathrm{p})\frac{df}{dT}\Big|_{T^{\mathrm{ref}}}$ and $C_{\omega,\mathrm{p},2}=\hbar\omega D_2(\omega,\mathrm{p})\frac{df}{dT}\Big|_{T^{\mathrm{ref}}}$ are the spectral heat capacities of materials 1 and 2. Simplifying and organizing Eqs. (12) and (13) in one-dimensional cross-plane phonon transport, the emitted phonon temperatures are calculated by [10,37]

$$T_1^{\mathrm{e}}=T^{\mathrm{ref}}+\frac{\sum_{\mathrm{p}}\int_0^{\omega_{\max,\mathrm{p},1}}\int_0^{\frac{\pi}{2}}(\Psi_1)^{+}\alpha_{12}\cos\theta\sin\theta d\omega d\theta}{\sum_{\mathrm{p}}\int_0^{\omega_{\max,\mathrm{p},1}}\int_0^{\frac{\pi}{2}}\frac{C_{\omega,\mathrm{p},1}v_{\mathrm{g},1}\alpha_{12}\cos\theta\sin\theta}{4\pi}d\omega d\theta}, \tag{14}$$

$$T_2^{\mathrm{e}}=T^{\mathrm{ref}}+\frac{\sum_{\mathrm{p}}\int_0^{\omega_{\max,\mathrm{p},2}}\int_{\frac{\pi}{2}}^{\pi}(\Psi_2)^{-}\alpha_{21}\cos\theta\sin\theta d\omega d\theta}{\sum_{\mathrm{p}}\int_0^{\omega_{\max,\mathrm{p},2}}\int_{\frac{\pi}{2}}^{\pi}\frac{C_{\omega,\mathrm{p},2}v_{\mathrm{g},2}\alpha_{21}\cos\theta\sin\theta}{4\pi}d\omega d\theta}. \tag{15}$$

It should be stated that the emitted phonon temperature is different from the commonly used temperature, i.e. the equivalent temperature, with their differences to be introduced later.

In DOM scheme, Eq. (7) is first discretized into a group of individual differential equations at each discrete angle, and then these differential equations are approximated by a group of difference equations using finite difference method. Solving these difference equations with iterative calculations, the deviational intensity can be approximately obtained and thus the temperature, pseudo-equilibrium temperature and

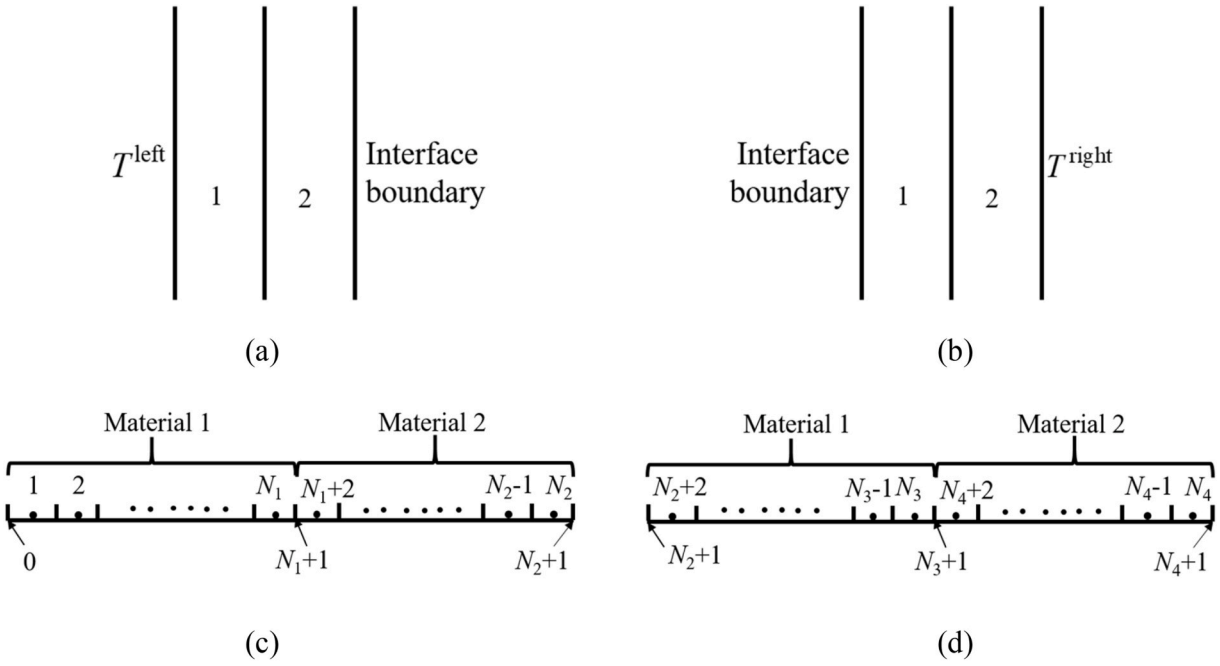

Fig. 3. The physical and numerical models of two bilayer films obtained by separating the multilayer film at the middle interface: (a) the bilayer film with the left isothermal and right interface boundaries, (b) the bilayer film with the right isothermal and left interface boundaries, (c) the numerical model for the bilayer film with the left isothermal and right interface boundaries, and (d) the numerical model for the bilayer film with the right isothermal and left interface boundaries. N_2+1 in (c) and (d) denote the right and left interface boundaries, respectively.

heat flux are all obtained based on Eqs. (9)–(11). The rest of subsection 2.2 will introduce the DOM schemes for bilayer and multilayer films, respectively.

2.2.1. *Bilayer films*

The DOM scheme for cross-plane interfacial phonon transport in bilayer films is similar to the previous schemes [27,41]. Its implementations are referred to those in Refs. [27,41] and briefly introduced as follows. This scheme mainly contains four implementations, including intensity calculation of inner spatial points, boundary treatment, interface treatment and macroscopic variable calculation. For bilayer films in the present work, only the isothermal boundary condition is considered, and the interface treatment is based on SMMM to first consider the spectral specularity and spectral transmissivity, with the detailed implementations to be introduced in subsection 2.3. In the simulation, the deviational intensities are first emitted from the boundaries and calculated towards the interface point by point in space. The interface treatment is implemented when the spatial points reach the interface. After the interface treatment, the deviational intensities are then calculated from the interface to the boundaries point by point in space. Since only a single interface exists, the intensity calculation in the bilayer film is simple and unidirectional, i.e. from the isothermal boundary to the interface and then from the interface to the isothermal boundary. Totally, the detailed simulation steps for the bilayer film are as follows: (1) Initialize the deviational and pseudo-equilibrium deviational intensities at all spatial points. (2) Starting from the left and right isothermal boundaries, update the deviational intensities from the boundaries to the interface point by point in space. (3) When the spatial points reach the middle interface, implement the interface treatment at the interface. (4) After the interface treatment, update the deviational intensities from the interface to the left and right isothermal boundaries. (5) Calculate the macroscopic information, i.e. temperature, pseudo-equilibrium temperature and heat flux distributions. (7) After obtaining the macroscopic information, verify whether the temperature and heat flux distributions converge. If they converge, output the calculation results. Otherwise, carry out the next iterative calculation of the temperature and pseudo-equilibrium temperature distributions with the updated temperature and pseudo-equilibrium temperature, until the temperatures and heat fluxes converge. The bilayer film is adopted to validate the interface treatment with spectral specularity and spectral transmissivity in the present work.

2.2.2. *Multilayer films*

Subsection 2.2.2 develops the numerical scheme of DOM for interfacial phonon transport in multilayer films in Fig. 1 (b). Different from the bilayer film, the simulation of cross-plane interfacial phonon transport in the multilayer film is challenging owing to the multi-interface coupling scattering by the multiple interfaces. Particularly, for the multilayer film in Fig. 2 (b), the deviational intensities are first calculated from the boundaries to the interfaces point by point in space. When the spatial points reach the first and third interfaces, the interface treatments at the first and third interfaces are implemented. After these interface treatments, some phonons are reflected and the corresponding deviational intensities are calculated from the first and third interfaces back to the boundaries. Other phonons transmit across the interfaces and the corresponding deviational intensities are calculated from the first and third interfaces to the second interface. For these phonons, when the spatial points reach the second interface, the interface treatment is implemented at the second interface. After the interface treatment, some phonons are reflected and others transmit across the second interface. The reflected phonons on the left side of the second interface and the transmitted phonons from the right to the left of the second interface continue to transport towards the first interface. And the corresponding deviational intensities are calculated from the second interface to the first interface. The transmitted phonons from the left to the right of the second interface and the reflected phonons on the right side of the second interface continue to transport towards the third interface. And the corresponding deviational intensities are calculated from the second interface to the third interface. After the above implementations, when the spatial points reach the first and third interfaces, the interface treatments are implemented at the first and third interfaces again. Then the deviational intensities are calculated from the first and

third interfaces to the boundaries and the second interface. The above process is repeated and never terminated. It makes simulating cross-plane interfacial phonon transport in multilayer films with DOM very complicated. In brief, the intensity calculation in multilayer films is complex and multidirectional, and the deviational intensity is calculated between boundaries and interfaces or between interfaces repeatedly. The multi-interface coupling scattering makes the intensity calculation at each spatial point complicated and difficult in multilayer films. Whereas for the bilayer film in Fig. 2 (a), the deviational intensities are first calculated from the boundaries to the interface point by point in space. When the spatial points reach the interface, the interface treatment is implemented. Then the deviational intensities are calculated from the interface to the boundaries point by point in space. The above process is simple and unidirectional, and easy to implemented, that is, from the boundaries to the interface and then from the interface to the boundaries. There is no multi-interface coupling scattering to make the intensity calculation complicated and difficult at each spatial point in bilayer films.

Referred to the computational characteristics of bilayer films, it is proposed in the present work to divide the multilayer film into two films to address the challenge in multilayer films caused by the multi-interface coupling scattering. Two bilayer films appears after separating the multilayer film at the middle interface, shown in Fig. 3(a) and (b). Their boundary conditions are given as the left and right boundaries being the isothermal and interface boundaries, respectively, or the left and right boundaries being the interface and isothermal boundaries, respectively. Their interface boundary conditions are equivalent to the deviational intensities at the second interface of the multilayer film. The advantage of dividing the multilayer film into two bilayer films is that it utilizes the computational characteristics of bilayer films, which is simple and unidirectional owing to the absence of the multi-interface coupling scattering. Yet it also introduces another issue, that is, the interface boundary conditions are unknown beforehand. To solve this issue, the present work adopts the iterative calculation to determine the interface boundary conditions of two bilayer films approximately. The concrete steps are as follows: First, assume two initial interface boundary conditions; secondly, in each bilayer film, the deviational intensities are calculated from the isothermal and interface boundaries to the middle interface point by point in space based on the temperature and pseudo-equilibrium temperature distributions; then, when the spatial points reach the middle interfaces, the interface treatments are implemented at the middle interfaces; next, after the interface treatments, the deviational intensities are calculated from the middle interfaces to the isothermal and interface boundaries; finally, for the deviational intensities reaching the interface boundaries, the interface treatment is implemented and two interface boundary conditions are updated simultaneously based on this treatment. Although these steps can only determine the approximate interface boundary conditions, these conditions can be considered as the sufficiently accurate results when the interface boundary conditions in two adjacent iterations are close enough after the sufficient iteration calculations. It should be noted that the adopted temperature and pseudo-equilibrium temperature distributions are known in advance in these steps, obtained through another iterative calculation. Since they are different in each step in this another iterative calculation, the above iterative calculation for interface boundary conditions can only determine the approximate values under the adoptedtemperature and pseudo-equilibrium temperature distributions in the current step. When the temperature and pseudo-equilibrium temperature distributions are changed in their iterative calculation, the adopted temperature and pseudo-equilibrium temperature distributions in the iterative calculation for interface boundary conditions need be updated correspondingly. Totally, in the present DOM scheme, two types of the iterative calculation should be introduced, that is, the ones for the interface boundary conditions and for the temperature and pseudo-equilibrium temperature distributions.

Based on the above analyses, the present numerical scheme of DOM for multilayer films also mainly contains four implementations, including the intensity calculation of inner spatial points, the boundary treatment, the interface treatment and the macroscopic variable calculation, introduced as follows:

First, for the intensity calculation of inner spatial points, the backward difference scheme is applied to approximate the spatial differential term in Eq. (8) at $\mu_j \geq 0$, and the corresponding difference equations in materials 1 and 2 are obtained [42]:

$$v_{g,1}(\omega_s,\mathrm{p})\mu_j\frac{\Psi_{s,\mathrm{p},i,j}-\Psi_{s,\mathrm{p},i-1,j}}{\Delta x}=\frac{\left(I^{\mathrm{pse}}_{s,\mathrm{p},i,j}-I^{\mathrm{ref}}_{s,\mathrm{p},i,j}\right)-\Psi_{s,\mathrm{p},i,j}}{\tau_1\left(\omega_s,\mathrm{p},T^{\mathrm{ref}}\right)}, \tag{16}$$

$$v_{g,2}(\omega_s,\mathrm{p})\mu_j\frac{\Psi_{s,\mathrm{p},i,j}-\Psi_{s,\mathrm{p},i-1,j}}{\Delta x}=\frac{\left(I^{\mathrm{pse}}_{s,\mathrm{p},i,j}-I^{\mathrm{ref}}_{s,\mathrm{p},i,j}\right)-\Psi_{s,\mathrm{p},i,j}}{\tau_2\left(\omega_s,\mathrm{p},T^{\mathrm{ref}}\right)}, \tag{17}$$

where i, j and s are the indexes for discrete spatial, angular and frequency points, respectively; Δx is the spatial step. Organizing Eqs. (16) and (17), two equations calculating the intensity of the present spatial points for $\mu_j \geq 0$ in materials 1 and 2 are obtained as below:

$$\Psi_{s,\mathrm{p},i,j}=\frac{\frac{1}{\tau_1\left(\omega_s,\mathrm{p},T^{\mathrm{ref}}\right)}\left(I^{\mathrm{pse}}_{s,\mathrm{p},i,j}-I^{\mathrm{ref}}_{s,\mathrm{p},i,j}\right)+\frac{v_{g,1}(\omega_s,\mathrm{p})\mu_j}{\Delta x}\Psi_{s,\mathrm{p},i-1,j}}{\left(\frac{v_{g,1}(\omega_s,\mathrm{p})\mu_j}{\Delta x}+\frac{1}{\tau_1\left(\omega_s,\mathrm{p},T^{\mathrm{ref}}\right)}\right)}, \tag{18}$$

$$\Psi_{s,\mathrm{p},i,j}=\frac{\frac{1}{\tau_2\left(\omega_s,\mathrm{p},T^{\mathrm{ref}}\right)}\left(I^{\mathrm{pse}}_{s,\mathrm{p},i,j}-I^{\mathrm{ref}}_{s,\mathrm{p},i,j}\right)+\frac{v_{g,2}(\omega_s,\mathrm{p})\mu_j}{\Delta x}\Psi_{s,\mathrm{p},i-1,j}}{\left(\frac{v_{g,2}(\omega_s,\mathrm{p})\mu_j}{\Delta x}+\frac{1}{\tau_2\left(\omega_s,\mathrm{p},T^{\mathrm{ref}}\right)}\right)}. \tag{19}$$

And the forward difference scheme is applied to approximate the spatial differential term in Eq. (8) at $\mu_j < 0$, and the corresponding difference equations in materials 1 and 2 are also obtained [42]:

$$v_{g,1}(\omega_s,\mathrm{p})\mu_j\frac{\Psi_{s,\mathrm{p},i+1,j}-\Psi_{s,\mathrm{p},i,j}}{\Delta x}=\frac{\left(I^{\mathrm{pse}}_{s,\mathrm{p},i,j}-I^{\mathrm{ref}}_{s,\mathrm{p},i,j}\right)-\Psi_{s,\mathrm{p},i,j}}{\tau_1\left(\omega_s,\mathrm{p},T^{\mathrm{ref}}\right)}, \tag{20}$$

$$v_{g,2}(\omega_s,\mathrm{p})\mu_j\frac{\Psi_{s,\mathrm{p},i+1,j}-\Psi_{s,\mathrm{p},i,j}}{\Delta x}=\frac{\left(I^{\mathrm{pse}}_{s,\mathrm{p},i,j}-I^{\mathrm{ref}}_{s,\mathrm{p},i,j}\right)-\Psi_{s,\mathrm{p},i,j}}{\tau_2\left(\omega_s,\mathrm{p},T^{\mathrm{ref}}\right)}. \tag{21}$$

Similarly, the equations calculating the intensity of the present spatial points for $\mu_j < 0$ in materials 1 and 2 are also obtained as below:

$$\Psi_{s,\mathrm{p},i,j}=\frac{\frac{1}{\tau_1\left(\omega_s,\mathrm{p},T^{\mathrm{ref}}\right)}\left(I^{\mathrm{pse}}_{s,\mathrm{p},i,j}-I^{\mathrm{ref}}_{s,\mathrm{p},i,j}\right)-\frac{v_{g,1}(\omega_s,\mathrm{p})\mu_j}{\Delta x}\Psi_{s,\mathrm{p},i+1,j}}{\left(-\frac{v_{g,1}(\omega_s,\mathrm{p})\mu_j}{\Delta x}+\frac{1}{\tau_1\left(\omega_s,\mathrm{p},T^{\mathrm{ref}}\right)}\right)}, \tag{22}$$

$$\Psi_{s,\mathrm{p},i,j}=\frac{\frac{1}{\tau_2\left(\omega_s,\mathrm{p},T^{\mathrm{ref}}\right)}\left(I^{\mathrm{pse}}_{s,\mathrm{p},i,j}-I^{\mathrm{ref}}_{s,\mathrm{p},i,j}\right)-\frac{v_{g,2}(\omega_s,\mathrm{p})\mu_j}{\Delta x}\Psi_{s,\mathrm{p},i+1,j}}{\left(-\frac{v_{g,2}(\omega_s,\mathrm{p})\mu_j}{\Delta x}+\frac{1}{\tau_2\left(\omega_s,\mathrm{p},T^{\mathrm{ref}}\right)}\right)}. \tag{23}$$

Secondly, for the boundary treatment, the isothermal and interface boundary conditions are considered in the present work. The isothermal boundary condition is implemented with a small temperature difference between two boundaries and analogous to the black body for photon radiation, obeying Lambert's cosine law. The intensities emitted from two isothermal boundaries are isotropic in all directions, directly dependent on the boundary temperatures as below:

$$\Psi_{s,\mathrm{p},0,j}=I^{\mathrm{left}}_{s,\mathrm{p}}-I^{\mathrm{ref}}_{s,\mathrm{p}}=\hbar\omega_s\left(f^{\mathrm{left}}-f^{\mathrm{ref}}\right)D_1(\omega_s,\mathrm{p})v_{g,1}(\omega_s,\mathrm{p})\Big/4\pi, \tag{24}$$

$$\Psi_{s,\mathrm{p},N_4+1,j}=I^{\mathrm{right}}_{s,\mathrm{p}}-I^{\mathrm{ref}}_{s,\mathrm{p}}=\hbar\omega_s\left(f^{\mathrm{right}}-f^{\mathrm{ref}}\right)D_2(\omega_s,\mathrm{p})v_{g,2}(\omega_s,\mathrm{p})\Big/4\pi, \tag{25}$$

where $I_{s,\mathrm{p}}^{\mathrm{left}}$ and $I_{s,\mathrm{p}}^{\mathrm{right}}$ are the equilibrium phonon intensities on left and right boundaries with Bose-Einstein distribution f^{left} and f^{right} at temperatures T^{left} and T^{right}, respectively; μ_j are larger and smaller than 0 for left and right boundaries, respectively. With the small temperature difference along the film, Eqs. (24) and (25) can be further linearized as below:

$$\Psi_{s,\mathrm{p},0,j} = \left(T^{\mathrm{left}} - T^{\mathrm{ref}}\right) C_{s,1} v_{\mathrm{g},1}(\omega_s, \mathrm{p})/4\pi, \tag{26}$$

$$\Psi_{s,\mathrm{p},N_4+1,j} = \left(T^{\mathrm{right}} - T^{\mathrm{ref}}\right) C_{s,2} v_{\mathrm{g},2}(\omega_s, \mathrm{p})/4\pi. \tag{27}$$

After obtaining the intensities emitted from two isothermal boundaries, the intensities of the first and last inner spatial points are obtained based on Eq. (8) using the backward and forward difference schemes with spatial step $\Delta x/2$, respectively [42]:

$$2v_{\mathrm{g},1}(\omega_s, \mathrm{p})\mu_j \frac{\Psi_{s,\mathrm{p},1,j} - \Psi_{s,\mathrm{p},0,j}}{\Delta x} = \frac{\left(I_{s,\mathrm{p},1,j}^{\mathrm{pse}} - I_{s,\mathrm{p},1,j}^{\mathrm{ref}}\right) - \Psi_{s,\mathrm{p},1,j}}{\tau_1\left(\omega_s, \mathrm{p}, T^{\mathrm{ref}}\right)}, \tag{28}$$

$$2v_{\mathrm{g},2}(\omega_s, \mathrm{p})\mu_j \frac{\Psi_{s,\mathrm{p},N_4+1,j} - \Psi_{s,\mathrm{p},N_4,j}}{\Delta x} = \frac{\left(I_{s,\mathrm{p},N_4,j}^{\mathrm{pse}} - I_{s,\mathrm{p},N_4,j}^{\mathrm{ref}}\right) - \Psi_{s,\mathrm{p},N_4,j}}{\tau_2\left(\omega_s, \mathrm{p}, T^{\mathrm{ref}}\right)}. \tag{29}$$

Organizing Eqs. (28) and (29), the equations calculating the intensity of the first and last spatial points for $\mu_j \geq 0$ and $\mu_j < 0$ are obtained as below:

$$\Psi_{s,\mathrm{p},1,j} = \frac{\frac{1}{\tau_1\left(\omega_s,\mathrm{p},T^{\mathrm{ref}}\right)}\left(I_{s,\mathrm{p},1,j}^{\mathrm{pse}} - I_{s,\mathrm{p},1,j}^{\mathrm{ref}}\right) + \frac{2v_{\mathrm{g},1}(\omega_s,\mathrm{p})\mu_j}{\Delta x}\Psi_{s,\mathrm{p},0,j}}{\left(\frac{2v_{\mathrm{g},1}(\omega_s,\mathrm{p})\mu_j}{\Delta x} + \frac{1}{\tau_1\left(\omega_s,\mathrm{p},T^{\mathrm{ref}}\right)}\right)}, \tag{30}$$

$$\Psi_{s,\mathrm{p},N_4,j} = \frac{\frac{1}{\tau_2\left(\omega_s,\mathrm{p},T^{\mathrm{ref}}\right)}\left(I_{s,\mathrm{p},N_4,j}^{\mathrm{pse}} - I_{s,\mathrm{p},N_4,j}^{\mathrm{ref}}\right) - \frac{2v_{\mathrm{g},2}(\omega_s,\mathrm{p})\mu_j}{\Delta x}\Psi_{s,\mathrm{p},N_4+1,j}}{\left(-\frac{2v_{\mathrm{g},2}(\omega_s,\mathrm{p})\mu_j}{\Delta x} + \frac{1}{\tau_2\left(\omega_s,\mathrm{p},T^{\mathrm{ref}}\right)}\right)}. \tag{31}$$

The interface boundary condition in the present work is based on SMMM, and thus the spectral specularity and spectral transmissivity are introduced into DOM scheme for the first time. The detailed implementations to give the outgoing intensities from the interface are presented based on the interface treatment in subsection 2.3. The calculations of the incoming intensities to the interface boundary and the intensities from the interface boundary to the nearest inner points are provided here. In Fig. 3 (c), the incoming intensity to the interface boundary is corresponding to $\mu_j \geq 0$, obtained using the backward difference scheme with spatial step $\Delta x/2$ [42]:

$$2v_{\mathrm{g},2}(\omega_s, \mathrm{p})\mu_j \frac{\Psi_{s,\mathrm{p},N_2+1,j} - \Psi_{s,\mathrm{p},N_2,j}}{\Delta x} = \frac{\left(I_{s,\mathrm{p},N_2,j}^{\mathrm{pse}} - I_{s,\mathrm{p},N_2,j}^{\mathrm{ref}}\right) - \Psi_{s,\mathrm{p},N_2,j}}{\tau_2\left(\omega_s, \mathrm{p}, T^{\mathrm{ref}}\right)}. \tag{32}$$

Organizing Eq. (32), the equation calculating the incoming intensity to the interface boundary in Fig. 3 (c) is obtained as below:

$$\Psi_{s,\mathrm{p},N_2+1,j} = \frac{\frac{1}{\tau_2\left(\omega_s,\mathrm{p},T^{\mathrm{ref}}\right)}\left(I_{s,\mathrm{p},N_2,j}^{\mathrm{pse}} - I_{s,\mathrm{p},N_2,j}^{\mathrm{ref}}\right)}{+\left(\frac{2v_{\mathrm{g},2}(\omega_s,\mathrm{p})\mu_j}{\Delta x} - \frac{1}{\tau_2\left(\omega_s,\mathrm{p},T^{\mathrm{ref}}\right)}\right)\Psi_{s,\mathrm{p},N_2,j}\frac{2v_{\mathrm{g},2}(\omega_s,\mathrm{p})\mu_j}{\Delta x}}. \tag{33}$$

In Fig. 3 (d), the incoming intensity to the interface boundary is corresponding to $\mu_j < 0$, obtained using the forward difference scheme with spatial step $\Delta x/2$ [42]:

$$2v_{\mathrm{g},1}(\omega_s, \mathrm{p})\mu_j \frac{\Psi_{s,\mathrm{p},N_2+2,j} - \Psi_{s,\mathrm{p},N_2+1,j}}{\Delta x} = \frac{\left(I_{s,\mathrm{p},N_2+2,j}^{\mathrm{pse}} - I_{s,\mathrm{p},N_2+2,j}^{\mathrm{ref}}\right) - \Psi_{s,\mathrm{p},N_2+2,j}}{\tau_1\left(\omega_s, \mathrm{p}, T^{\mathrm{ref}}\right)}. \tag{34}$$

Organizing Eq. (34), the equation calculating the incoming intensity to the interface boundary in Fig. 3 (d) is obtained as below:

$$\Psi_{s,\mathrm{p},N_2+1,j} = \frac{\frac{1}{\tau_1\left(\omega_s,\mathrm{p},T^{\mathrm{ref}}\right)}\left(I_{s,\mathrm{p},N_2+2,j}^{\mathrm{pse}} - I_{s,\mathrm{p},N_2+2,j}^{\mathrm{ref}}\right)}{-\left(\frac{1}{\tau_1\left(\omega_s,\mathrm{p},T^{\mathrm{ref}}\right)} + \frac{2v_{\mathrm{g},1}(\omega_s,\mathrm{p})\mu_j}{\Delta x}\right)\Psi_{s,\mathrm{p},N_2+2,j} - 2v_{\mathrm{g},1}(\omega_s,\mathrm{p})\mu_j\Delta x}. \tag{35}$$

In Fig. 3 (c), the intensity from the interface boundary to the nearest inner points is corresponding to $\mu_j < 0$, obtained using the forward difference scheme with spatial step $\Delta x/2$ [42]:

$$2v_{\mathrm{g},2}(\omega_s, \mathrm{p})\mu_j \frac{\Psi_{s,\mathrm{p},N_2+1,j} - \Psi_{s,\mathrm{p},N_2,j}}{\Delta x} = \frac{\left(I_{s,\mathrm{p},N_2,j}^{\mathrm{pse}} - I_{s,\mathrm{p},N_2,j}^{\mathrm{ref}}\right) - \Psi_{s,\mathrm{p},N_2,j}}{\tau_2\left(\omega_s, \mathrm{p}, T^{\mathrm{ref}}\right)}. \tag{36}$$

Organizing Eq. (36), the equation calculating the intensity from the interface to the nearest inner points is obtained as below:

$$\Psi_{s,\mathrm{p},N_2,j} = \frac{\frac{1}{\tau_2\left(\omega_s,\mathrm{p},T^{\mathrm{ref}}\right)}\left(I_{s,\mathrm{p},N_2,j}^{\mathrm{pse}} - I_{s,\mathrm{p},N_2,j}^{\mathrm{ref}}\right) - \frac{2v_{\mathrm{g},2}(\omega_s,\mathrm{p})\mu_j}{\Delta x}\Psi_{s,\mathrm{p},N_2+1,j}}{\left(-\frac{2v_{\mathrm{g},2}(\omega_s,\mathrm{p})\mu_j}{\Delta x} + \frac{1}{\tau_2\left(\omega_s,\mathrm{p},T^{\mathrm{ref}}\right)}\right)}. \tag{37}$$

In Fig. 3 (d), the intensity from the interface boundary to the nearest inner points is corresponding to $\mu_j \geq 0$, obtained using the forward difference scheme with spatial step $\Delta x/2$ [42]:

$$2v_{\mathrm{g},1}(\omega_s, \mathrm{p})\mu_j \frac{\Psi_{s,\mathrm{p},N_2+2,j} - \Psi_{s,\mathrm{p},N_2+1,j}}{\Delta x} = \frac{\left(I_{s,\mathrm{p},N_2+2,j}^{\mathrm{pse}} - I_{s,\mathrm{p},N_2+2,j}^{\mathrm{ref}}\right) - \Psi_{s,\mathrm{p},N_2+2,j}}{\tau_1\left(\omega_s, \mathrm{p}, T^{\mathrm{ref}}\right)}. \tag{38}$$

Organizing Eq. (38), the equation calculating the intensity from the interface to the nearest inner points is obtained as below:

$$\Psi_{s,\mathrm{p},N_2+2,j} = \frac{\frac{1}{\tau_1\left(\omega_s,\mathrm{p},T^{\mathrm{ref}}\right)}\left(I_{s,\mathrm{p},N_2+2,j}^{\mathrm{pse}} - I_{s,\mathrm{p},N_2+2,j}^{\mathrm{ref}}\right) + \frac{2v_{\mathrm{g},1}(\omega_s,\mathrm{p})\mu_j}{\Delta x}\Psi_{s,\mathrm{p},N_2+1,j}}{\left(\frac{2v_{\mathrm{g},1}(\omega_s,\mathrm{p})\mu_j}{\Delta x} + \frac{1}{\tau_1\left(\omega_s,\mathrm{p},T^{\mathrm{ref}}\right)}\right)}. \tag{39}$$

Thirdly, for the interface treatment, the detailed implementations to calculate the outgoing intensities from the interface are also presented based on the numerical framework in subsection 2.3. The calculations of the incoming intensities to the middle interface and the intensities from the middle interface to the nearest inner points are provided here. The incoming intensities to the middle interface contain two parts, that is, those from material 1 to the middle interface and those from material 2 to the middle interface, corresponding to $\mu_j \geq 0$ and $\mu_j < 0$, respectively. Two parts are obtained based on Eq. (8) using the backward and forward difference schemes with spatial step $\Delta x/2$, respectively [42]:

$$2v_{\mathrm{g},1}(\omega_s, \mathrm{p})\mu_j \frac{\Psi_{s,\mathrm{p},N_1+1,j} - \Psi_{s,\mathrm{p},N_1,j}}{\Delta x} = \frac{\left(I_{s,\mathrm{p},N_1,j}^{\mathrm{pse}} - I_{s,\mathrm{p},N_1,j}^{\mathrm{ref}}\right) - \Psi_{s,\mathrm{p},N_1,j}}{\tau_1\left(\omega_s, \mathrm{p}, T^{\mathrm{ref}}\right)}, \tag{40}$$

$$2v_{\mathrm{g},2}(\omega_s, \mathrm{p})\mu_j \frac{\Psi_{s,\mathrm{p},N_1+2,j} - \Psi_{s,\mathrm{p},N_1+1,j}}{\Delta x} = \frac{\left(I_{s,\mathrm{p},N_1+2,j}^{\mathrm{pse}} - I_{s,\mathrm{p},N_1+2,j}^{\mathrm{ref}}\right) - \Psi_{s,\mathrm{p},N_1+2,j}}{\tau_2\left(\omega_s, \mathrm{p}, T^{\mathrm{ref}}\right)}. \tag{41}$$

Organizing Eqs. (40) and (41), the equations calculating the incoming intensity to the middle interface for $\mu_j \geq 0$ and $\mu_j < 0$ are obtained as below:

$$\Psi_{s,\mathrm{p},N_1+1,j} = \frac{\frac{1}{\tau_1\left(\omega_s,\mathrm{p},T^{\mathrm{ref}}\right)}\left(I_{s,\mathrm{p},N_1,j}^{\mathrm{pse}} - I_{s,\mathrm{p},N_1,j}^{\mathrm{ref}}\right)}{+\left(\frac{2v_{\mathrm{g},1}(\omega_s,\mathrm{p})\mu_j}{\Delta x} - \frac{1}{\tau_1\left(\omega_s,\mathrm{p},T^{\mathrm{ref}}\right)}\right)\Psi_{s,\mathrm{p},N_1,j}\frac{2v_{\mathrm{g},1}(\omega_s,\mathrm{p})\mu_j}{\Delta x}}, \tag{42}$$

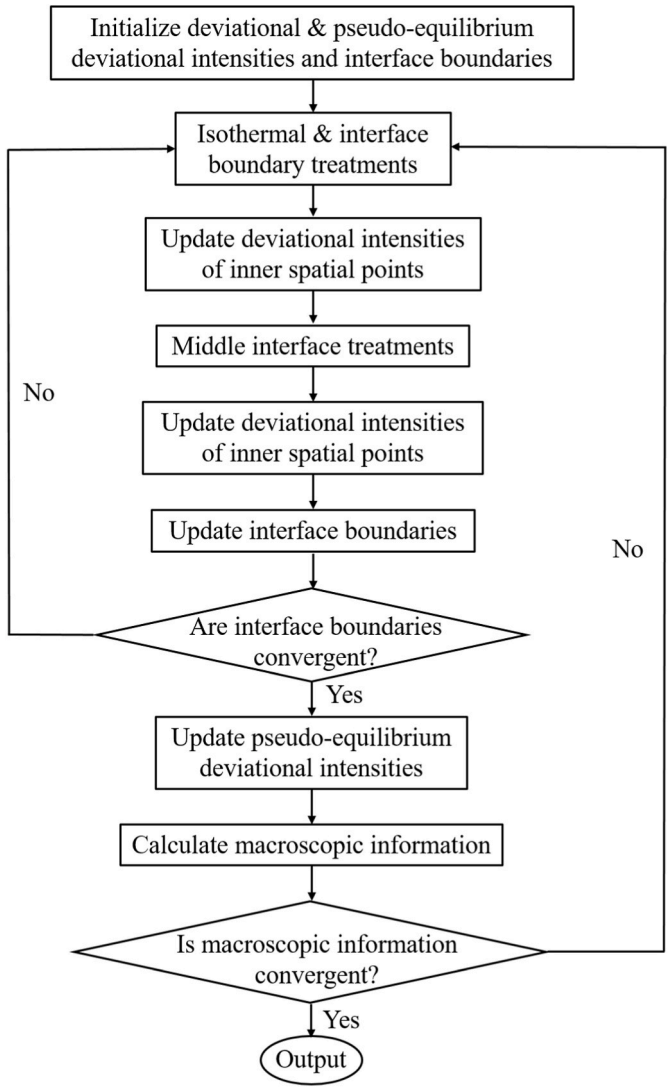

Fig. 4. The flow chart of the DOM scheme for interfacial phonon transport in multilayer films in the present work.

$$\Psi_{s,\mathrm{p},N_1+1,j}=\frac{\frac{1}{\tau_2\left(\omega_s,\mathrm{p},T^{\mathrm{ref}}\right)}\left(I^{\mathrm{pse}}_{s,\mathrm{p},N_1+2,j}-I^{\mathrm{ref}}_{s,\mathrm{p},N_1+2,j}\right)}{-\left(\frac{1}{\tau_2\left(\omega_s,\mathrm{p},T^{\mathrm{ref}}\right)}+\frac{2\nu_{\mathrm{g},2}(\omega_s,\mathrm{p})\mu_j}{\Delta x}\right)\Psi_{s,\mathrm{p},N_1+2,j}-2\nu_{\mathrm{g},2}(\omega_s,\mathrm{p})\mu_j\Delta x}. \tag{43}$$

The intensities from the interface to the nearest inner points contain two parts, that is, those from the middle interface to material 1 and those from the middle interface to material 2, corresponding to $\mu_j<0$ and $\mu_j\geq 0$, respectively. Two parts are obtained based on Eq. (8) using the forward and backward difference schemes with spatial step $\Delta x/2$, respectively [42]:

$$2\nu_{\mathrm{g},1}(\omega_s,\mathrm{p})\mu_j\frac{\Psi_{s,\mathrm{p},N_1+1,j}-\Psi_{s,\mathrm{p},N_1,j}}{\Delta x}=\frac{\left(I^{\mathrm{pse}}_{s,\mathrm{p},N_1,j}-I^{\mathrm{ref}}_{s,\mathrm{p},N_1,j}\right)-\Psi_{s,\mathrm{p},N_1,j}}{\tau_1\left(\omega_s,\mathrm{p},T^{\mathrm{ref}}\right)}, \tag{44}$$

$$2\nu_{\mathrm{g},2}(\omega_s,\mathrm{p})\mu_j\frac{\Psi_{s,\mathrm{p},N_1+2,j}-\Psi_{s,\mathrm{p},N_1+1,j}}{\Delta x}=\frac{\left(I^{\mathrm{pse}}_{s,\mathrm{p},N_1+2,j}-I^{\mathrm{ref}}_{s,\mathrm{p},N_1+2,j}\right)-\Psi_{s,\mathrm{p},N_1+2,j}}{\tau_2\left(\omega_s,\mathrm{p},T^{\mathrm{ref}}\right)}. \tag{45}$$

Organizing Eqs. (44) and (45), the equations calculating the intensities from the interface to the nearest inner points for $\mu_j<0$ and $\mu_j\geq 0$ are obtained as below:

$$\Psi_{s,\mathrm{p},N_1,j}=\frac{\frac{1}{\tau_1\left(\omega_s,\mathrm{p},T^{\mathrm{ref}}\right)}\left(I^{\mathrm{pse}}_{s,\mathrm{p},N_1,j}-I^{\mathrm{ref}}_{s,\mathrm{p},N_1,j}\right)-\frac{2\nu_{\mathrm{g},1}(\omega_s,\mathrm{p})\mu_j}{\Delta x}\Psi_{s,\mathrm{p},N_1+1,j}}{\left(-\frac{2\nu_{\mathrm{g},1}(\omega_s,\mathrm{p})\mu_j}{\Delta x}+\frac{1}{\tau_1\left(\omega_s,\mathrm{p},T^{\mathrm{ref}}\right)}\right)}, \tag{46}$$

$$\Psi_{s,\mathrm{p},N_1+2,j}=\frac{\frac{1}{\tau_2\left(\omega_s,\mathrm{p},T^{\mathrm{ref}}\right)}\left(I^{\mathrm{pse}}_{s,\mathrm{p},N_1+2,j}-I^{\mathrm{ref}}_{s,\mathrm{p},N_1+2,j}\right)+\frac{2\nu_{\mathrm{g},2}(\omega_s,\mathrm{p})\mu_j}{\Delta x}\Psi_{s,\mathrm{p},N_1+1,j}}{\left(\frac{2\nu_{\mathrm{g},2}(\omega_s,\mathrm{p})\mu_j}{\Delta x}+\frac{1}{\tau_2\left(\omega_s,\mathrm{p},T^{\mathrm{ref}}\right)}\right)}. \tag{47}$$

Finally, for the macroscopic variable calculation, the temperature, pseudo-equilibrium temperature and heat flux distributions are calculated after obtaining the deviational intensities using Eqs. (9)–(11). Considering the discrete angle and frequency, the integrals are evaluated using the summations as below

$$T_{m,i}=T^{\mathrm{ref}}+\frac{1}{2C_{V,m}}\sum_{\mathrm{p}}\sum_{s}\sum_{j}\frac{\Psi_{s,\mathrm{p},i,j}}{\nu_{\mathrm{g},m}(\omega_s,\mathrm{p})}\varsigma_j w_s, \tag{48}$$

$$T^{\mathrm{loc}}_{m,i}=T^{\mathrm{ref}}+\frac{1}{2C^{\mathrm{loc}}_{V,m}}\sum_{\mathrm{p}}\sum_{s}\sum_{j}\frac{\Psi_{s,\mathrm{p},i,j}}{\nu_{\mathrm{g},m}(\omega_s,\mathrm{p})\tau_m(\omega_s,\mathrm{p})}\varsigma_j w_s, \tag{49}$$

$$q_i=2\pi\sum_{\mathrm{p}}\sum_{s}\sum_{j}\Psi_{s,\mathrm{p},i,j}\mu_j\varsigma_j w_s, \tag{50}$$

where ς_j and w_s are the weights for the numerical evaluation of integrals of angle and frequency.

Totally, the present work proposes a DOM scheme to simulate cross-plane interfacial phonon transport in multilayer films with the flow chart in Fig. 4. Its detailed simulation steps are as follows: (1) Initialize the deviational and pseudo-equilibrium deviational intensities at all spatial point and the interface boundary conditions of two bilayer films. (2) For the bilayer film in Fig. 3 (a), emit the deviational intensities from the left isothermal and right interface boundaries; for the bilayer film in Fig. 3 (b), emit the deviational intensities from the right isothermal and left interface boundaries. (3) For the bilayer film in Fig. 3 (a), update the deviational intensities point by point in space from the left isothermal boundary to the middle interface, and from the right interface boundary to the middle interface; for the bilayer film in Fig. 3 (b), update the deviational intensities point by point in space from the right isothermal boundary to the middle interface, and from the left interface boundary to the middle interface. (4) For two bilayer films in Fig. 3(a) and (b), when the spatial points reach the middle interfaces, implement the interface treatments at the middle interfaces. (5) After the interface treatments, for the bilayer film in Fig. 3 (a), update the deviational intensities from the middle interface to the left isothermal boundary and the right interface boundary; for the bilayer film in Fig. 3 (b), update the deviational intensities from the middle interface to the right isothermal boundary and the left interface boundary. (6) For two bilayer films in Fig. 3(a) and (b), when the spatial points reach the right and left interface boundaries, implement the interface treatments at the right and left interface boundaries, and then update the interface boundary conditions of two bilayer films. (7) Verify whether the interface boundary conditions converge. If they converge, update the pseudo-equilibrium deviational intensities, and calculate the macroscopic information, i.e. temperature, pseudo-equilibrium temperature and heat flux distributions. Otherwise, carry out the next iterative calculation for the interface boundary conditions based on the updated interface boundary conditions until they converge. (8) After obtaining the macroscopic information, verify whether the temperature and heat flux

distributions converge. If they converge, output the calculation results. Otherwise, based on the updated temperature and pseudo-equilibrium temperature as well as the updated interface boundary conditions, carry out the next iterative calculation for the temperature, pseudo-equilibrium temperature and heat flux distributions until they converge.

It should be pointed out that due to two bilayer films are formed by separating the multilayer film at the middle interface, the right interface boundary in Fig. 3 (a) and the left interface boundary in Fig. 3 (b) are the same interface. Therefore, the interface treatments at the right and left interface boundaries should be combined together in step (5). In detail, among the phonons entering the bilayer film from the right interface boundary in Fig. 3 (a), two parts should be considered, that is, the reflected phonons at the right interface boundary in Fig. 3 (a) and the transmitted phonons from the right to the left of the left interface boundary in Fig. 3 (b). Among the phonons entering the bilayer film from the left interface boundary in Fig. 3 (b), two parts should be considered, that is, the transmitted phonons from the left to the right of the right interface boundary in Fig. 3 (a) and the reflected phonons at the left interface boundary in Fig. 3 (b). The numerical scheme in the present work can be extended into other multilayer films with more or fewer layers, and is adopted to investigate the roughness dependence of cross-plane interfacial phonon transport in multilayer films after being verified in subsection 3.2.

2.3. Interface treatment

The present work develops the DOM scheme of interface treatment with spectral specularity and spectral transmissivity based on SMMM. Using this interface treatment, the outgoing deviational intensities from the interface can be obtained, mentioned in subsection 2.2.

SMMM provides the transmissivities accounting for partially specular and partially diffuse scatterings at the interfaces as below [16].

$$\alpha_{12}(\theta_1,\omega,\mathrm{p}) = P_1(\omega,\mathrm{p})\alpha_{\mathrm{Specular},12}(\theta_1,\omega,\mathrm{p}) + (1-P_1(\omega,\mathrm{p}))\alpha_{\mathrm{Diffuse},12}(\omega,\mathrm{p}), \tag{51}$$

$$\alpha_{21}(\theta_2,\omega,\mathrm{p}) = P_2(\omega,\mathrm{p})\alpha_{\mathrm{Specular},21}(\theta_2,\omega,\mathrm{p}) + (1-P_2(\omega,\mathrm{p}))\alpha_{\mathrm{Diffuse},21}(\omega,\mathrm{p}), \tag{52}$$

where θ_1 and θ_2 are the incident angles at the interface from material 1 to 2 and from material 2 to 1, respectively; P is the spectral specularity; $\alpha_{\mathrm{Specular},12}$ and $\alpha_{\mathrm{Diffuse},12}$ are the transmissivities from material 1 to 2 for spectral specular and spectral diffuse scatterings, respectively; $\alpha_{\mathrm{Specular},21}$ and $\alpha_{\mathrm{Diffuse},21}$ are the transmissivities from material 2 to 1 for spectral specular and spectral diffuse scatterings, respectively. Based on the assumption of elastic scattering and neglecting the polarization conversion, the transmissivities in SMMM can be deduced according to the principle of detailed balance [16]

$$\begin{aligned}\alpha_{12}(\theta_1,\omega,\mathrm{p}) = {} & \exp\left(-\frac{16\pi^2\eta^2}{\lambda_1^2(\omega,\mathrm{p})}\right)\cdot\min\left\{1,\frac{P_2(\omega,\mathrm{p})C_{\omega,\mathrm{p},2}v_{\mathrm{g},2}^3(\omega,\mathrm{p})}{P_1(\omega,\mathrm{p})C_{\omega,\mathrm{p},1}v_{\mathrm{g},1}^3(\omega,\mathrm{p})}\right\}\frac{\frac{4\rho_2 v_{\mathrm{g},2}(\omega,\mathrm{p})}{\rho_1 v_{\mathrm{g},1}(\omega,\mathrm{p})}\frac{\cos\theta_2}{\cos\theta_1}}{\left(\frac{\rho_2 v_{\mathrm{g},2}(\omega,\mathrm{p})}{\rho_1 v_{\mathrm{g},1}(\omega,\mathrm{p})}+\frac{\cos\theta_2}{\cos\theta_1}\right)^2}\\ & +\left(1-\exp\left(-\frac{16\pi^2\eta^2}{\lambda_1^2(\omega,\mathrm{p})}\right)\right)\cdot\frac{(1-P_2(\omega,\mathrm{p}))k_2^2(\omega,\mathrm{p})}{(1-P_1(\omega,\mathrm{p}))k_1^2(\omega,\mathrm{p})+(1-P_2(\omega,\mathrm{p}))k_2^2(\omega,\mathrm{p})},\end{aligned} \tag{53}$$

$$\begin{aligned}\alpha_{21}(\theta_2,\omega,\mathrm{p}) = {} & \exp\left(-\frac{16\pi^2\eta^2}{\lambda_2^2(\omega,\mathrm{p})}\right)\cdot\min\left\{1,\frac{P_1(\omega,\mathrm{p})C_{\omega,\mathrm{p},1}v_{\mathrm{g},1}^3(\omega,\mathrm{p})}{P_2(\omega,\mathrm{p})C_{\omega,\mathrm{p},2}v_{\mathrm{g},2}^3(\omega,\mathrm{p})}\right\}\frac{\frac{4\rho_2 v_{\mathrm{g},2}(\omega,\mathrm{p})}{\rho_1 v_{\mathrm{g},1}(\omega,\mathrm{p})}\frac{\cos\theta_2}{\cos\theta_1}}{\left(\frac{\rho_2 v_{\mathrm{g},1}(\omega,\mathrm{p})}{\rho_1 v_{\mathrm{g},1}(\omega,\mathrm{p})}+\frac{\cos\theta_2}{\cos\theta_1}\right)^2}\\ & +\left(1-\exp\left(-\frac{16\pi^2\eta^2}{\lambda_2^2(\omega,\mathrm{p})}\right)\right)\cdot\frac{(1-P_1(\omega,\mathrm{p}))k_1^2(\omega,\mathrm{p})}{(1-P_1(\omega,\mathrm{p}))k_1^2(\omega,\mathrm{p})+(1-P_2(\omega,\mathrm{p}))k_2^2(\omega,\mathrm{p})},\end{aligned} \tag{54}$$

where λ is phonon wavelength, obtained from $\lambda(\omega,\mathrm{p}) = \frac{2\pi}{k(\omega,\mathrm{p})}$ with the wave number k; η is interface roughness. SMMM can both capture the spectrum dependence of specularity and specular and diffuse scatterings and satisfy the principle of detailed balance. Although it cannot consider the inelastic scattering and polarization conversion, even inaccurate for the phonons with high frequency, it is currently most appropriate theoretical model accounting for the spectral specularity and spectral transmissivity [16]. SMMM will be adopted in the present work and its transmissivities are calculated just with the phonon dispersions and interface roughness. The interface scattering in the present work is referred to Fig. 5, where $(\Psi_{1,\omega,\mathrm{p}})^+$ and $(\Psi_{2,\omega,\mathrm{p}})^-$ are the incoming deviational intensities from materials 1 and 2, respectively, and $(\Psi_{1,\omega,\mathrm{p}})^-$ and $(\Psi_{2,\omega,\mathrm{p}})^+$ are the outgoing deviational intensities to materials 1 and 2. According to the energy conservation law for interface scattering, the equations below are valid:

$$\begin{aligned}\int_{\frac{\pi}{2}}^{\pi}(\Psi_{1,\omega,\mathrm{p}})^-\sin\theta\cos\theta d\theta = {} & \int_{\frac{\pi}{2}}^{\pi}\alpha_{21}(\theta,\omega,\mathrm{p})(\Psi_{2,\omega,\mathrm{p}})^-\sin\theta\cos\theta d\theta\\ & -\int_0^{\frac{\pi}{2}}(1-\alpha_{12}(\theta,\omega,\mathrm{p}))(\Psi_{1,\omega,\mathrm{p}})^+\sin\theta\cos\theta d\theta,\end{aligned} \tag{55}$$

$$\begin{aligned}\int_0^{\frac{\pi}{2}}(\Psi_{2,\omega,\mathrm{p}})^+\sin\theta\cos\theta d\theta = {} & -\int_{\frac{\pi}{2}}^{\pi}(1-\alpha_{21}(\theta,\omega,\mathrm{p}))(\Psi_{2,\omega,\mathrm{p}})^-\sin\theta\cos\theta d\theta\\ & +\int_0^{\frac{\pi}{2}}\alpha_{12}(\theta,\omega,\mathrm{p})(\Psi_{1,\omega,\mathrm{p}})^+\sin\theta\cos\theta d\theta.\end{aligned} \tag{56}$$

For the outgoing deviational intensities of diffuse scattering in Eqs. (55) and (56), the equations below are valid:

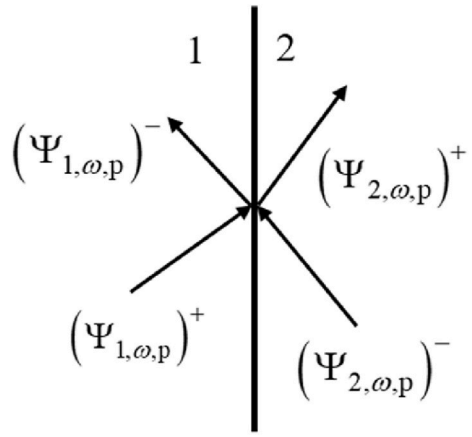

Fig. 5. The schematic diagram for the interface scattering. The vertical black solid line is the interface, and the black solid arrows towards and away from the interface denote the ingoing and outgoing deviational intensities, respectively.

$$\begin{aligned}&\int_{\frac{\pi}{2}}^{\pi}(\Psi_{1,\omega,\mathrm{p}})^-_{\mathrm{Diffuse}}\sin\theta\cos\theta d\theta\\&=(1-P_2(\omega,\mathrm{p}))\alpha_{\mathrm{Diffuse},21}(\omega,\mathrm{p})\int_{\frac{\pi}{2}}^{\pi}(\Psi_{2,\omega,\mathrm{p}})^-\sin\theta\cos\theta d\theta\\&-(1-P_1(\omega,\mathrm{p}))(1-\alpha_{\mathrm{Diffuse},12}(\omega,\mathrm{p}))\int_0^{\frac{\pi}{2}}(\Psi_{1,\omega,\mathrm{p}})^+\sin\theta\cos\theta d\theta,\end{aligned}\tag{57}$$

$$\begin{aligned}&\int_0^{\frac{\pi}{2}}(\Psi_{2,\omega,\mathrm{p}})^+_{\mathrm{Diffuse}}\sin\theta\cos\theta d\theta\\&=-(1-P_2(\omega,\mathrm{p}))(1-\alpha_{\mathrm{Diffuse},21}(\omega,\mathrm{p}))\int_{\frac{\pi}{2}}^{\pi}(\Psi_{2,\omega,\mathrm{p}})^-\sin\theta\cos\theta d\theta+.\\&(1-P_1(\omega,\mathrm{p}))\alpha_{\mathrm{Diffuse},12}(\omega,\mathrm{p})\int_0^{\frac{\pi}{2}}(\Psi_{1,\omega,\mathrm{p}})^+\sin\theta\cos\theta d\theta\end{aligned}\tag{58}$$

Based on the assumption of diffuse scattering, the outgoing deviational intensities are isotropic for diffuse scattering and thus $(\Psi_{\omega,\mathrm{p},1})^-_{\mathrm{Diffuse}}$ and $(\Psi_{\omega,\mathrm{p},2})^+_{\mathrm{Diffuse}}$ are uniform in all directions. Due to the direction is discretized into a series of discrete angles, Eqs. (57) and (58) are further simplified as

$$\begin{aligned}(\Psi_{1,s,\mathrm{p}})^-_{\mathrm{Diffuse}}&=-2\sum_{j=N_\mu/2+1}^{N_\mu}(1-P_{2,s,\mathrm{p}})\alpha_{\mathrm{Diffuse},21,s,\mathrm{p}}(\Psi_{2,s,\mathrm{p}j})^-\mu_j\varsigma_j\\&+2\sum_{j=1}^{N_\mu/2}(1-P_{1,s,\mathrm{p}})(1-\alpha_{\mathrm{Diffuse},12,s,\mathrm{p}})(\Psi_{1,s,\mathrm{p}j})^+\mu_j\varsigma_j,\end{aligned}\tag{59}$$

$$\begin{aligned}(\Psi_{2,s,\mathrm{p}})^+_{\mathrm{Diffuse}}&=-2\sum_{j=N_\mu/2+1}^{N_\mu}(1-P_{2,s,\mathrm{p}})(1-\alpha_{\mathrm{Diffuse},21,s,\mathrm{p}})(\Psi_{2,s,\mathrm{p}j})^-\mu_j\varsigma_j\\&+2\sum_{j=1}^{N_\mu/2}(1-P_{1,s,\mathrm{p}})\alpha_{\mathrm{Diffuse},12,s,\mathrm{p}}(\Psi_{1,s,\mathrm{p}j})^+\mu_j\varsigma_j,\end{aligned}\tag{60}$$

where $j=1$ to $j=N_\mu/2$ are corresponding to the angles from 0 to $\pi/2$; $j=N_\mu/2$ to $j=N_\mu$ are corresponding to the angles from $\pi/2$ to π.

For the outgoing deviational intensities of specular scattering in Eqs. (55) and (56), the specular interface scattering obeys Snell's law and it is required that a phonon specularly incident on the interface with an incident angle transmits across the interface with the corresponding transmitted angle, which means that the incident and transmitted angles correspond one-to-one. Thus the specular scattering parts in Eqs. (55) and (56) have the following relationships:

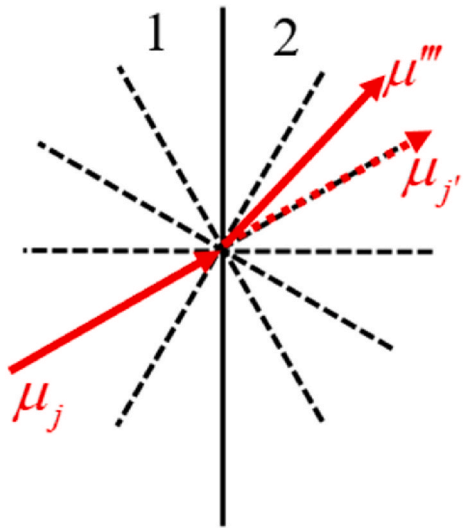

Fig. 6. The schematic diagram for the specular scattering at the interface. The vertical black solid line is the interface, and the black dashed lines correspond to the discrete angles. The red solid arrows towards and away from the interface denote the incident and transmitted phonons, and the red dashed arrow away from the interface denote the discrete angle corresponding to the transmitted angle, illustrated in the main text. (For interpretation of the references to colour in this figure legend, the reader is referred to the web version of this article.)

$$\begin{aligned}(\Psi_{1,\omega,\mathrm{p}}(\mu'))^-_{\mathrm{Specular}}&=P_2(\omega,\mathrm{p})\alpha_{\mathrm{Specular},21}(\mu,\omega,\mathrm{p})(\Psi_{2,\omega,\mathrm{p}}(\mu))^-_{\mathrm{Specular}}\\&+P_1(\omega,\mathrm{p})(1-\alpha_{\mathrm{Specular},12}(-\mu',\omega,\mathrm{p}))(\Psi_{1,\omega,\mathrm{p}}(-\mu'))^+_{\mathrm{Specular}},\end{aligned}\tag{61}$$

$$\begin{aligned}(\Psi_{2,\omega,\mathrm{p}}(\mu''))^+_{\mathrm{Specular}}&=P_2(\omega,\mathrm{p})(1-\alpha_{\mathrm{Specular},21}(-\mu'',\omega,\mathrm{p}))(\Psi_{2,\omega,\mathrm{p}}(-\mu''))^-_{\mathrm{Specular}}\\&+P_1(\omega,\mathrm{p})\alpha_{\mathrm{Specular},12}(\mu,\omega,\mathrm{p})(\Psi_{1,\omega,\mathrm{p}}(\mu))^+_{\mathrm{Specular}}.\end{aligned}\tag{62}$$

where $-\mu'$ and $-\mu''$ are the incident angles on the interface from the material 1 and 2, respectively, and μ are their corresponding transmitted angles. Reorganize Eqs. (61) and (62) using discrete angles and the following equations are obtained:

$$\begin{aligned}(\Psi_{1,s,\mathrm{p}}(\mu^{`}))^-_{\mathrm{Specular}}&=P_{2,s,\mathrm{p}}\alpha_{\mathrm{Specular},21,s,\mathrm{p}}\left(\mu_j\right)\left(\Psi_{2,s,\mathrm{p}}\left(\mu_j\right)\right)^-_{\mathrm{Specular}}\\&+P_{1,s,\mathrm{p}}\left(1-\alpha_{\mathrm{Specular},12,s,\mathrm{p}}(-\mu^{`})\right)(\Psi_{1,s,\mathrm{p}}(-\mu^{`}))^+_{\mathrm{Specular}},\end{aligned}\tag{63}$$

$$\begin{aligned}(\Psi_{2,s,\mathrm{p}}(\mu^{``}))^-_{\mathrm{Specular}}&=P_{2,s,\mathrm{p}}\left(1-\alpha_{\mathrm{Specular},21,s,\mathrm{p}}(-\mu^{``})\right)(\Psi_{2,s,\mathrm{p}}(-\mu^{``}))^-_{\mathrm{Specular}}\\&+P_{1,s,\mathrm{p}}\alpha_{\mathrm{Specular},12,s,\mathrm{p}}\left(\mu_j\right)\left(\Psi_{1,s,\mathrm{p}}\left(\mu_j\right)\right)^+_{\mathrm{Specular}}.\end{aligned}\tag{64}$$

When phonons are specularly scattered by the interface, they are assumed as the plane waves, and this scattering obeys Snell's law. The incident and transmitted angles in Snell's law have the following relationships [8,9]:

$$\frac{v_{\mathrm{g},1}(\omega,\mathrm{p})}{\sqrt{1-(\mu'(\omega,\mathrm{p}))^2}}=\frac{v_{\mathrm{g},2}(\omega,\mathrm{p})}{\sqrt{1-\left(\mu_j\right)^2}},\tag{65}$$

$$\frac{v_{\mathrm{g},1}(\omega,\mathrm{p})}{\sqrt{1-\left(\mu_j\right)^2}}=\frac{v_{\mathrm{g},2}(\omega,\mathrm{p})}{\sqrt{1-(\mu''(\omega,\mathrm{p}))^2}}.\tag{66}$$

To take the present DOM scheme to simulate interfacial phonon transport, the challenge that the actual incident or transmitted angles may not align with the discrete angles should be first addressed. This is caused by the fact that the discrete angles on both sides of the interface

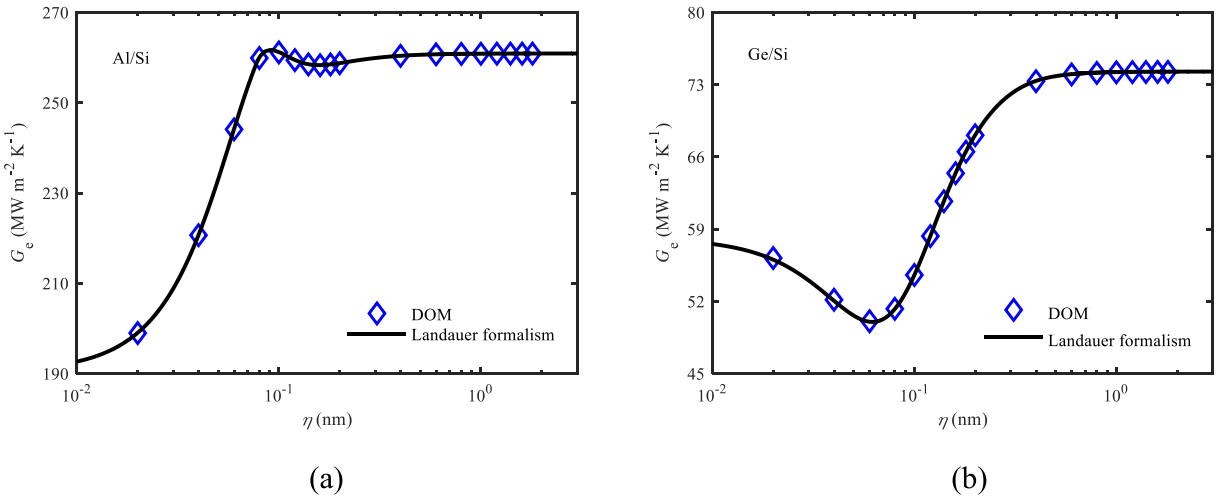

Fig. 7. The thermal boundary conductances based on the emitted phonon temperature at various interface roughnesses: (a) Al/Si and (b) Ge/Si.

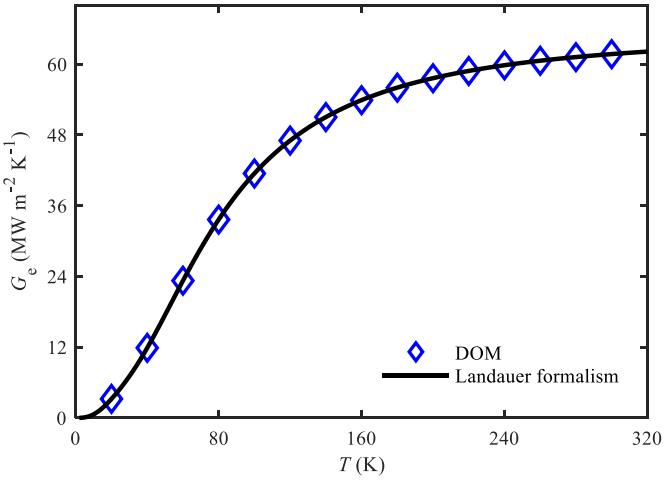

Fig. 8. The thermal boundary conductances of Ge/Si based on the emitted phonon temperature at various temperatures.

may not satisfy the corresponding relationship in Snell's law. For instance, shown in Fig. 6, a phonon is incident on the interface with the incident angle μ_j, and based on Snell's law, its corresponding transmitted angle is assumed to equal μ''', not belonging to the discrete angles in the simulation. To address this challenge, define a cumulative distribution for angles as

$$\Theta(\mu_0) = \int_0^{\mu_0} \mathrm{d}\mu, \tag{67}$$

where μ_0 is the cut off angle for the integral. Rewrite Eq. (67) with discrete angles as

$$\Theta\left(\mu_{j_0}\right) = \sum_{j=1}^{N_{\mu_{j_0}}} \varsigma_j, \tag{68}$$

where μ_{j_0} is one of the discrete angles in the simulation with index number j_0; $N_{\mu_{j_0}}$ is the order value of μ_{j_0} when all discrete angles are arranged in order from small to large. Based on the above definitions, the implementations for the specular interface scattering in DOM are given as follows: (1) When a phonon is incident on the interface with the incident angle μ_j, calculate the transmitted based on Snell's law, i.e. Eq. (65) or (66), and the result is assumed to equal μ'''. (2) Comparing the transmitted angle μ''' and the cumulative distribution Eq. (68), if $\Theta\left(\mu_{j'}\right) \le \mu''' < \Theta\left(\mu_{j'+1}\right)$, the transmitted angle μ''' is corresponding to $\mu_{j'}$, one of the discrete angles. In these situations, all calculations regarding μ''' are the same as $\mu_{j'}$. For instance, in all summations in previous parts about μ''', the value and weight of μ''' should be replaced with those of $\mu_{j'}$, etc. It should be noted that since the phonon properties depend on the phonon frequency, the relationships in Snell's law also depend on phonon frequency, and Eqs. (65) and (66) are different for different phonon frequencies.

With the outgoing deviational intensities of diffuse and specular scatterings in Eqs. (55) and (56), the outgoing deviational intensities are calculated by

$$\left(\Psi_{1,\omega,\mathrm{p}}\left(\mu_j\right)\right)^- = \left(\Psi_{1,\omega,\mathrm{p}}\right)^-_{\mathrm{Diffuse}} + \left(\Psi_{1,\omega,\mathrm{p}}\left(\mu_j\right)\right)^-_{\mathrm{Specular}}, \tag{69}$$

$$\left(\Psi_{2,\omega,\mathrm{p}}\left(\mu_j\right)\right)^+ = \left(\Psi_{2,\omega,\mathrm{p}}\right)^+_{\mathrm{Diffuse}} + \left(\Psi_{2,\omega,\mathrm{p}}\left(\mu_j\right)\right)^+_{\mathrm{Specular}}. \tag{70}$$

The above deductions give the DOM scheme of interface treatment with spectral specularity and spectral transmissivity. This treatment is validated in bilayer films through comparisons with Landauer formalism and experiments.

3. Validations

In this section, the interface treatment with spectral specularity and spectral transmissivity and the numerical framework for multilayer films in the previous section are validated against Landauer formalism, experiments and MC.

3.1. Bilayer films

In subsection 3.1, the interface treatment with the spectral specularity and spectral transmissivity of DOM is validated in bilayer films by comparing its thermal boundary conductance with Landauer formalism and experiments. Two definitions for thermal boundary conductance are adopted in the present work, that is, those based on the emitted phonon and equivalent equilibrium temperatures. Two temperatures have different physical meanings with detailed explanations provided here. The emitted phonon temperature denotes the ideal temperature defined by the conjectured phonons with infinite mean free paths emitted from the isothermal boundary at this temperature and ballistically transporting and scattered at the interface. For the latter one, owing to the non-equilibrium effect at the interface, the definition for the temperature with the conventional way under the thermal equilibrium state is

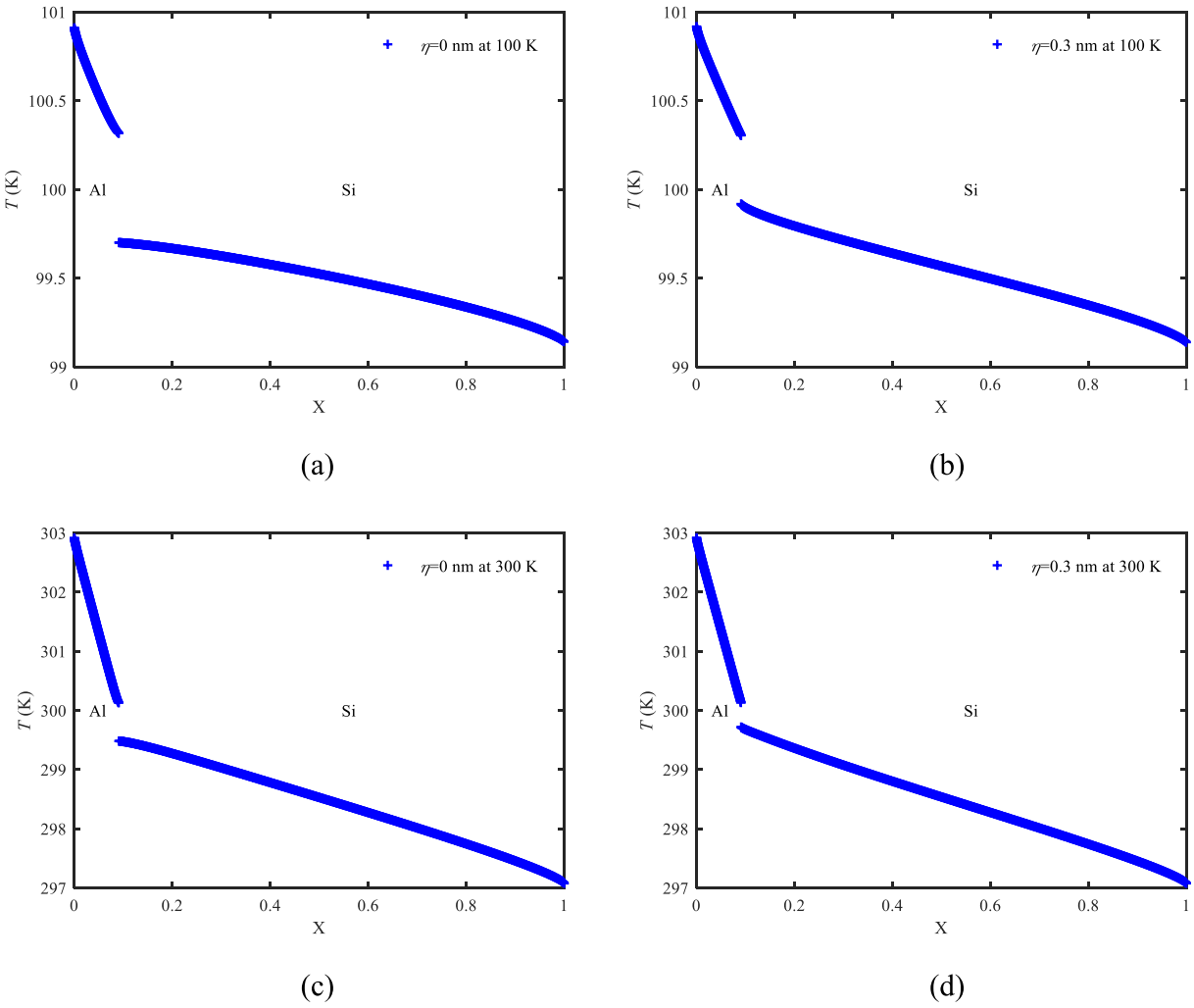

Fig. 9. The temperature distributions of cross-plane interfacial phonon transport across bilayer films by DOM with the different interface roughnesses and referenced temperatures: (a) the bilayer film with the interface roughness being 0 nm and the referenced temperature being 100 K, (b) the bilayer film with the interface roughness being 0.3 nm and the referenced temperature being 100 K, (c) the bilayer film with the interface roughness being 0 nm and the referenced temperature being 300 K, and (d) the bilayer film with the interface roughness being 0.3 nm and the referenced temperature being 300 K.

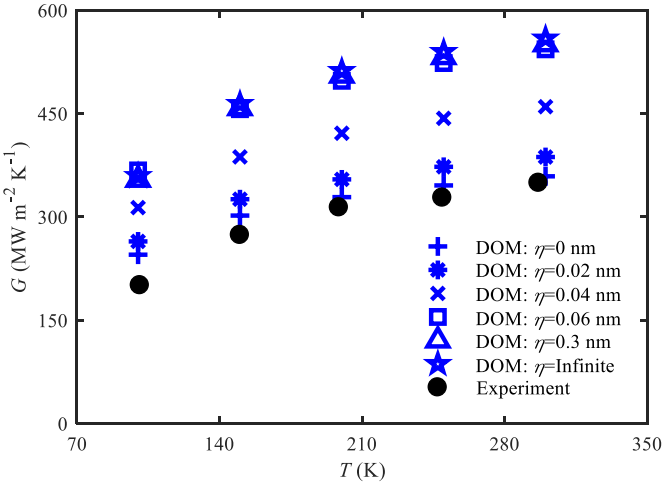

Fig. 10. The thermal boundary conductances of Al/Si based on the equivalent equilibrium temperature at various temperatures.

invalid. Thus the equivalent equilibrium temperature is introduced to quantify the temperature near the interface, reproducing the average energy of all phonons near the interface. In detail, the average energy calculated based on the equivalent equilibrium temperature equals the realistic energy near the interface. The thermal boundary conductances in Landauer formalism and experiments correspond to the emitted phonon and equivalent equilibrium temperatures, respectively.

In bilayer films, the thermal boundary conductances based on the emitted phonon temperature at various interface roughnesses are first calculated by DOM and compared with Landauer formalism below:

$$\begin{aligned} G_{\mathrm{e}} &= 2\pi \sum_{\mathrm{p}} \int_0^{\omega_{\max,\mathrm{p},1}} \int_0^{\frac{\pi}{2}} C_{\omega,1} v_{\mathrm{g},1}(\omega,\mathrm{p}) \alpha_{12}(\omega,\mathrm{p},\theta) \sin\theta \cos\theta \mathrm{d}\theta \mathrm{d}\omega \\ &= \pi \sum_{\mathrm{p}} \sum_{s=1}^{N_{\omega,\mathrm{p}}} \sum_{j=1}^{N_{\mu}} C_{\omega_s,1} v_{\mathrm{g},1}(\omega_s,\mathrm{p}) \alpha_{12}\left(\omega_s,\mathrm{p},\mu_j\right) \mu_j \varsigma_j w_s. \end{aligned} \tag{71}$$

The physical model of bilayer films is shown in Fig. 1 (a), and the intensity calculation of inner spatial points, the boundary treatment and the macroscopic variable calculation are referred to Refs. [27,41], and the interface treatment is implemented following subsection 2.3. Two material pairs are considered, i.e. Al (1)/Si(2) and Ge (1)/Si(2), with the dispersions of Al, Si and Ge in Refs. [43–45] and the relaxation times of Si and Ge in Ref. [46]. For Al, only contribution from phonons is considered and the calculations of their relaxation times are referred to

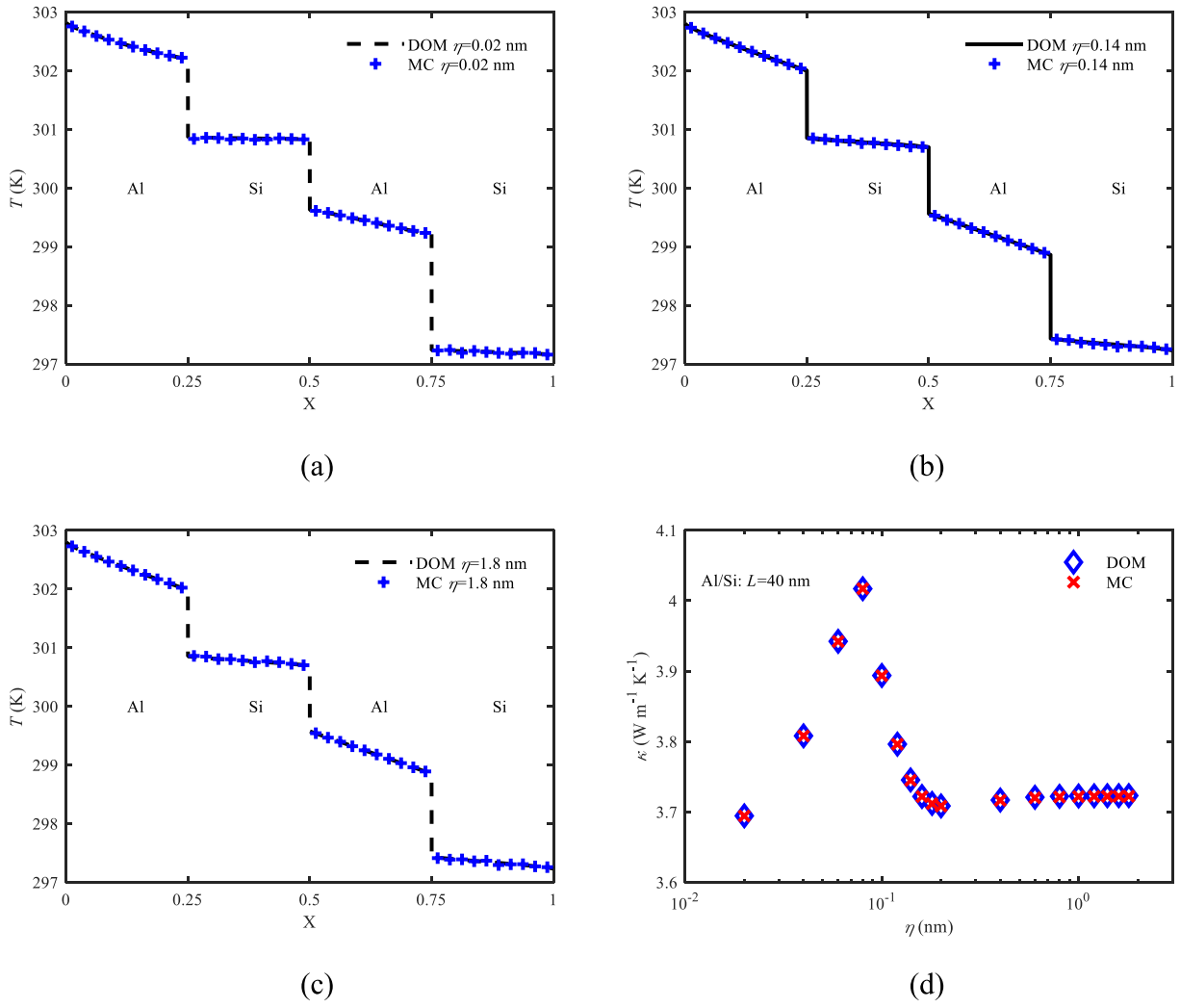

Fig. 11. The steady-state cross-plane temperature distributions and cross-plane thermal conductivities of Al/Si multilayer films with the total thickness of 40 nm at various interface roughnesses: (a) the interface roughnesses being 0.02 nm, (b) the interface roughnesses being 0.14 nm, (c) the interface roughnesses being 1.8 nm and (d) the cross-plane thermal conductivities at various interface roughnesses.

Refs. [47,48], assumed to be an constant throughout all frequencies and polarizations at each temperature. The relaxation times of Al at corresponding temperatures are obtained based on their lattice thermal conductivities at various temperatures. The lattice thermal conductivities of Al in the present work are referred to Ref. [49] and the relationship between the lattice thermal conductivity and relaxation time is given by [50].

$$\kappa = \frac{1}{3}\sum_{\mathrm{p}} \int C_{\omega,\mathrm{p}} v_{\mathrm{g}}^2(\omega,\mathrm{p})\tau d\omega. \tag{72}$$

The left and right sides of bilayer films are considered as the isothermal boundaries with temperatures 303 and 297 K. The interface roughness first increases from 0.02 to 0.2 nm with the common difference 0.02 nm and then increases from 0.2 to 1.8 nm with the common difference 0.02 nm. The total thicknesses of all bilayer films are fixed at 40 nm with the volume ratios 1, and the spatial steps are fixed at 0.01 nm for all simulations. When the relative errors between two adjacent iteration steps of both temperatures and heat fluxes are smaller than 1×10^{-7}, output the calculation results. The spectral transmissivities are calculated based on SMMM [16] and referred to Ref. [41]. The emitted phonon temperatures are obtained and then the corresponding thermal boundary conductances are calculated with

$$G_{\mathrm{e}}' = \frac{q}{T_1^{\mathrm{e}} - T_2^{\mathrm{e}}}. \tag{73}$$

Fig. 7 gives the thermal boundary conductances based on emitted phonon temperature at various interface roughnesses obtained by both DOM and Landauer formalism. The results by both methods agree well with each other, demonstrating that the present interface treatment can simulate phonon scattering process at the interface. From the results, for Al/Si, thermal boundary conductance first increases dramatically with increasing interface roughness, and reaches the maximum at interface roughness 0.08 nm, and then decreases slightly until the interface roughness reaches 0.16 nm, and next increases slightly, and eventually tends to a constant. For Ge/Si, the relationship between the thermal boundary conductance and interface roughness is different from that for Al/Si. With increasing interface roughness, the thermal boundary conductance first decreases dramatically, and reaches the minimum at interface roughness 0.06 nm, and then increases dramatically until the interface roughness reaches 0.4 nm, and next continues to increase slightly, and eventually tends to a constant.

Then the thermal boundary conductances based on the emitted phonon temperature at various temperatures are calculated by DOM and also compared with Landauer formalism. Owing to the lack of lattice thermal conductivities at various temperatures for Al, this comparison

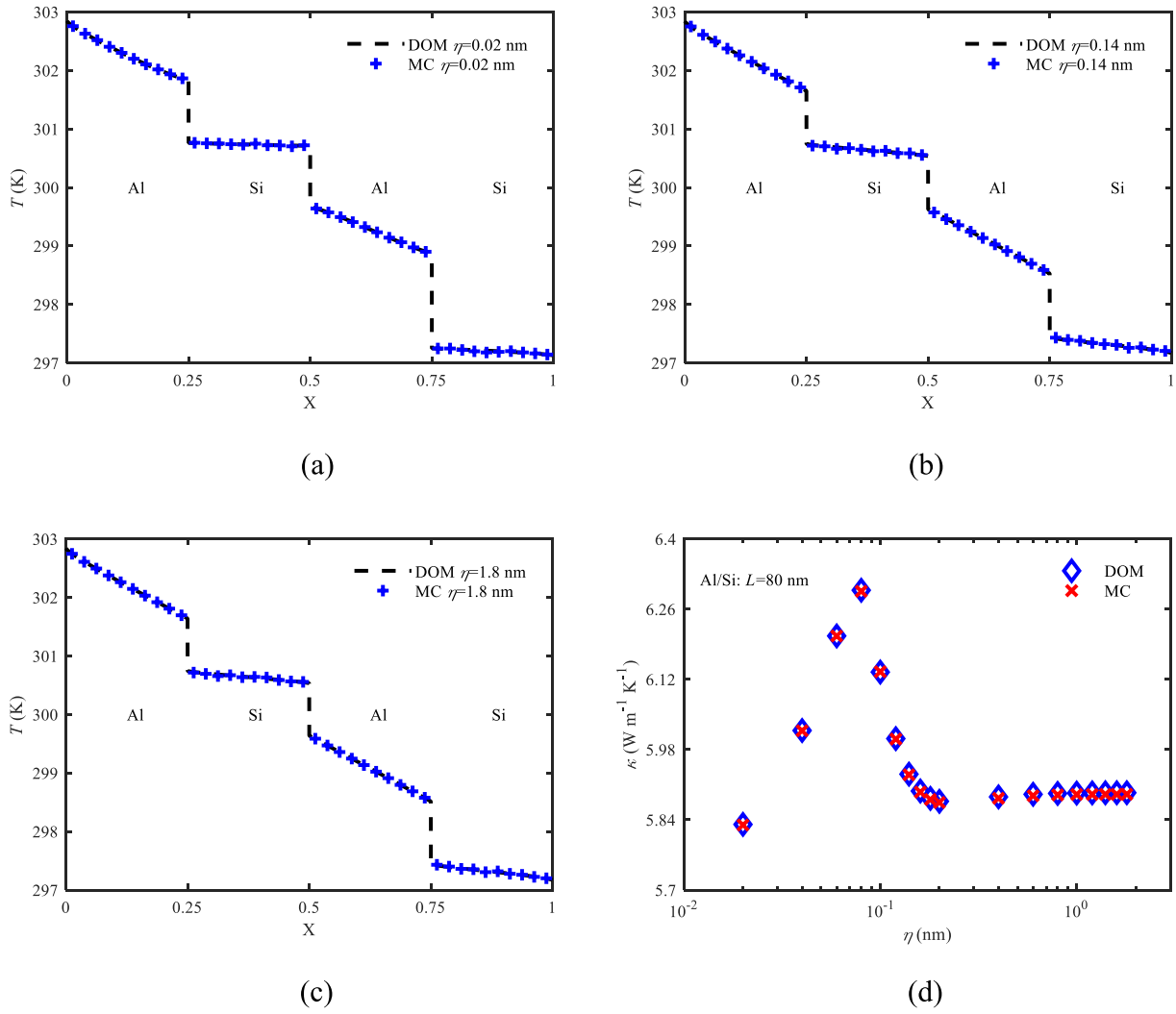

Fig. 12. The steady-state cross-plane temperature distributions and cross-plane thermal conductivities of Al/Si multilayer films with the total thickness of 80 nm at various interface roughnesses: (a) the interface roughnesses being 0.02 nm, (b) the interface roughnesses being 0.14 nm, (c) the interface roughnesses being 1.8 nm and (d) the cross-plane thermal conductivities at various interface roughnesses.

only considers the material pair Ge (1)/Si(2). The dispersions and relaxation times of Si and Ge are referred to Refs. [43,44] and Ref. [46], respectively. The left and right sides of bilayer films are set as the isothermal boundaries with small temperature differences to match the small temperature difference assumption. For instance, to calculate the thermal boundary conductance at 20 K, fix the left and right isothermal boundaries at 20.1 and 19.9 K, respectively; to calculate the thermal boundary conductance at 40 K, fix the left and right isothermal boundaries at 40.2 and 39.8 K, respectively; to calculate the thermal boundary conductance at 200 K, fix the left and right isothermal boundaries at 201 and 199 K, respectively; to calculate the thermal boundary conductance at 300 K, fix the left and right isothermal boundaries at 303 and 297 K, respectively; etc. The total thicknesses of all bilayer films are fixed at 40 nm with the volume ratios 1, and the spatial steps and interface roughnesses in all simulations are fixed at 0.01 and 0.14 nm, respectively. When the relative errors between two adjacent iteration steps for both temperature and heat flux are smaller than 1×10^{-7}, the calculation results are output. SMMM is also adopted to calculate the spectral transmissivities and the thermal boundary conductance based on the emitted phonon temperature is calculated by DOM, referred to Ref. [41] and with Landauer formalism using Eq. (71). Fig. 8 presents the thermal boundary conductances based on emitted phonon temperature at various temperatures calculated by both DOM and Landauer formalism, showing good agreements. The results show that the thermal boundary conductance based on the emitted phonon temperature increases with increasing temperature, caused by the increasing spectral heat capacity with increasing temperature.

Finally, for the comparisons with experiments, the thermal boundary conductance based on the equivalent equilibrium temperature is calculated by DOM in bilayer films formed by Al/Si. To better reproduce the situation in experiment [51], the thickness of Al is set as 100 nm, equal to that in the experiment. The thickness of Si substrate should be large enough to ensure that it is much larger than the mean free paths of phonons in Si, yet should not be too large to avoid significant computational consumption, and considering all factors, it is selected as 1000 nm. Since there is a lack of characterization of the interface, the interface roughness is difficult to determine. In the experiment, the thermal boundary conductance was measured after removing the natural oxide at Al/Si interface; consequently, the interface could be considered as a highest-quality one. Further referred to the measured interface roughness by transmission electron microscopy in Ref. [52], five interface roughnesses are selected, that is, 0, 0.02, 0.04, 0.06, and 0.3 nm, where 0 nm corresponds to the completely specular scattering. For comparisons with the results in Ref. [53], the interface roughness being infinite

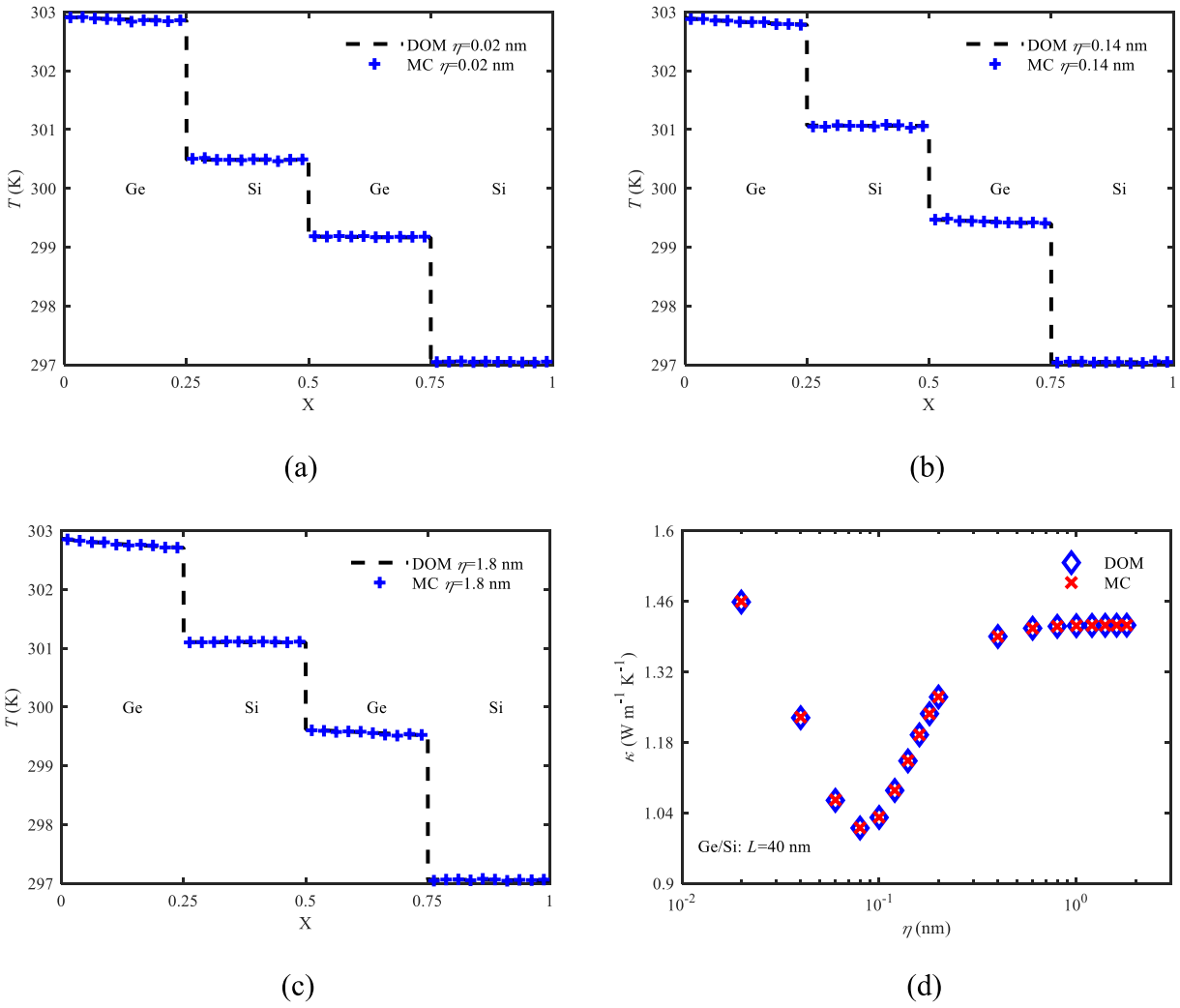

Fig. 13. The steady-state cross-plane temperature distributions and cross-plane thermal conductivities of Ge/Si multilayer films with the total thickness being 40 nm at various interface roughnesses: (a) the interface roughnesses being 0.02 nm, (b) the interface roughnesses being 0.14 nm, (c) the interface roughnesses being 1.8 nm and (d) the cross-plane thermal conductivities at various interface roughnesses.

is also simulated corresponding to the completely diffuse scattering. All spatial steps and relative errors to output the results are set as 0.01 nm and 1×10^{-7}, respectively, and the interface scattering is modeled by SMMM. With the thickness, interface roughness and phonon properties above, cross-plane interfacial phonon transport across bilayer films is simulated at various temperatures and the thermal boundary conductances based on the equivalent equilibrium temperature are calculated. Due to only five lattice thermal conductivities at five temperatures are given, that is, 100, 150, 200, 250 and 300 K [49], only five thermal boundary conductances are calculated at these temperatures. The temperatures at left and right boundaries of bilayer films are also set very small to match the small temperature difference assumption. For instance, to calculate the thermal boundary conductance at 100 K, fix the left and right isothermal boundaries at 101 and 99 K, respectively; to calculate the thermal boundary conductance at 200 K, fix the left and right isothermal boundaries at 203 and 197 K, respectively. The thermal boundary conductance based on the equivalent equilibrium temperature is calculated by

$$G = \frac{q}{\Delta T}, \tag{74}$$

where $\Delta T = T_1 - T_2$ is the equivalent equilibrium temperature jump at the interface with T_1 and T_2 being the equivalent equilibrium temperatures on the left and right sides of the interface, respectively.

The key to calculate the thermal boundary conductance based on the equivalent equilibrium temperature is to obtain the equivalent equilibrium temperature jump at the interface. Using DOM, the steady-state cross-plane temperature distribution is obtained and the temperature jump can thus be calculated. As mentioned above, due to the strong non-equilibrium effects at the interface, the temperature distribution near the interface is non-linearized. For the cross-plane temperature distributions in bilayer films, the equivalent temperatures of two nearest spatial points to the interface become closer and closer to the equivalent temperatures at the interface with decreasing spatial step. Since the spatial step in the present work is very small, it is inferred that the equivalent temperatures of two nearest spatial points to the interface are approximately equal to those at the interface. Thereby the equivalent equilibrium temperature jump at the interface can be directly obtained from the steady-state cross-plane temperature distribution. To verify this inference, the steady-state cross-plane temperature distributions are analyzed at different interface roughnesses and different temperatures. Fig. 9 gives the cross-plane temperature distributions at the interface roughnesses being 0 and 0.3 nm, and the referenced equilibrium temperatures being 100 and 300 K. For the cross-plane temperature distribution at the interface roughness being 0 nm and the referenced equilibrium temperature being 100 K in Fig. 9 (a), the temperatures of

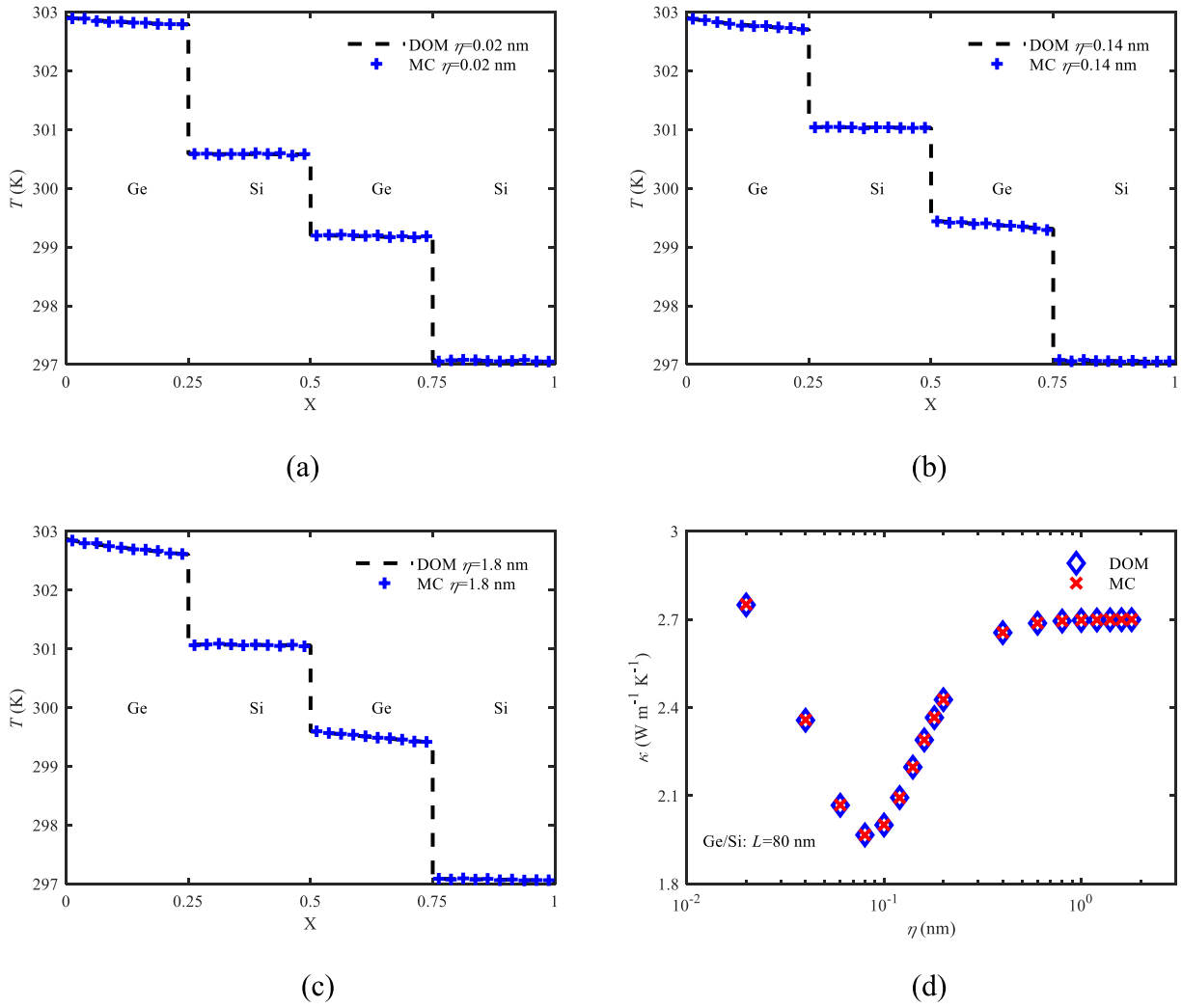

Fig. 14. The steady-state cross-plane temperature distributions and cross-plane thermal conductivities of Ge/Si multilayer films with the total thickness being 80 nm at various interface roughnesses: (a) the interface roughnesses being 0.02 nm, (b) the interface roughnesses being 0.14 nm, (c) the interface roughnesses being 1.8 nm and (d) the cross-plane thermal conductivities at various interface roughnesses.

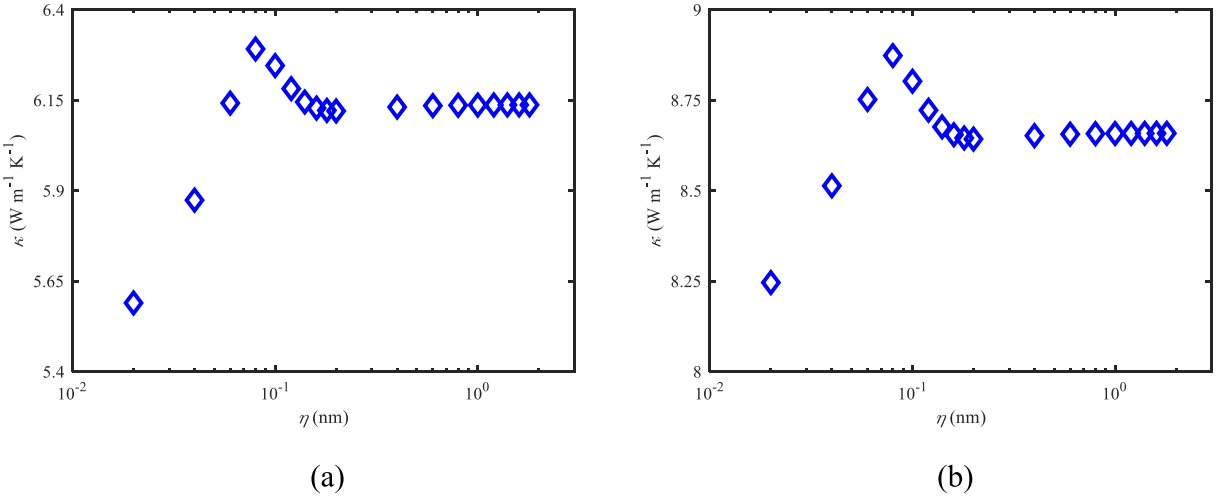

Fig. 15. The cross-plane thermal conductivities at various interface roughnesses in Al/Si bilayer films with two thicknesses: (a) the total thickness being 40 nm and each layer thickness being 20 nm, and (b) the total thickness being 80 nm and each layer thickness being 40 nm.

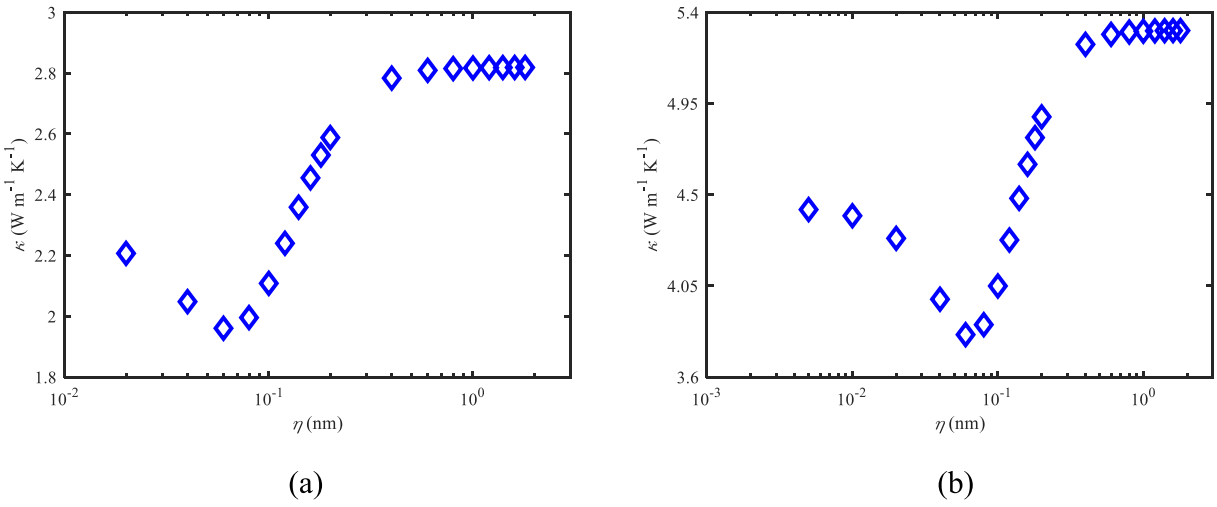

Fig. 16. The cross-plane thermal conductivities at various interface roughnesses in Ge/Si bilayer films with two thicknesses: (a) the total thickness being 40 nm and each layer thickness being 20 nm, and (b) the total thickness being 80 nm and each layer thickness being 40 nm.

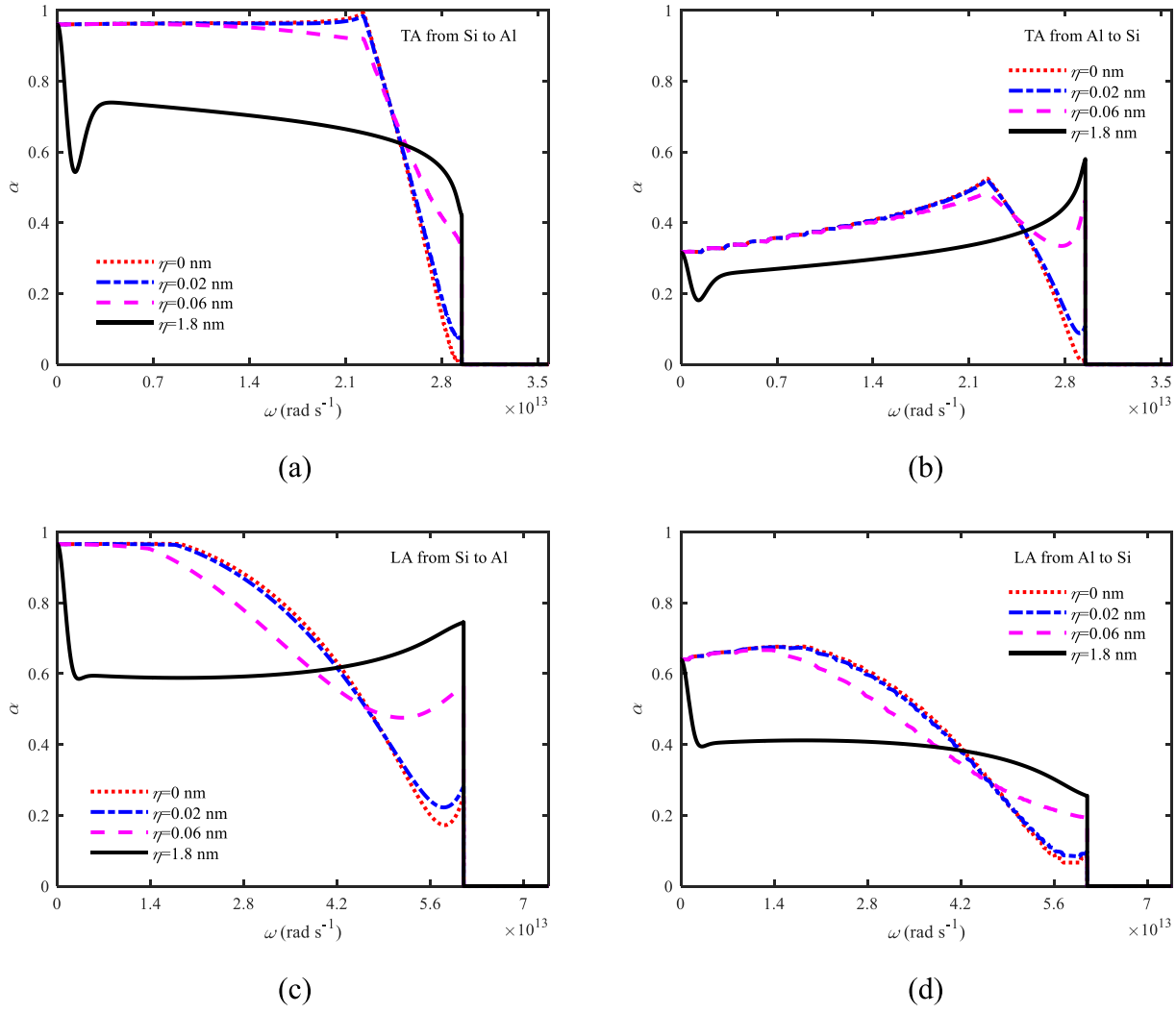

Fig. 17. The spectral transmissivities of phonons of Al/Si for various polarizations at various interface roughnesses: (a) the transverse acoustic phonons from Si to Al, (b) the transverse acoustic phonons from Al to Si, (c) the longitudinal acoustic phonons from Si to Al and (d) the longitudinal acoustic phonons from Al to Si. TA and LA denote the transverse acoustic and longitudinal acoustic phonons, respectively.

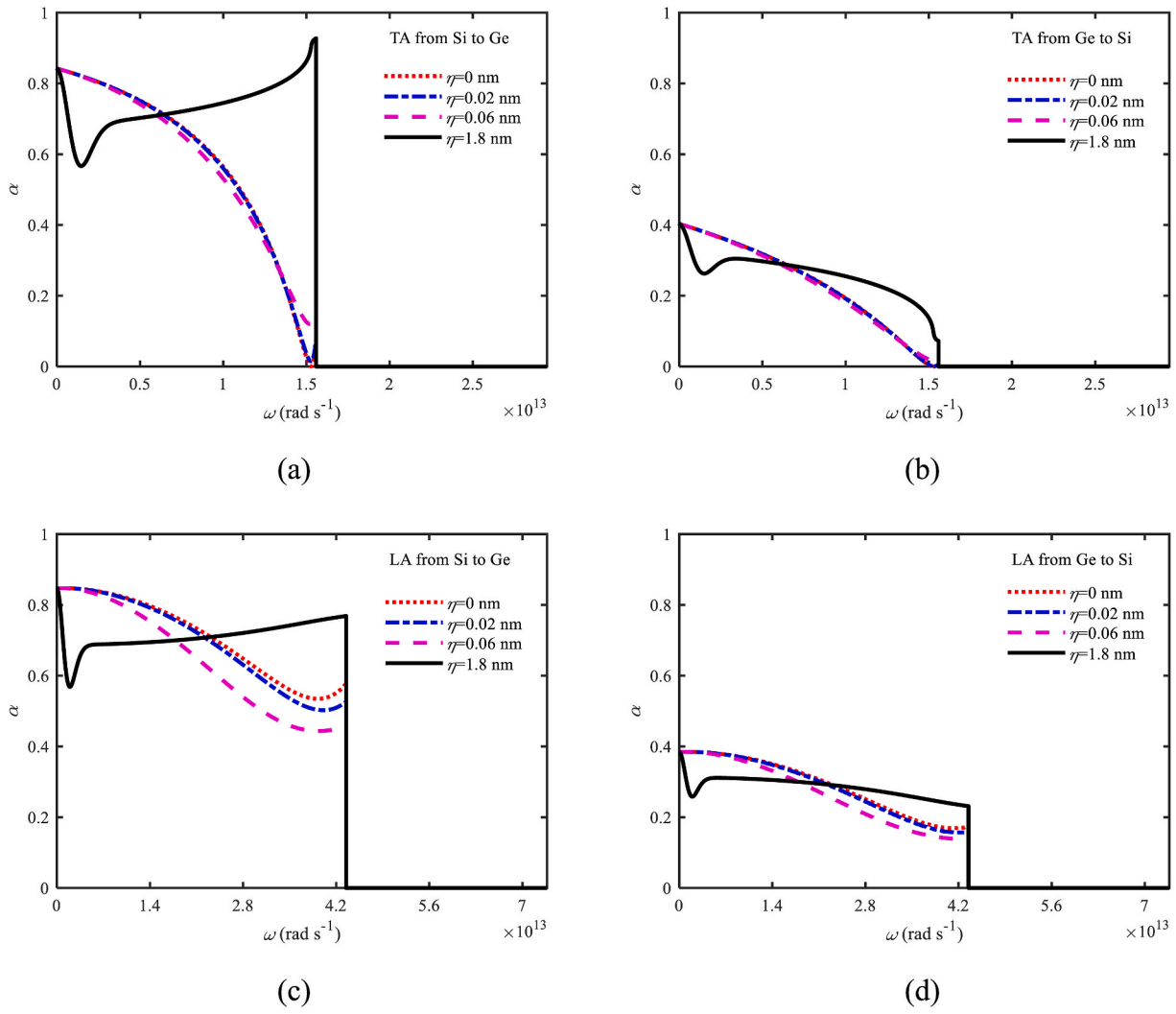

Fig. 18. The spectral transmissivities of phonons of Ge/Si for various polarizations at various interface roughnesses: (a) the transverse acoustic phonons from Si to Ge, (b) the transverse acoustic phonons from Ge to Si, (c) the longitudinal acoustic phonons from Si to Ge and (d) the longitudinal acoustic phonons from Ge to Si.

the first five spatial points with increasing distance from the interface to the inner points on Al side are 100.3165, 100.3165, 100.3164, 100.3164 and 100.3164 K, with a total temperature variation being 0.0001 K, much smaller than the total temperature variation in Al layer being 0.5950 K. The temperatures of the first five spatial points with increasing distance from the interface to the inner points on Si side are all 99.7010 K, much smaller than the total temperature variation in Si layer being 0.5614 K. For the cross-plane temperature distribution at the interface roughness being 0.3 nm and the referenced equilibrium temperature being 100 K in Fig. 9 (b), the temperatures of the first five spatial points with increasing distance from the interface to the inner points on Al side are 100.3050, 100.3049, 100.3049, 100.3049 and 100.3049 K, with a total temperature variation being 0.0001 K, much smaller than the total temperature variation in Al layer being 0.6135 K. The temperatures of the first five spatial points with increasing distance from the interface to the inner points on Si side are 99.9187, 99.9187, 99.9186, 99.9186 and 99.9186 K, with a total temperature variation being 0.0001 K, much smaller than the total temperature variation in Si layer being 0.7816 K. For the cross-plane temperature distribution at the interface roughness being 0 nm and the referenced equilibrium temperature being 300 K in Fig. 9 (c), the temperatures of the first five spatial points with increasing distance from the interface to the inner points on Al side are 300.1278, 300.1277, 300.1277, 300.1276 and 300.1276 K, with a total temperature variation being 0.0002 K, much smaller than the total temperature variation in Al layer being 2.7905 K. The temperatures of the first five spatial points with increasing distance from the interface to the inner points on Si side are all 299.4836 K, much smaller than the total temperature variation in Si layer being 2.4075 K. For the cross-plane temperature distribution at the interface roughness being 0.3 nm and the referenced equilibrium temperature being 300 K in Fig. 9 (d), the temperatures of the first five spatial points with increasing distance from the interface to the inner points on Al side are 300.1273, 300.1272, 300.1271, 300.1269 and 300.1268 K, with a total temperature variation being 0.0005 K, much smaller than the total temperature variation in Al layer being 2.7939 K. The temperatures of the first five spatial points with increasing distance from the interface to the inner points on Si side are 299.7206, 299.7206, 299.7205, 299.7205 and 299.7205 K, with a total temperature variation being 0.0001 K, much smaller than the total temperature variation in Si layer being 2.6459 K. The above conclusions are valid for all interface roughnesses and referenced equilibrium temperatures. These comparisons indicate that owing to the much small spatial step, the equivalent temperatures of two

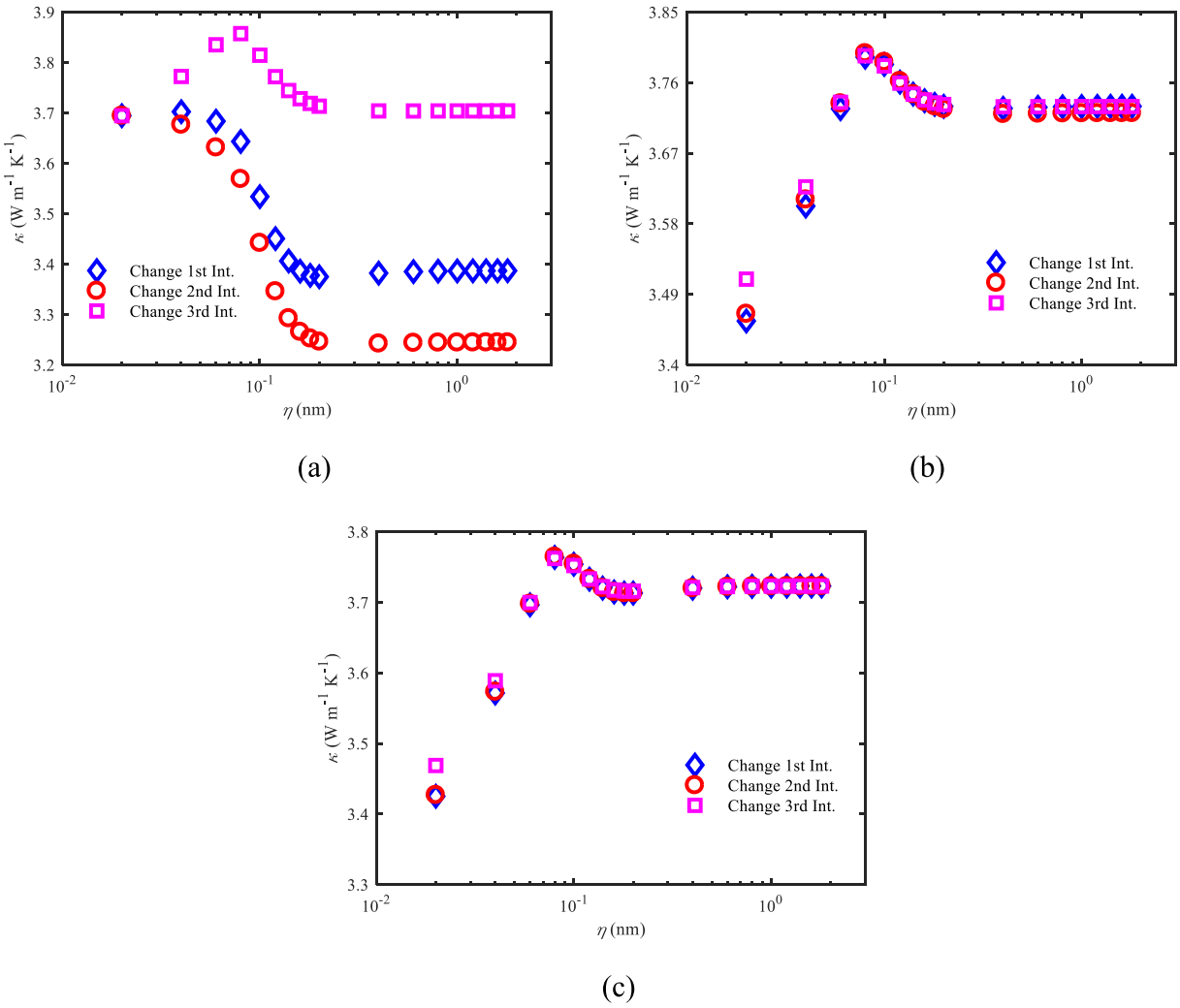

Fig. 19. The cross-plane thermal conductivities of Al/Si multilayer films with the total thickness being 40 nm with the nonidentical interface roughness: (a) fixing two interface roughnesses at 0.02 nm and changing another interface roughness, (b) fixing two interface roughnesses at 0.14 nm and changing another interface roughness, and (c) fixing two interface roughnesses at 1.8 nm and changing another interface roughness. The abbreviations, 1st Int., 2nd Int., and 3rd Int., denote the first, second, and third interfaces, respectively.

nearest spatial points to the interface approximately equal to those at the interface, and their difference approximately equals to the equivalent equilibrium temperature jump at the interface. Therefore, when the spatial step is very small, calculating the equivalent temperature difference of two nearest spatial points is an effective way to approximately obtain the equivalent equilibrium temperature jump at the interface.

After obtaining the equivalent equilibrium temperature jump at the interface, the thermal boundary conductance based on the equivalent equilibrium temperature is calculated using Eq. (74), shown in Fig. 10. The comparison shows that the thermal boundary conductances by DOM are close to the experimental results, and furthermore, these calculation results are closer and closer to the experiment with decreasing the interface roughness [51,53]. It demonstrates that the present DOM scheme for interface treatment can effectively capture the interface phonon scattering and it is inferred that the specular interface scattering makes a significant contribution to the cross-plane interfacial phonon transport in the experiment.

Overall, all above comparisons have validated the present DOM scheme of interface treatment with the spectral specularity and spectral transmissivity. It is adopted to simulate and investigate the roughness dependence of cross-plane interfacial phonon transport in multilayer films.

3.2. *Multilayer films*

In subsection 3.2, the DOM scheme constructed in section 2 for multilayer films is verified against Monte Carlo simulations in Ref. [16], adopting the previous interface treatment with the spectral specularity and spectral transmissivity.

The physical model is the four-layer film formed of two material pairs, that is, Al (1)/Si(2) and Ge (1)/Si(2), shown in Fig. 1 (b). Same with before, the dispersions of Al, Si and Ge are referred to Refs. [43–45] and the relaxation times of Si and Ge are referred to Ref. [46]. And the relaxation time of Al is obtained using the method in subsection 3.1 with the lattice thermal conductivities in Ref. [49]. The total thicknesses of multilayer films are selected as 40 and 80 nm with the thicknesses of

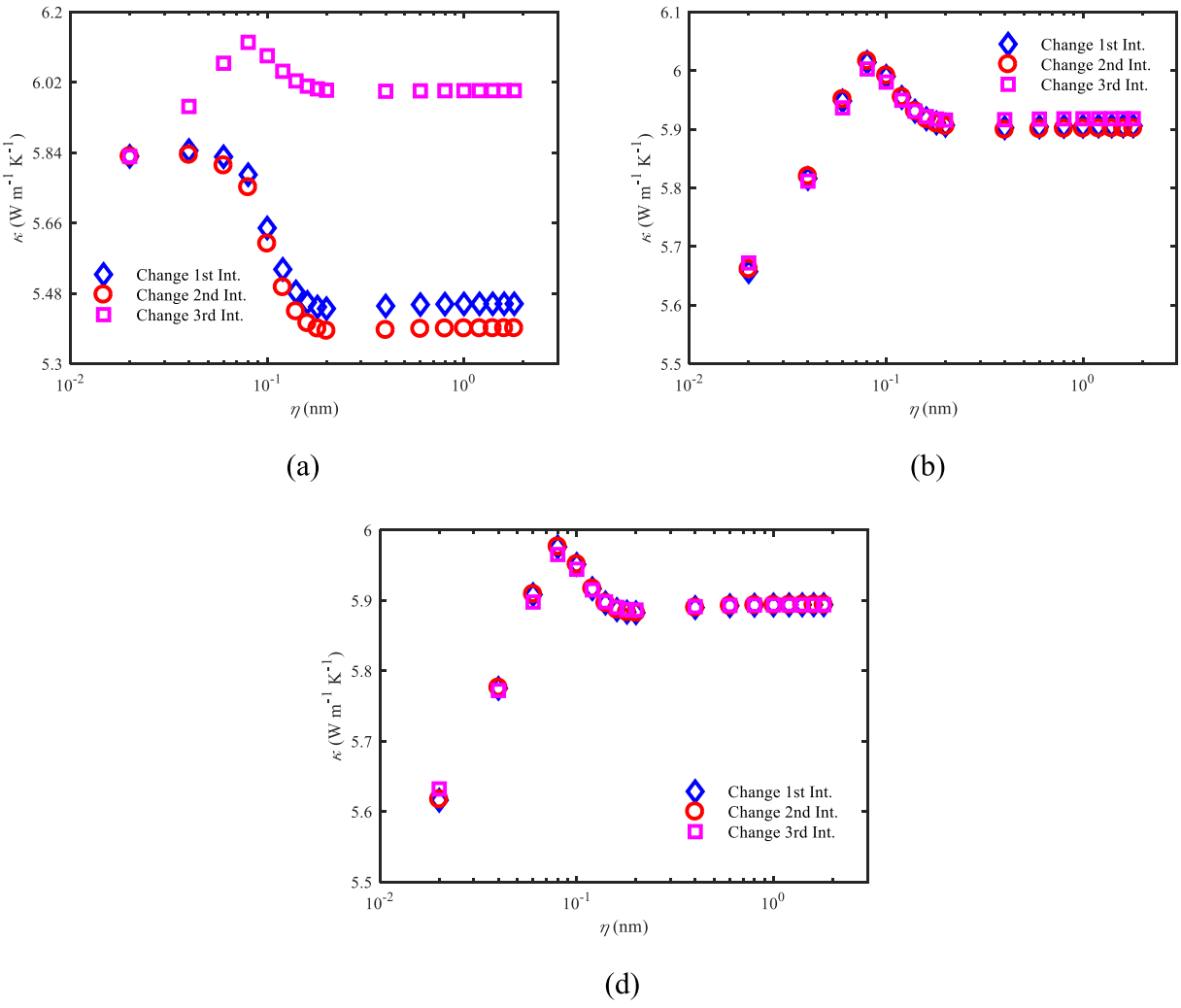

Fig. 20. The cross-plane thermal conductivities of Al/Si multilayer films with the total thickness being 80 nm with the nonidentical interface roughness: (a) fixing two interface roughnesses at 0.02 nm and changing another interface roughness, (b) fixing two interface roughnesses at 0.14 nm and changing another interface roughness, and (c) fixing two interface roughnesses at 1.8 nm and changing another interface roughness.

each layer as 10 and 20 nm, respectively, and the spatial steps in all simulations are fixed at 0.01 nm. The interface roughnesses of all three interfaces first increase from 0.02 to 0.2 nm with the common difference 0.02 nm and then increase from 0.2 to 1.8 nm with the common difference 0.02 nm. The left and right isothermal boundaries are fixed at 303 and 297 K. The convergence conditions for the interface boundary condition is that the relative error between two adjacent iteration steps of deviational intensities at the interface boundaries is smaller than 1×10^{-4}, and for the macroscopic information is that the relative errors between two adjacent iteration steps of both temperature and heat flux are all smaller than 1×10^{-8}. The relative errors are calculated by2

$$\varepsilon = \frac{\sum_{\mathrm{p}}\sum_{s}\sum_{j=1}^{N_\mu/2}\left|\left(\Psi^{\mathrm{right}}_{s,\mathrm{p},N_2+1,j}\right)^{n+1}-\left(\Psi^{\mathrm{right}}_{s,\mathrm{p},N_2+1,j}\right)^{n}\right|+\sum_{\mathrm{p}}\sum_{s}\sum_{j=N_\mu/2+1}^{N_\mu}\left|\left(\Psi^{\mathrm{left}}_{s,\mathrm{p},N_2+1,j}\right)^{n+1}-\left(\Psi^{\mathrm{left}}_{s,\mathrm{p},N_2+1,j}\right)^{n}\right|}{\sum_{\mathrm{p}}\sum_{s}\sum_{j=1}^{N_\mu/2}\left|\left(\Psi^{\mathrm{right}}_{s,\mathrm{p},N_2+1,j}\right)^{n}\right|+\sum_{\mathrm{p}}\sum_{s}\sum_{j=N_\mu/2+1}^{N_\mu}\left|\left(\Psi^{\mathrm{left}}_{s,\mathrm{p},N_2+1,j}\right)^{n}\right|}, \tag{75}$$

$$\varepsilon' = \frac{\sum_i\left|(T_i)^{n+1}-(T_i)^{n}\right|}{\sum_i\left|(T_i)^{n}\right|}, \tag{76}$$

$$\varepsilon'' = \frac{\sum_i\left|(q_i)^{n+1}-(q_i)^{n}\right|}{\sum_i\left|(q_i)^{n}\right|}, \tag{77}$$

where n is the index of the iteration step; ε, ε', and ε'' are the relative errors of deviational intensities at interface boundaries, temperature and

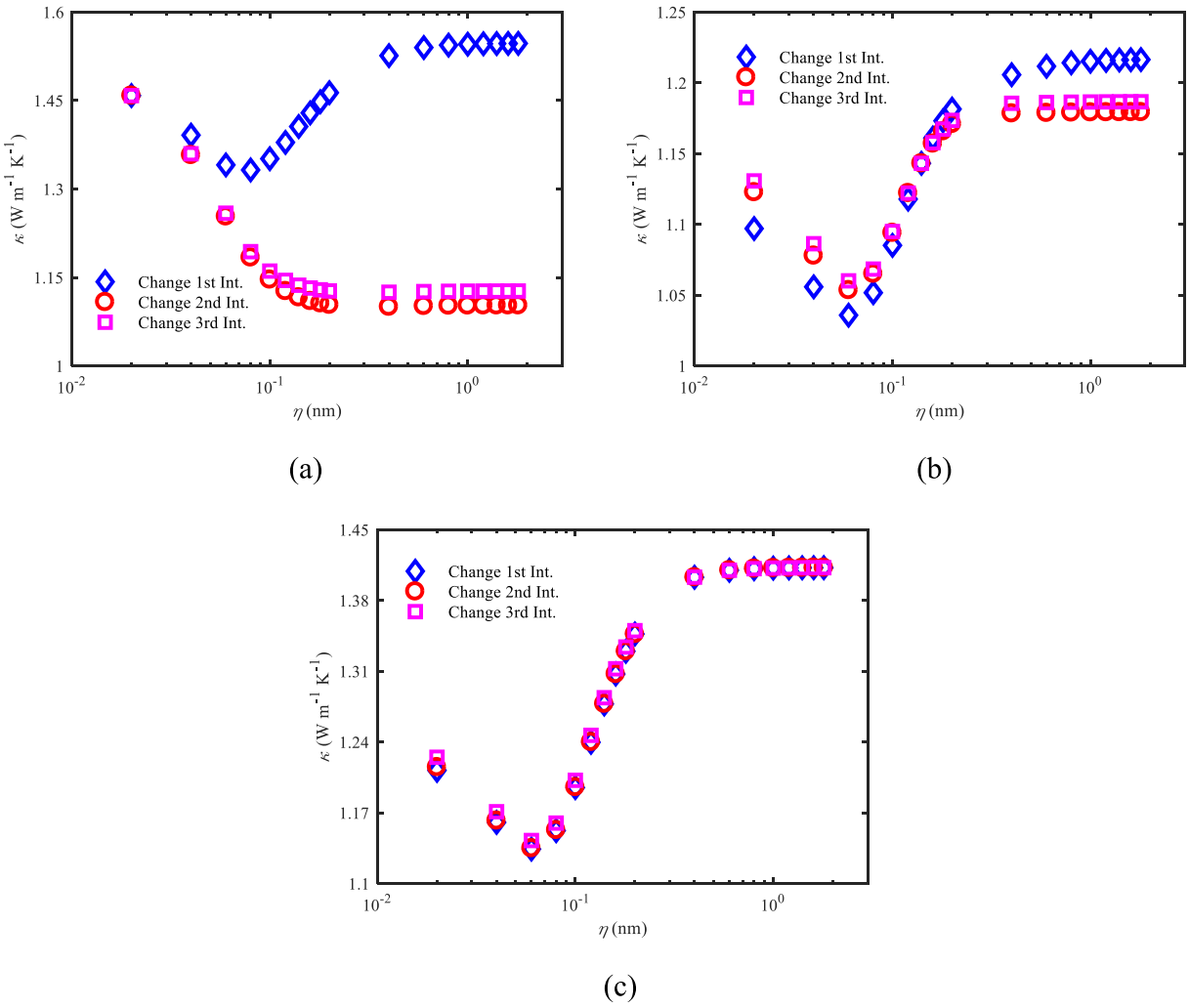

Fig. 21. The cross-plane thermal conductivities of Ge/Si multilayer films with the total thickness being 40 nm with the nonidentical interface roughness: (a) fixing two interface roughnesses at 0.02 nm and changing another interface roughness, (b) fixing two interface roughnesses at 0.14 nm and changing another interface roughness, and (c) fixing two interface roughnesses at 1.8 nm and changing another interface roughness.

heat flux, respectively. 1×10^{-4} and 1×10^{-8} are determined after a number of trials to obtain well convergent results. The steady-state cross-plane temperature distributions and heat flux are calculated by DOM using the scheme in section 2, and the cross-plane thermal conductivity is calculated based on Fourier's law, $\kappa = qL/\left(T^{\text{left}} - T^{\text{right}}\right)$ with the total thickness L. The cross-plane temperature distributions and thermal conductivities by DOM are compared with MC. Fig. 11(a)–(c), Fig. 12(a)–(c), Fig. 13(a)–(c) and Fig. 14(a)–(c) give the steady-state cross-plane temperature distributions of multilayer films formed by Al/Si and Ge/Si at the interface roughnesses as 0.02, 0.14 and 1.8 nm. And Fig. 11(d)–. 12 (d), Fig. 13 (d) and Fig. 14 (d) give the cross-plane thermal conductivities of multilayer films formed by Al/Si and Ge/Si at various roughnesses. The results by the present DOM scheme agree well with those by MC for multilayer films, demonstrating that the DOM scheme in section 2 can be well capable of simulating cross-plane interfacial phonon transport in multilayer films. In addition, the temperature jumps at the interfaces in multilayer films are much larger than those inside the materials, indicating that the non-equilibrium effects at the interfaces are much stronger than those inside the materials. And the maximum cross-plane thermal conductivities of Al/Si multilayer films and minimum cross-plane thermal conductivities of Ge/Si multilayer films are obtained at interface roughness as 0.08 and 0.08 nm, respectively, where the interface scattering is partially specular and partially diffuse.

4. Results and discussions

The present section adopts the DOM schemes with the interface treatment in section 2 to investigate the roughness dependence of cross-plane interfacial phonon transport in multilayer films. Four cases are calculated and analyzed, i.e. the cross-plane thermal conductivities with identical and nonidentical interface roughnesses and the thermal boundary conductances with identical and nonidentical interface roughnesses.

4.1. Cross-plane thermal conductivity with identical interface roughness

Subsection 4.1 presents the roughness dependence of cross-plane thermal conductivity of multilayer films with identical interface roughness for all interfaces. The physical model is the four-layer film formed of two material pairs, that is, Al (1)/Si(2) and Ge (1)/Si(2), shown in Fig. 1 (b). Same with section 3, the dispersions of Al, Si, and Ge are taken from Refs. [43–45] and the relaxation times of Si and Ge are taken from Ref. [46]. The relaxation time of Al is also calculated using the way in section 3 with the bulk lattice thermal conductivities in Ref. [49]. Two total thicknesses are considered, i.e. 40 and 80 nm, and the thicknesses of each layer of multilayer films are uniformly fixed at 10 and 20 nm to exclude the impact of the system size, and the spatial steps are all selected as 0.01 nm. The identical interface roughness means that

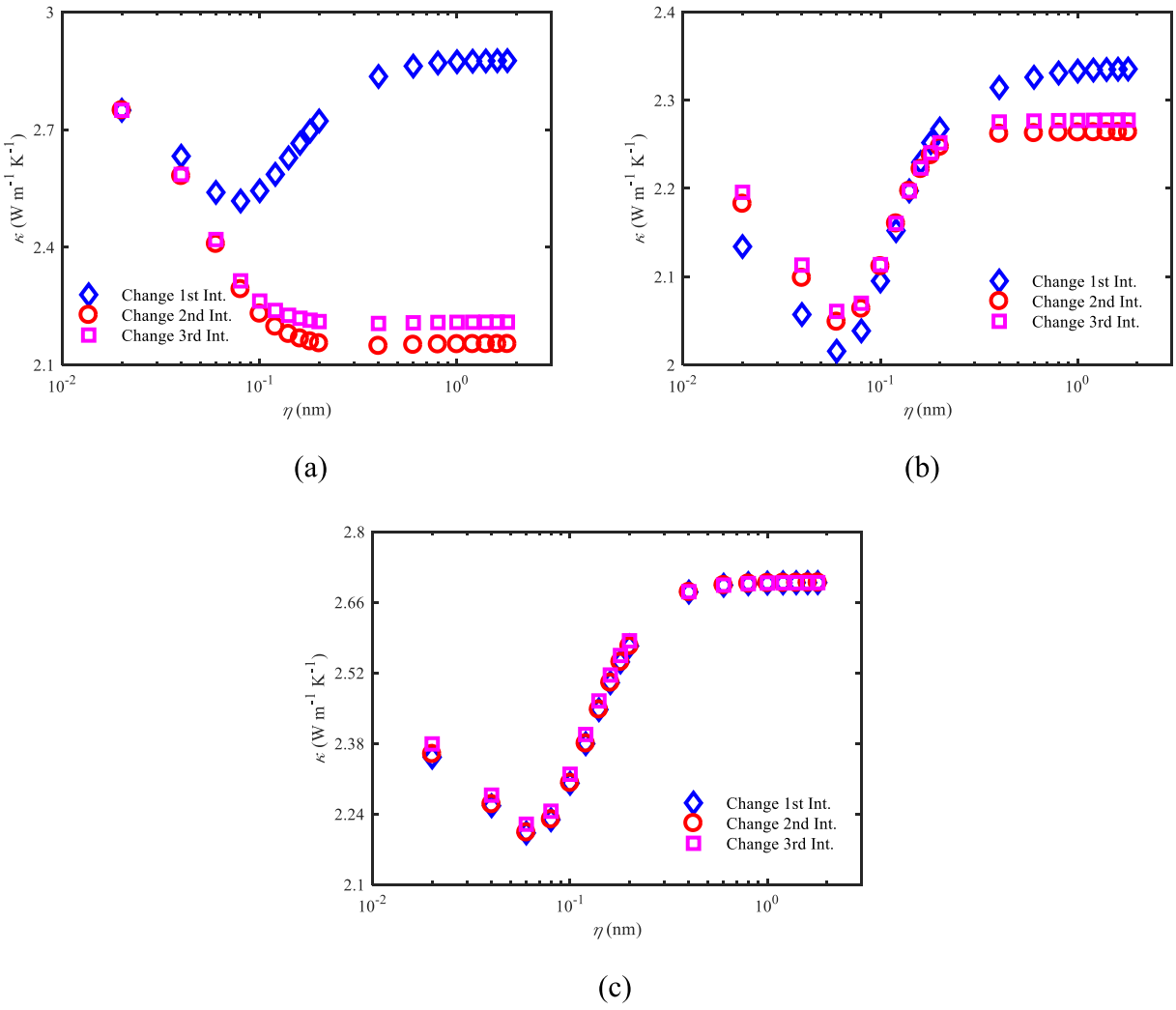

Fig. 22. The cross-plane thermal conductivities of Ge/Si multilayer films with the total thickness being 80 nm with the nonidentical interface roughness: (a) fixing two interface roughnesses at 0.02 nm and changing another interface roughness, (b) fixing two interface roughnesses at 0.14 nm and changing another interface roughness, and (c) fixing two interface roughnesses at 1.8 nm and changing another interface roughness.

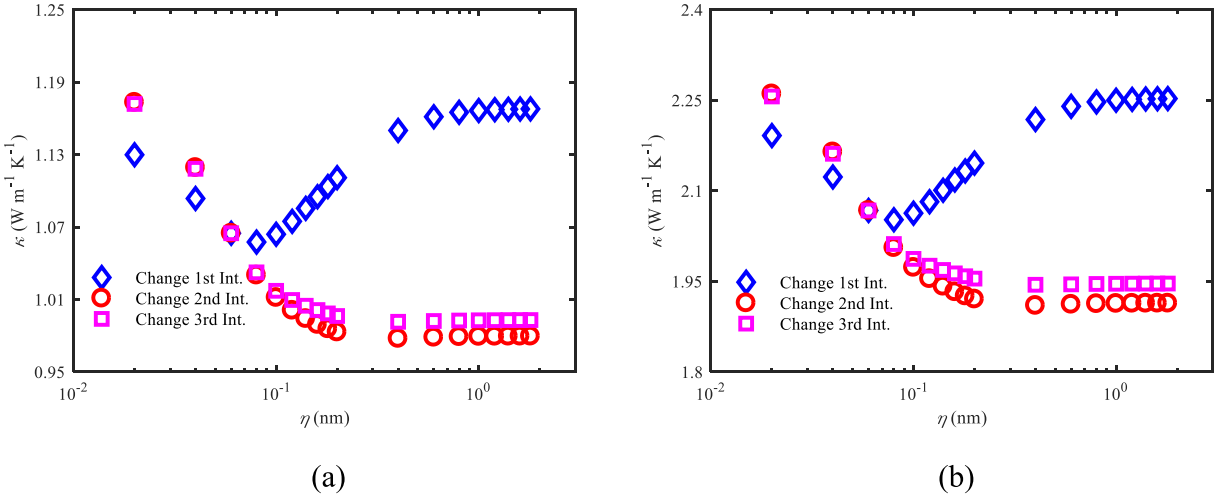

Fig. 23. The cross-plane thermal conductivities of Ge/Si multilayer films with two total thicknesses with the nonidentical interface roughness: (a) the total thickness being 40 nm with fixing two interface roughnesses at 0.06 nm and changing another interface roughness, and (b) the total thickness being 80 nm with fixing two interface roughnesses at 0.06 nm and changing another interface roughness.

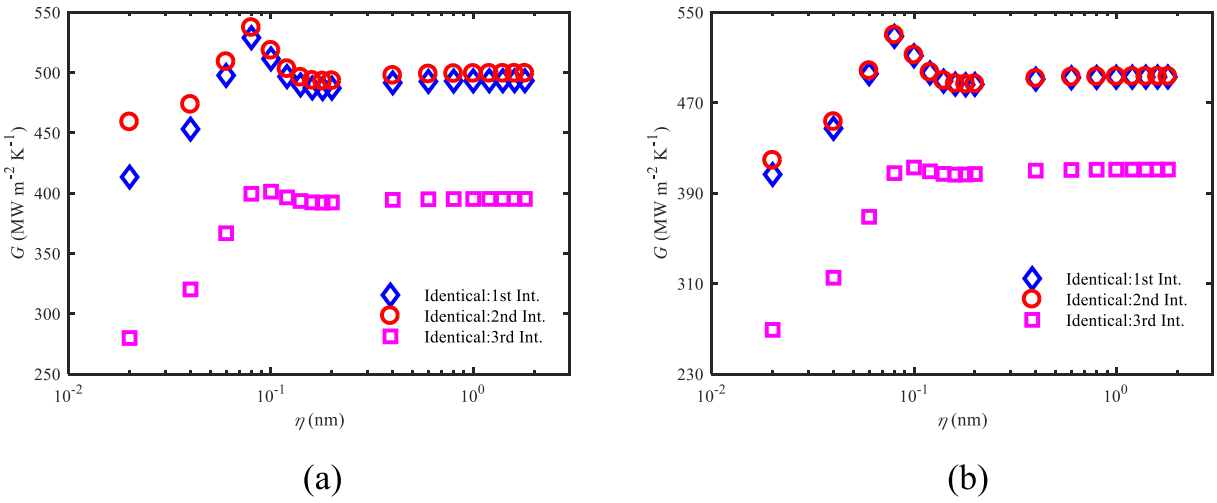

Fig. 24. The thermal boundary conductances at various interface roughnesses in Al/Si multilayer films with two thicknesses with the identical interface roughness: (a) the total thickness being 40 nm and each layer thickness being 10 nm, and (b) the total thickness being 80 nm and each layer thickness being 20 nm.

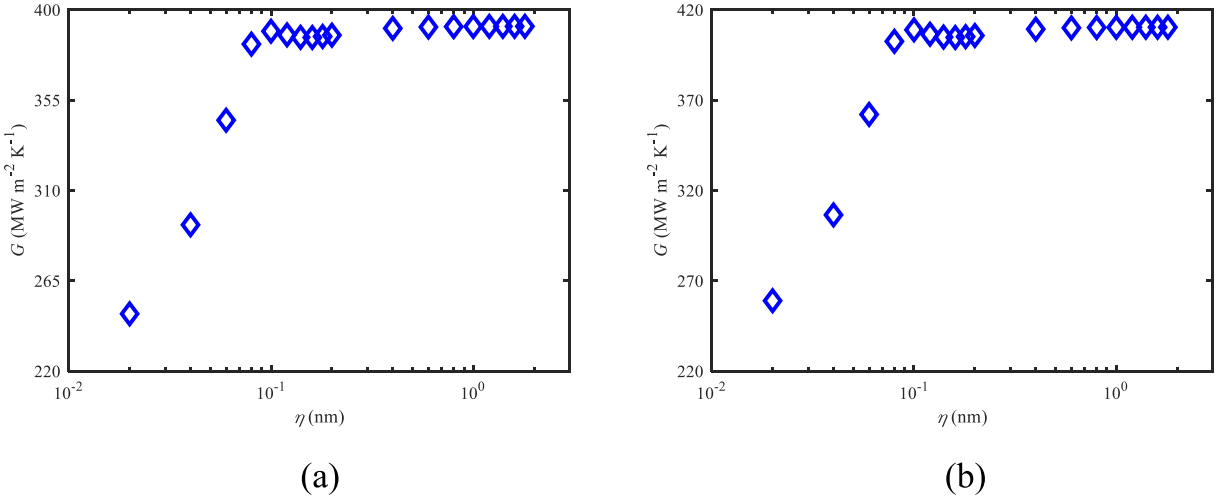

Fig. 25. The thermal boundary conductances at various interface roughnesses in Al/Si bilayer films with two thicknesses: (a) the total thickness being 20 nm and each layer thickness being 10 nm, and (b) the total thickness being 40 nm and each layer thickness being 20 nm.

the interface roughnesses of three interfaces are equal to each other, which first increase from 0.02 to 0.2 nm with the common difference 0.02 nm, and then increase from 0.2 to 1.8 nm with the common difference 0.02 nm. The left and right isothermal boundaries are fixed at 303 and 297 K, respectively. As subsection 3.2, the relative errors in convergence conditions for deviational intensities at interface boundaries and macroscopic information are selected as $1\times\ 10^{-4}$ and $1\times\ 10^{-8}$, respectively. When both interface boundary condition and macroscopic information are convergent, the results are output. With these results, the steady-state cross-plane temperature and heat flux are obtained and thus the cross-plane thermal conductivities are calculated by the formula, $\kappa = qL/\left(T^{\text{left}} - T^{\text{right}}\right)$.

Fig. 11(d), 12 (d), Fig. 13 (d) and Fig. 14 (d) show the cross-plane thermal conductivities at various interface roughnesses of Al/Si and Ge/Si multilayer films with total thicknesses as 40 and 80 nm. The cross-plane thermal conductivities at various interface roughnesses in Al/Si and Ge/Si bilayer films with the same total thickness with multilayer films and the thickness ratios being 1 are also shown in Figs. 15 and 16 for comparisons. The variation patterns in multilayer films for each material pair are similar at two total thicknesses. For Al/Si, the cross-plane thermal conductivity of the multilayer film first dramatically increases, and then dramatically decreases, and eventually tends to a constant. This trend is explained by the variation of the spectral transmissivity with the phonon frequency, shown in Fig. 17. When the interface roughness increases from 0 to 0.06 nm, the transmissivity for low- and high-frequency phonons decreases and increases slightly, respectively. The decrease is larger than the increase and thus the cross-plane thermal conductivity increases with increasing interface roughness. When the interface roughness further increases from 0.06 to 1.8 nm, the transmissivity for low-frequency phonons dramatically decreases whereas that for high-frequency phonons increases slightly, resulting in the dramatic decrease of the cross-plane thermal conductivity. The above variation pattern for multilayer films is similar to that for bilayer films, with different size relationships at large and small interface roughnesses. In detail, the cross-plane thermal conductivities at large and small interface roughnesses are close for multilayer films whereas the previous one is much larger than the latter one for bilayer films. The difference is mainly caused by the multi-interface coupling scattering in multilayer films, which increases the probability of phonons from the heat source reaching the heat sink by multiple reflections and transmissions.

The detailed explanation is as follows: (1) At small interface roughness, the transmissivities of high-frequency phonons are small and their reflectivity is large, and some of the emitted high-frequency phonons

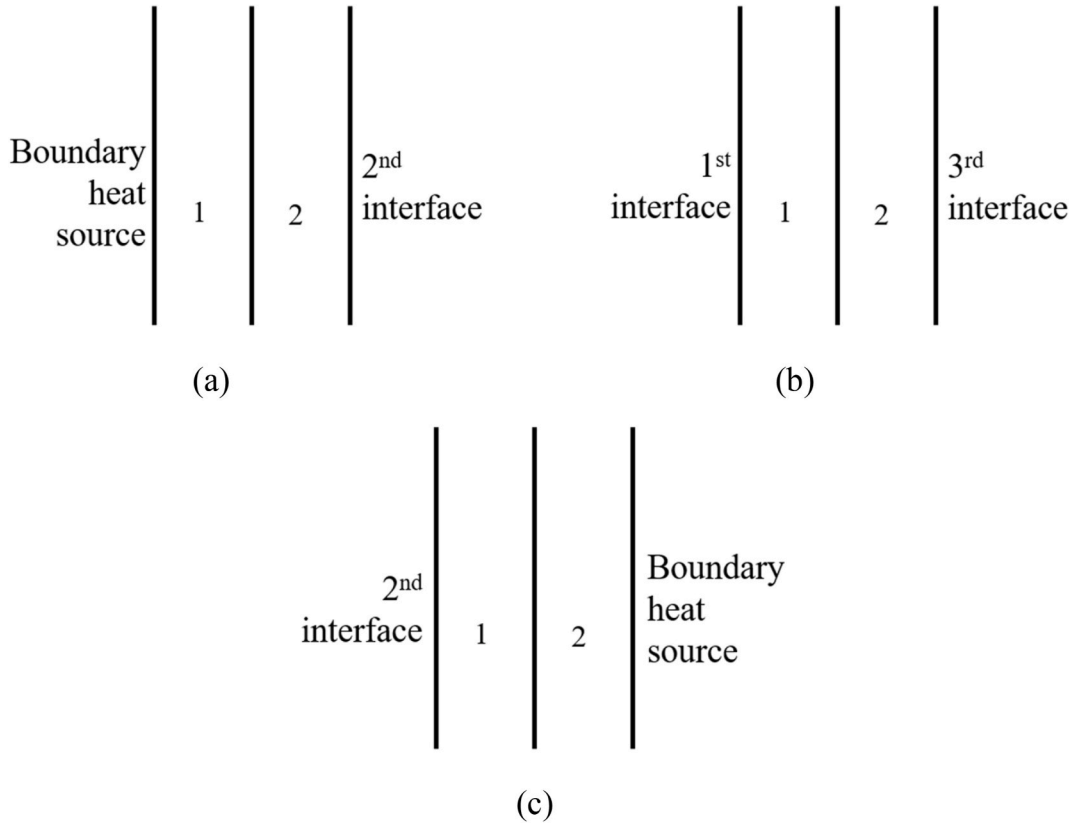

Fig. 26. Three bilayer films obtained by separating the multilayer film at one of its interfaces: (a) the bilayer film with the left isothermal boundary and the second interface, (b) the bilayer film with the first and third interfaces, and (c) the bilayer film with the right isothermal boundary and the second interface. The boundary heat sources in (a) and (c) denote the left and right isothermal boundaries, respectively.

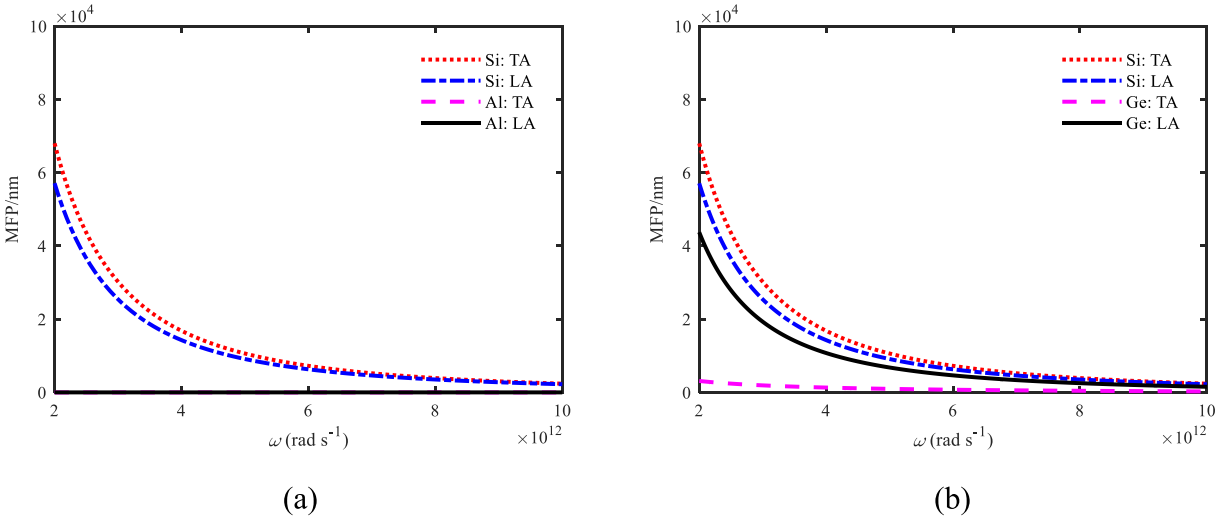

Fig. 27. The mean free paths (MFP) of phonons of each polarization for two material pairs: (a) Al/Si and (b) Ge/Si.

from the heat source are scattered at the second or third interface, and reflected back to be scattered by the first or second interface. Owing to the large reflectivity, they are more likely reflected and transport towards the heat sink again, increasing the cross-plane thermal conductivity of multilayer films. (2) At medium interface roughness, such as 0.06 nm, the transmissivities of low- and high-frequency phonons are close to and larger than those at small interface roughness, respectively. Thus on the one hand, the low-frequency phonons are more likely transport across the multilayer film and reach the heat sink owing to their large transmissivities; on the other hand, the high-frequency phonons are also more likely transport across the multilayer film and reach the heat sink after multiple reflections owing to their large reflectivity. These two factors makes the cross-plane thermal conductivity of multilayer films at medium interface roughness the largest. (3) At large interface roughness, the transmissivities of low- and high-frequency phonons are relatively large, and those of low-frequency phonons are smaller than those at small interface roughness. The large transmissivities make low- and high-frequency phonons less likely

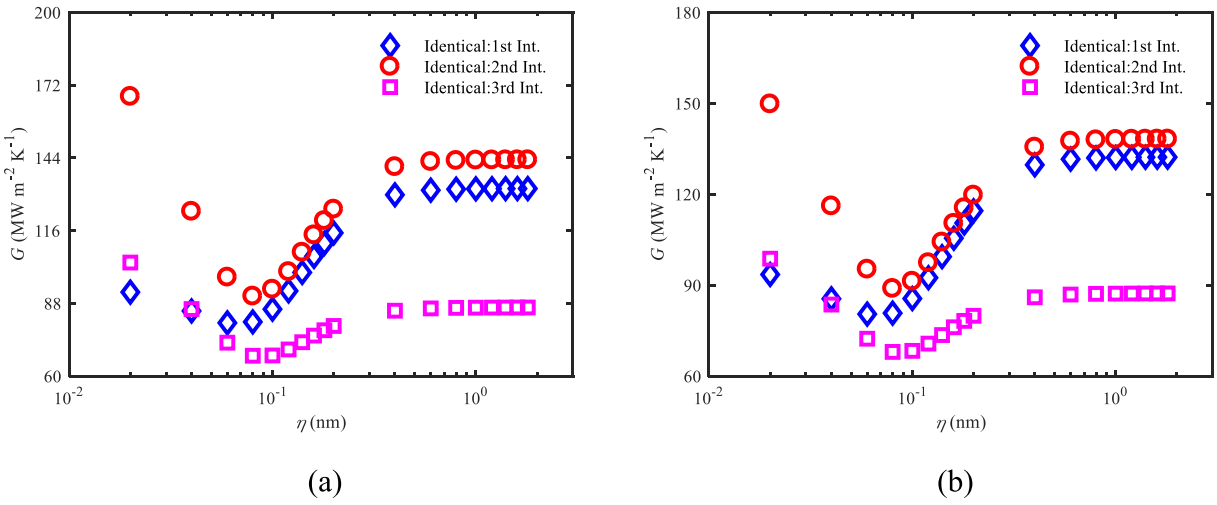

Fig. 28. The thermal boundary conductances at various interface roughnesses in Ge/Si multilayer films with two thicknesses with the identical interface roughness: (a) the total thickness being 40 nm and each layer thickness being 10 nm, and (b) the total thickness being 80 nm and each layer thickness being 20 nm.

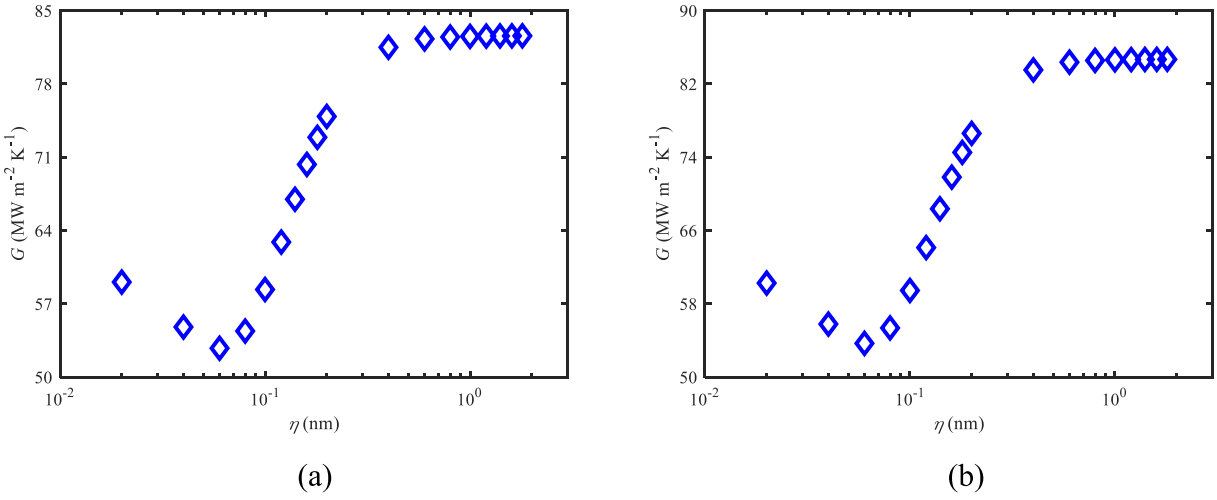

Fig. 29. The thermal boundary conductances at various interface roughnesses in Ge/Si bilayer films with two thicknesses: (a) the total thickness being 20 nm and each layer thickness being 10 nm, and (b) the total thickness being 40 nm and each layer thickness being 20 nm.

reflected by the first or second interface after their reflections at the second or third interface, and these phonons are more likely back to the heat source, decreasing the cross-plane thermal conductivity of the multilayer film. Yet owing to the large transmissivity, the cross-plane thermal conductivities of multilayer films at large interface roughnesses are still larger than those at small interface roughnesses, whereas their differences are not as large as those of bilayer films. Furthermore, it is worth noting that the above variation patterns of cross-plane thermal conductivity with interface roughness for Al/Si should depend on the interface model adopted in the present work. Take two most typical and different interface scattering mechanisms here as the comparisons. When adopting the interface models considering gray assumption, containing AMM, DMM and MMM, etc, the cross-plane thermal conductivities for multilayer films at large interface roughnesses are inferred to be much larger than those at small interface roughnesses. This is caused by that the spectral feature of the interface transmissivity is ignored in these interface models and thus its impact on the cross-plane thermal conductivity of multilayer films should be weakened. Therefore, this variation pattern of multilayer films considering the gray assumption is similar to that of bilayer film. For other cases considering the spectral transmissivity, elastic scattering and polarization conversion, the detailed variation of the cross-plane thermal conductivity of multilayer films with interface roughness is difficult to be predicted in advance, which is more complicated than the present case.

For Ge/Si, the cross-plane thermal conductivity of multilayer films first dramatically decreases, and then it dramatically increases, and eventually tends to a constant. This trend is also explained by the varying spectral transmissivity with the phonon frequency, shown in Fig. 18. When the interface roughness increases from 0 to 0.06 nm, the transmissivity for both low- and high-frequency phonons decreases slightly, resulting in the decreasing cross-plane thermal conductivity. When the interface roughness further increases from 0.06 to 1.8 nm, the increase of the transmissivity for high-frequency phonons is larger than the decrease of low-frequency phonons, resulting in the increasing cross-plane thermal conductivity. The above variation pattern for the multilayer film is similar to that for the bilayer film, with different size relationships at large and small interface roughnesses. The cross-plane thermal conductivities of multilayer films at small interface roughnesses are larger than that at large interface roughnesses, whereas the conclusion is opposite for bilayer films. This is also owing to the multiple reflections and transmissions caused by the multi-interface coupling scattering in multilayer films. The detailed explanation is as follows: (1) At small interface roughness, the transmissivities of high-frequency phonons are small or their reflectivity is large, and some of the

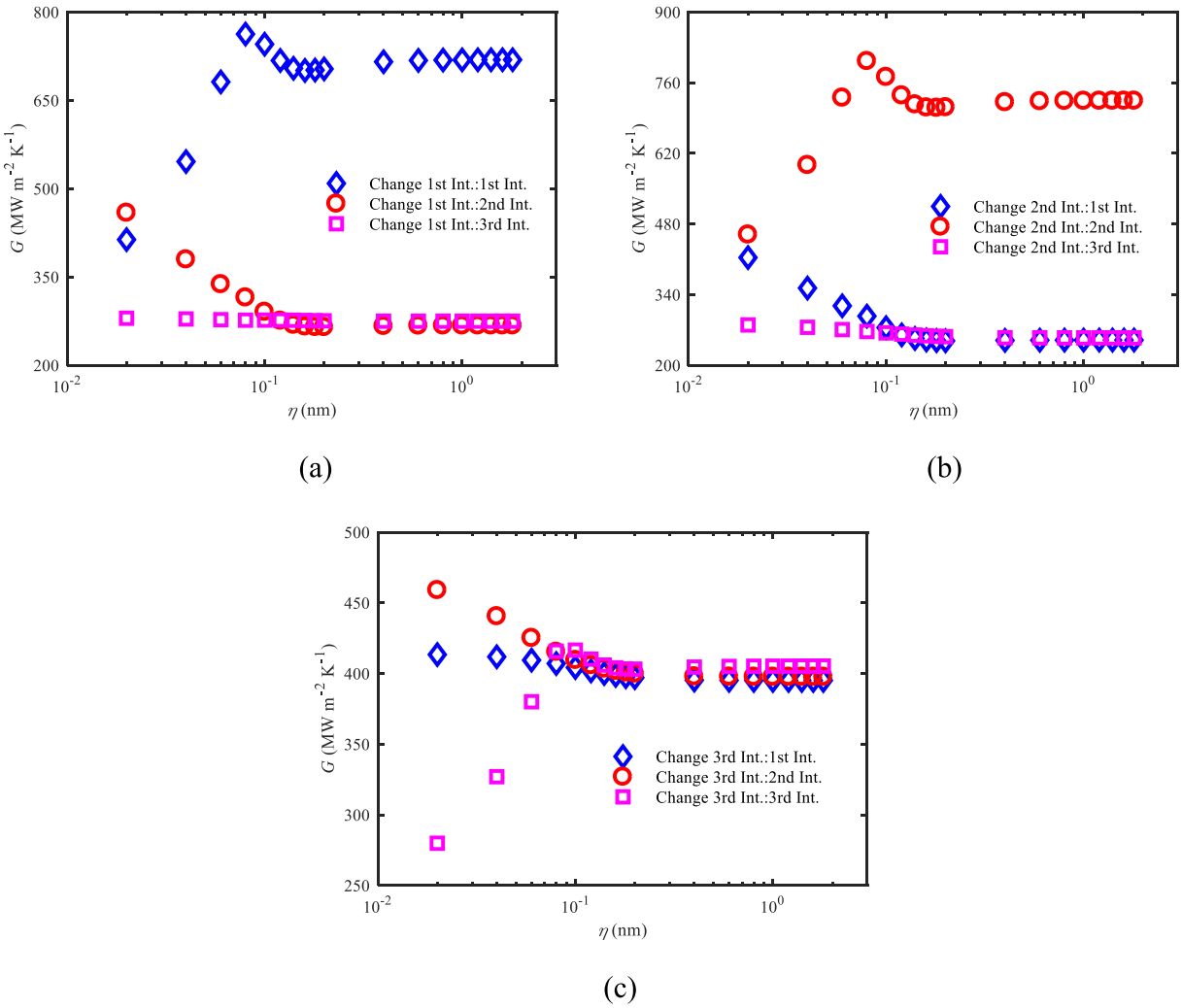

Fig. 30. The thermal boundary conductances of three interfaces in Al/Si multilayer films with the total thickness being 40 nm with the nonidentical interface roughness: (a) changing the first interface roughness and fixing two other interface roughnesses at 0.02 nm, (b) changing the second interface roughness and fixing two other interface roughnesses at 0.02 nm, and (c) changing the third interface roughness and fixing two other interface roughnesses at 0.02 nm.

emitted high-frequency phonons from the heat source are reflected by the second or third interface, and back to the first or second interface. Owing to the large reflectivity, they are more likely to undergo secondary reflection and transport towards the heat sink again, increasing the cross-plane thermal conductivity of multilayer films. (2) At large interface roughness, the transmissivities of high-frequency phonons are significantly larger than those at small interface roughness, which indicates the reflectivity of high-frequency phonons is significantly smaller than that at small interface roughness. The transmissivity of low-frequency phonons decreases less from small interface roughness to large interface roughness, resulting in a smaller increase in reflectivity. The small reflectivity at large interface roughness makes the probability of the reflection of low- and high-frequency phonons by the first or second interface small, and thus the reflected phonons at the second or third interface are more likely back to the heat source, decreasing the cross-plane thermal conductivity of the multilayer film. The above effects result in the larger cross-plane thermal conductivities at small interface roughnesses for multilayer films. Additionally, the above patterns of the cross-plane thermal conductivity varying with the interface roughness for Ge/Si also depend on the interface model adopted in the present work. Similar to Al/Si, when adopting the interface models considering the gray assumption, the variation pattern in multilayer films is similar to that for bilayer films since the spectral feature of its transmissivity is ignored. When considering the spectral transmissivity, elastic scattering and polarization conversion, the detailed variation of the cross-plane thermal conductivities for multilayer films with the interface roughness is also difficult to be predicted in advance.

4.2. Cross-plane thermal conductivity with nonidentical interface roughness

Subsection 4.2 presents the roughness dependence of cross-plane thermal conductivity of multilayer films with nonidentical interface roughness for all interfaces. The physical model is also the four-layer film formed of two material pairs, that is, Al (1)/Si(2) and Ge (1)/Si (2), shown in Fig. 1 (b). The dispersions and relaxation times of three materials, the total thickness, the thickness of each layer, the spatial steps, the relative errors in convergence conditions, and the left and right isothermal boundary temperatures are same with subsection 4.1. The nonidentical interface roughness means that the interface roughnesses of two interfaces are fixed and the another one is changed, which first increases from 0.02 to 0.2 nm with the common difference 0.02 nm, and then increases from 0.2 to 1.8 nm with the common difference 0.02 nm. The cross-plane thermal conductivities are calculated after obtaining the steady-state cross-plane temperature and heat flux distributions with formula, $\kappa = qL/\left(T^{\text{left}} - T^{\text{right}}\right)$, shown in Figs. 19–21 and 22.

For Al/Si, when fixing two interface roughnesses at 0.02 nm and changing another interface roughness, as shown in Fig. 19 (a) and

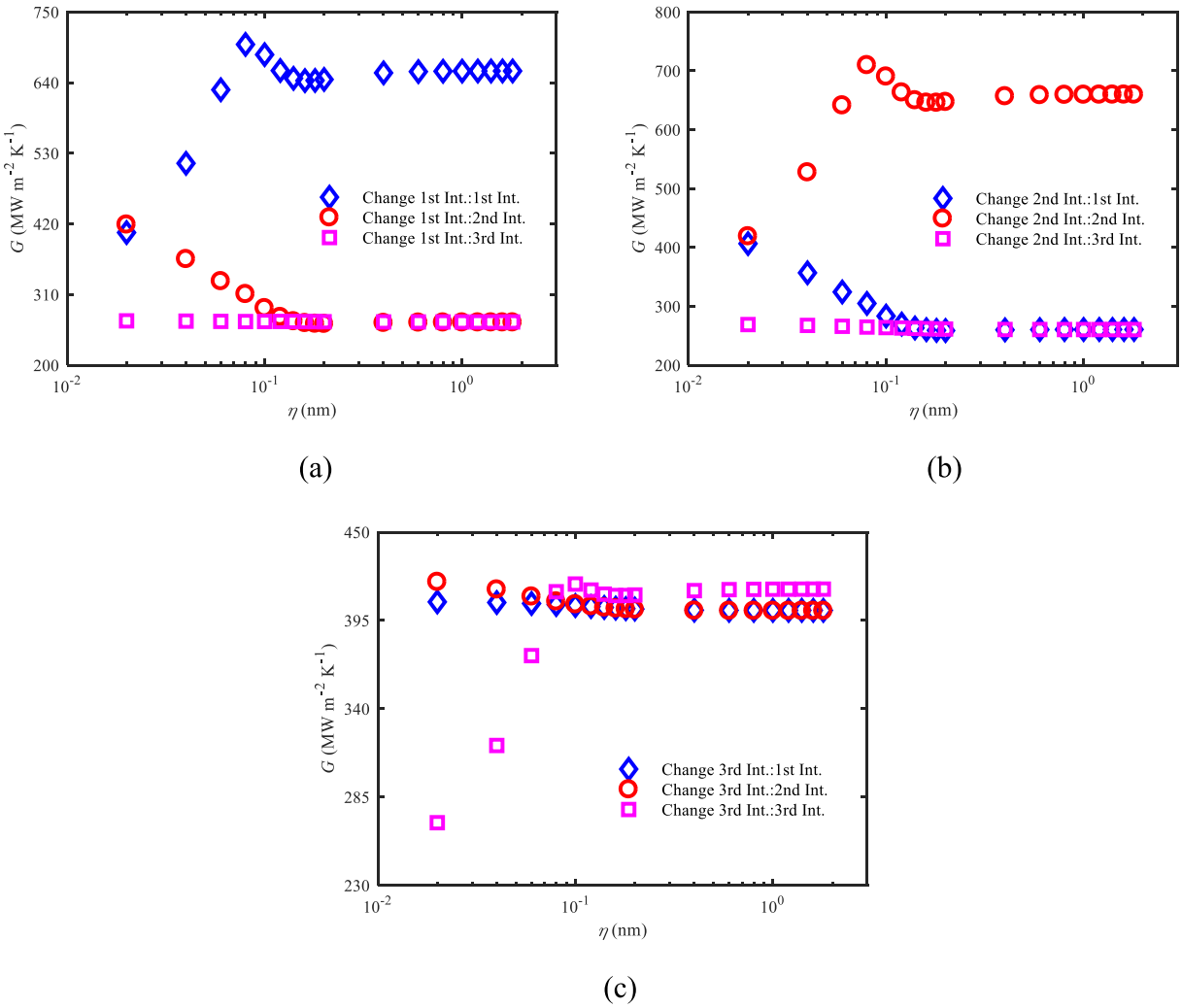

Fig. 31. The thermal boundary conductances of three interfaces in Al/Si multilayer films with the total thickness being 80 nm with the nonidentical interface roughness: (a) changing the first interface roughness and fixing two other interface roughnesses at 0.02 nm, (b) changing the second interface roughness and fixing two other interface roughnesses at 0.02 nm, and (c) changing the third interface roughness and fixing two other interface roughnesses at 0.02 nm.

Fig. 20 (a), there are generally three conclusions with details as follows: (1) Increasing the first interface roughness, on the one hand, as Fig. 17 shows, the overall transmissivity of the first interface increases, resulting in increasing its thermal boundary conductance and thus the cross-plane thermal conductivity. Whereas at large interface roughnesses, the increase of the overall transmissivity is not significant and thus the increase of cross-plane thermal conductivity is not significant. On the other hand, the transmissivities of low- and high-frequency phonons decrease and increase with increasing the interface roughness, respectively. This means that the amounts of low- and high-frequency phonons transmitting across the first interface decrease and increase, respectively. The transmissivities of high-frequency phonons at the second and third interfaces are very small owing to the small interface roughness. Thereby many high-frequency phonons transmitting across the first interface are reflected by the second and third interfaces, causing the decrease of the cross-plane thermal conductivity. The above effects lead to that the cross-plane thermal conductivity almost keeps constant at small interface roughnesses and decreases at large interface roughnesses. (2) Increasing the second interface roughness, on the one hand, as Fig. 17 shows, the overall transmissivity of the second interface increases, resulting in increasing its thermal boundary conductance and thus the cross-plane thermal conductivity. Whereas at large interface roughnesses, the increase of the overall transmissivity is not significant and thus the increase of cross-plane thermal conductivity is not significant. On the other hand, the transmissivities of high-frequency phonons are small at the first interface owing to its interface roughness is small, hence most phonons transmitting across the first interface are low-frequency. With increasing the second interface roughness, the transmissivities of low-frequency phonons at the second interface decrease and those of high-frequency phonons increase. This makes most low-frequency phonons transmitting across the first interface reflected by the second interface, causing the decrease of the cross-plane thermal conductivity. The above effects lead to that the cross-plane thermal conductivity almost keeps constant at small interface roughnesses and decreases at large interface roughnesses. (3) Increasing the third interface roughness, on the one hand, as Fig. 17 shows, the overall transmissivity of the third interface increases, resulting in increasing its thermal boundary conductance and thus the cross-plane thermal conductivity. Yet at large interface roughnesses, the increase of the overall transmissivity is not significant and thus the increase of the cross-plane thermal conductivity is not significant. On the other hand, the transmissivities of high-frequency phonons are small at the first and second interfaces owing to their interface roughnesses are small, hence most phonons transmitting across the first and second interfaces are low-frequency. With increasing the third interface roughness, the transmissivities of low-frequency phonons at the third interface decrease and those of high-frequency phonons increase. Thus most low-frequency phonons transmitting across the first and second interfaces are

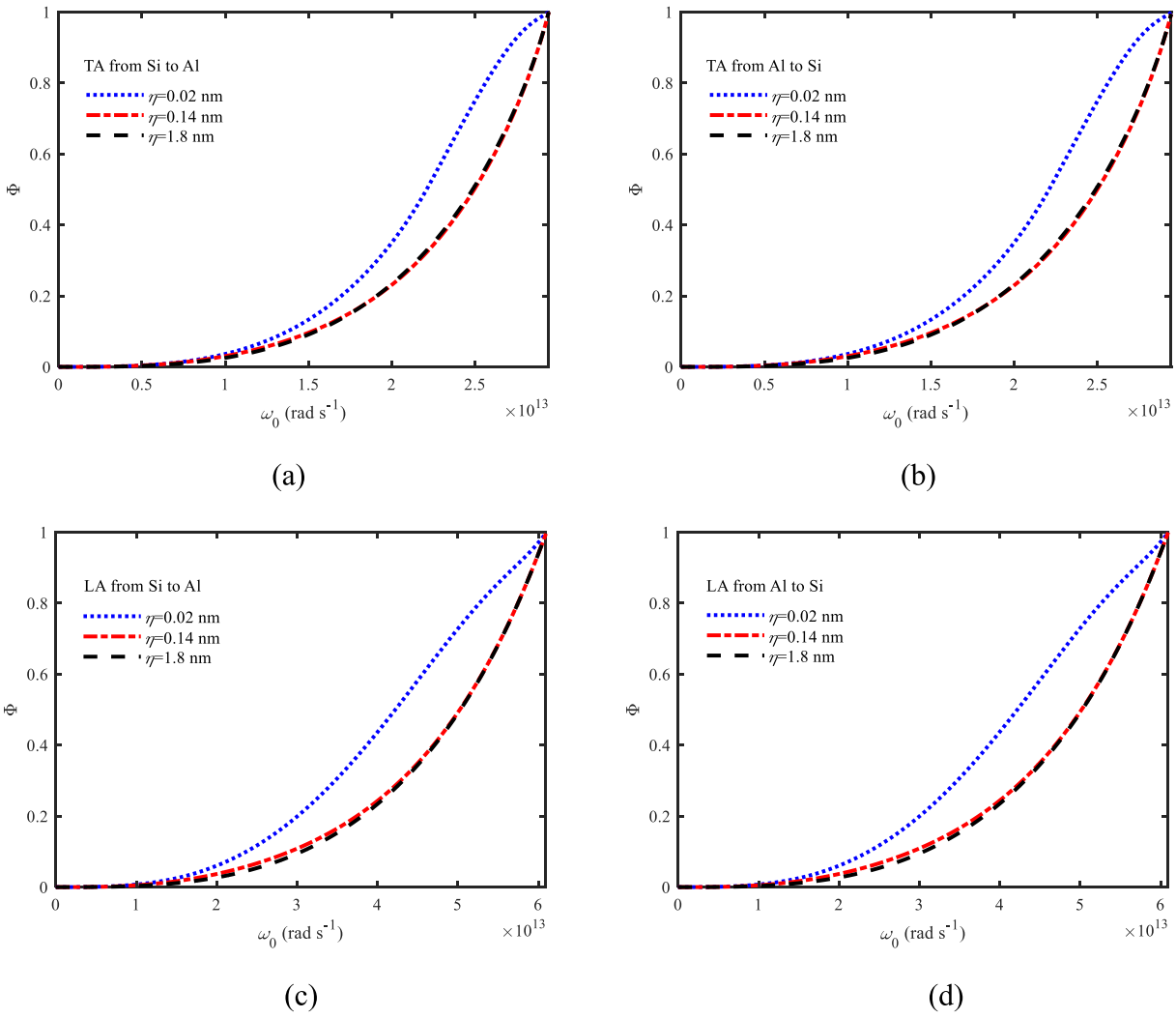

Fig. 32. The cumulative distributions of thermal boundary conductance of each polarization for Al/Si at three interface roughnesses: (a) the transverse acoustic phonons from Si to Al, (b) the transverse acoustic phonons from Al to Si, (c) the longitudinal acoustic phonons from Si to Al and (d) the longitudinal acoustic phonons from Al to Si.

reflected by the third interface, causing the significant decrease of the cross-plane thermal conductivity. The above effects lead to that the cross-plane thermal conductivity increases and decreases at small and large interface roughnesses, respectively.

For Al/Si, when fixing two interface roughnesses at 0.14 nm and changing another interface roughness, as shown in Fig. 19 (b) and Fig. 20 (b), there are also generally three conclusions with details as follows: (1) Increasing the first interface roughness, on the one hand, as Fig. 17 shows, the overall transmissivity of the first interface increases, resulting in increasing its thermal boundary conductance and thus the cross-plane thermal conductivity. Whereas at large interface roughnesses, the increase of overall transmissivity is not significant and thus the increase of cross-plane thermal conductivity is not significant. On the other hand, the transmissivities of low- and high-frequency phonons decrease and increase with increasing interface roughness, respectively. It means that the amounts of low- and high-frequency phonons transmitting across the first interface decrease and increase, respectively. The transmissivities of low- and high-frequency phonons at the second and third interfaces are relatively large owing to their interface roughnesses are moderate, and thus their reflection probabilities are small. Thereby the decrease of the cross-plane thermal conductivity caused by the reflection of phonons is small at the second and third interfaces. The above effects lead to that the cross-plane thermal conductivity first increases and then tends to a constant with increasing the first interface roughness. (2) Increasing the second interface roughness, on the one hand, as Fig. 17 shows, the overall transmissivity of the second interface increases, resulting in increasing its thermal boundary conductance and thus the cross-plane thermal conductivity. Whereas at large interface roughnesses, the increase of the overall transmissivity is not significant and thus the increase of cross-plane thermal conductivity is not significant. On the other hand, the transmissivities of low- and high-frequency phonons decrease and increase at the second interface, respectively, with increasing its interface roughness. It means that the amounts of low- and high-frequency phonons transmitting across the second interface decrease and increase, respectively. The transmissivities of low- and high-frequency phonons at the first and third interfaces are relatively large owing to their interface roughnesses are moderate, and thus their reflection probabilities are small. Thereby the decrease of the cross-plane thermal conductivity caused by the reflection of phonons is small at the third interfaces. The above effects lead to that the cross-plane thermal conductivity first increases and then tends to a constant with increasing the second interface roughness. (3) Increasing the third interface roughness, on the one hand, as Fig. 17 shows, the overall transmissivity of the third interface increases, resulting in increasing its thermal boundary conductance and thus the cross-plane thermal conductivity. Yet at large interface roughness, the increase of the overall

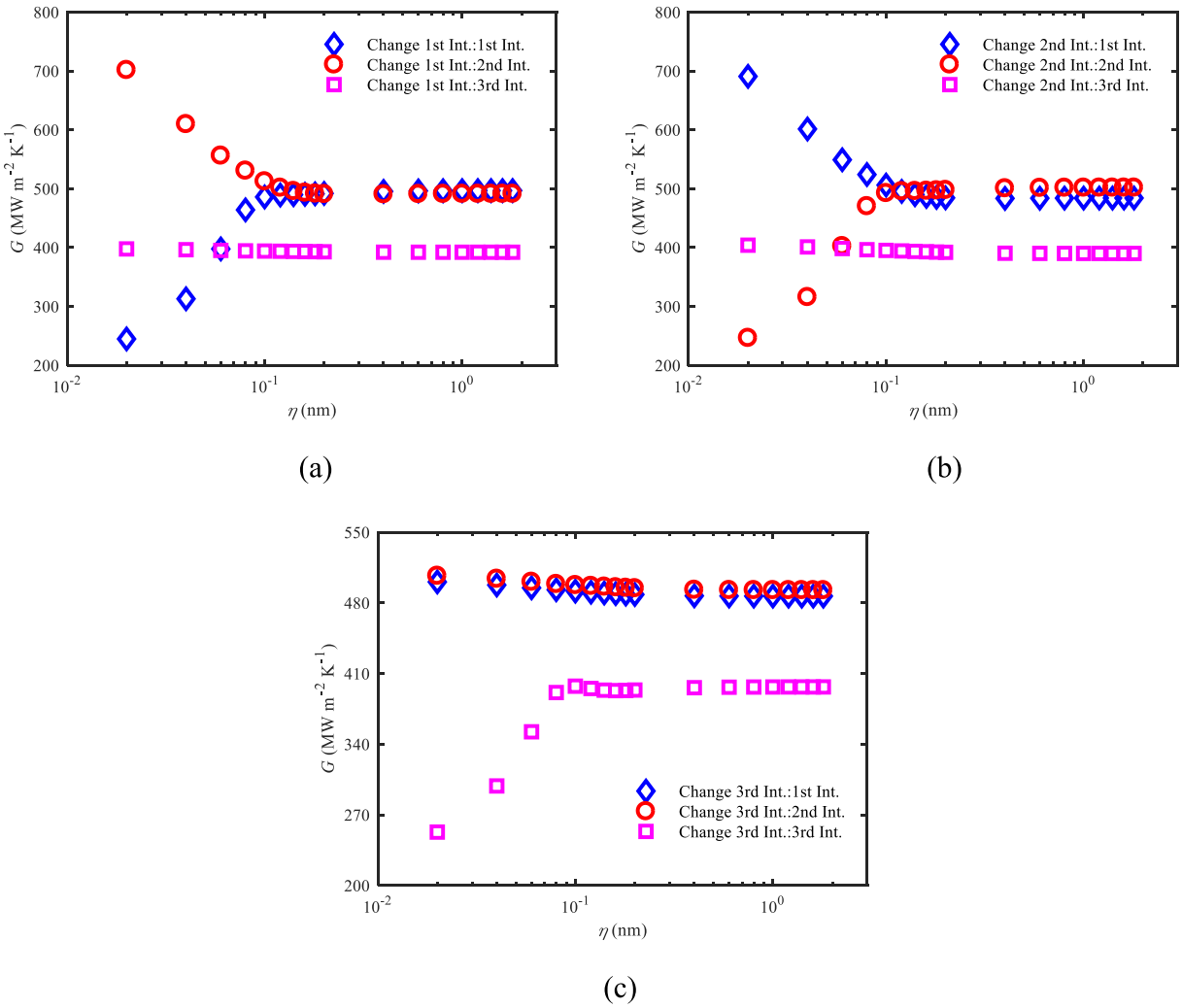

Fig. 33. The thermal boundary conductances of three interfaces in Al/Si multilayer films with the total thickness being 40 nm with the nonidentical interface roughness: (a) changing the first interface roughness and fixing two other interface roughnesses at 0.14 nm, (b) changing the second interface roughness and fixing two other interface roughnesses at 0.14 nm, and (c) changing the third interface roughness and fixing two other interface roughnesses at 0.14 nm.

transmissivity is not significant and thus the increase of cross-plane thermal conductivity is not significant. On the other hand, the transmissivities of low- and high-frequency phonons are moderate at the first and second interfaces owing to their interface roughnesses are moderate, hence the amount of low-frequency phonons transmitting across the first and second interfaces is comparable to that of high-frequency phonons. The impacts of increasing the third interface roughness on the transmission probabilities of low- and high-frequency phonons are comparable, which makes the cross-plane thermal conductivity almost keep constant. The above effects lead to that the cross-plane thermal conductivity first increases and then tends to a constant with increasing the third interface roughness. In addition, for three cases, i.e. fixing the first and second interface roughnesses at 0.14 nm and setting the third interface roughness to be a small one, fixing the second and third interface roughnesses at 0.14 nm and setting the first interface roughness to be a small one, and fixing the first and third interface roughnesses at 0.14 nm and setting the second interface roughness to be a small one, the cross-plane thermal conductivities of the latter two cases are smaller than the former one due to many high-frequency phonons are reflected back to the heat source by the first and second interfaces.

For Al/Si, when fixing two interface roughnesses at 1.8 nm and changing another interface roughness, as shown in Fig. 19 (c) and Fig. 20 (c), there are also generally three conclusions. These conclusions and the corresponding explanation are same with the case when fixing two interface roughnesses at 0.14 nm and changing another interface roughness, hence no further elaboration is provided here. In addition, for Al/Si, fixing two interface roughnesses at 0.02 nm and setting the first or second interface roughness as 0.14 or 1.8 nm, or fixing two interface roughnesses at 0.14 or 1.8 nm and setting the first or second interface roughness as 0.02 nm, give smaller cross-plane thermal conductivities than the minimum cross-plane thermal conductivities with the identical interface roughness. This conclusion is different from the prediction using one-dimensional thermal resistance network model based on the classical law, Fourier's law, which gives the minimum cross-plane thermal conductivity at the identical and small interface roughness for Al/Si [54]. This observation is caused by different roughness dependences of the spectral transmissivity at different interface roughnesses, and it provides a new way to manipulate the cross-plane thermal conductivity of the multilayer film. The detailed explanation is as follows: When the second and third interfaces or the first and third interfaces are fixed at small interface roughnesses, the low-frequency phonons more likely transmit across these two interfaces and the high-frequency phonons are more likely reflected back. And fixing the first or second interface at large interface roughnesses, the low-frequency phonons are more likely reflected back, and the increase of transmission probability of the high-frequency phonons is small. These interface roughness settings greatly reflect the phonons back to the heat source and further reduce the cross-plane thermal conductivity.

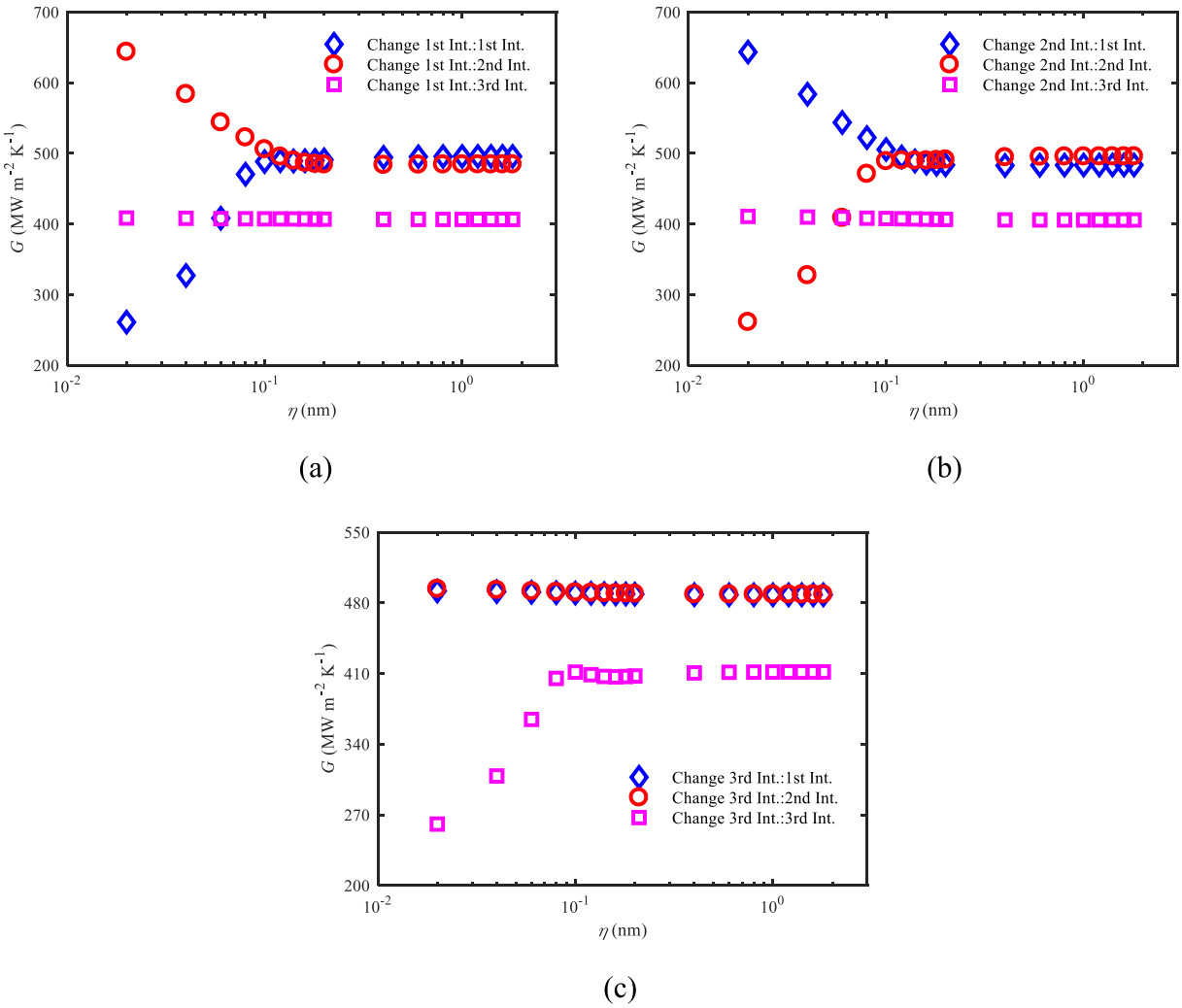

Fig. 34. The thermal boundary conductances of three interfaces in Al/Si multilayer films with the total thickness being 80 nm with the nonidentical interface roughness: (a) changing the first interface roughness and fixing two other interface roughnesses at 0.14 nm, (b) changing the second interface roughness and fixing two other interface roughnesses at 0.14 nm, and (c) changing the third interface roughness and fixing two other interface roughnesses at 0.14 nm.

Similarly, when the second and third interfaces or the first and third interfaces are fixed at large interface roughnesses, the high-frequency phonons more likely transmit across these two interfaces and the low-frequency phonons are more likely reflected back. And fixing the first or second interface at small interface roughnesses, the high-frequency phonons are more likely reflected back, and the increase of transmission probability of the low-frequency phonons is small. These interface roughness settings also greatly reflect the phonons back to the heat source and further reduce the cross-plane thermal conductivity of the multilayer film.

For Ge/Si, when fixing two interface roughnesses at 0.02 nm and changing another interface roughness, as shown in Fig. 21 (a) and Fig. 22 (a), there are generally three conclusions with details as follows: (1) Increasing the first interface roughness, on the one hand, as Fig. 18 shows, the overall transmissivity of the first interface first increases and then decreases, resulting in its thermal boundary conductance and the cross-plane thermal conductivity of multilayer films to first increase and then decrease. On the other hand, with increasing interface roughness, the transmissivities of both low- and high-frequency phonons first decrease and then those of low- and high-frequency phonons slightly decrease and dramatically increase, respectively. This means that the amount of low-frequency phonons transmitting across the first interface decreases, and that of high-frequency phonons first slightly decreases and then dramatically increases. Owing to the interface roughness is small, the transmissivities of high-frequency phonons are very small at the second and third interfaces. Thereby many high-frequency phonons transmitting across the first interface are reflected by the second and third interfaces, causing the decrease of the cross-plane thermal conductivity. The above effects lead to that the cross-plane thermal conductivity of multilayer films decreases and increases at small and large interface roughnesses, respectively. (2) Increasing the second interface roughness, on the one hand, as Fig. 18 shows, the overall transmissivity of the second interface first increases and then decreases, resulting in its thermal boundary conductance and the cross-plane thermal conductivity of multilayer films to first increase and then decrease. On the other hand, the transmissivities of high-frequency phonons are small at the first interface owing to its small interface roughness, hence most phonons transmitting across the first interface are low-frequency. With increasing the second interface roughness, the transmissivities of both low- and high-frequency phonons first decrease, and then those of low- and high-frequency phonons slightly decrease and dramatically increase, respectively. This makes many low-frequency phonons transmitting across the first interface reflected by the second interface, causing the decrease of the cross-plane thermal conductivity. The above effects lead to the decrease of the cross-plane thermal conductivity of multilayer films. (3) Increasing the third interface roughness, on the one hand, as Fig. 18 shows, the overall transmissivity of the third interface first increases and then decreases, resulting in its thermal boundary

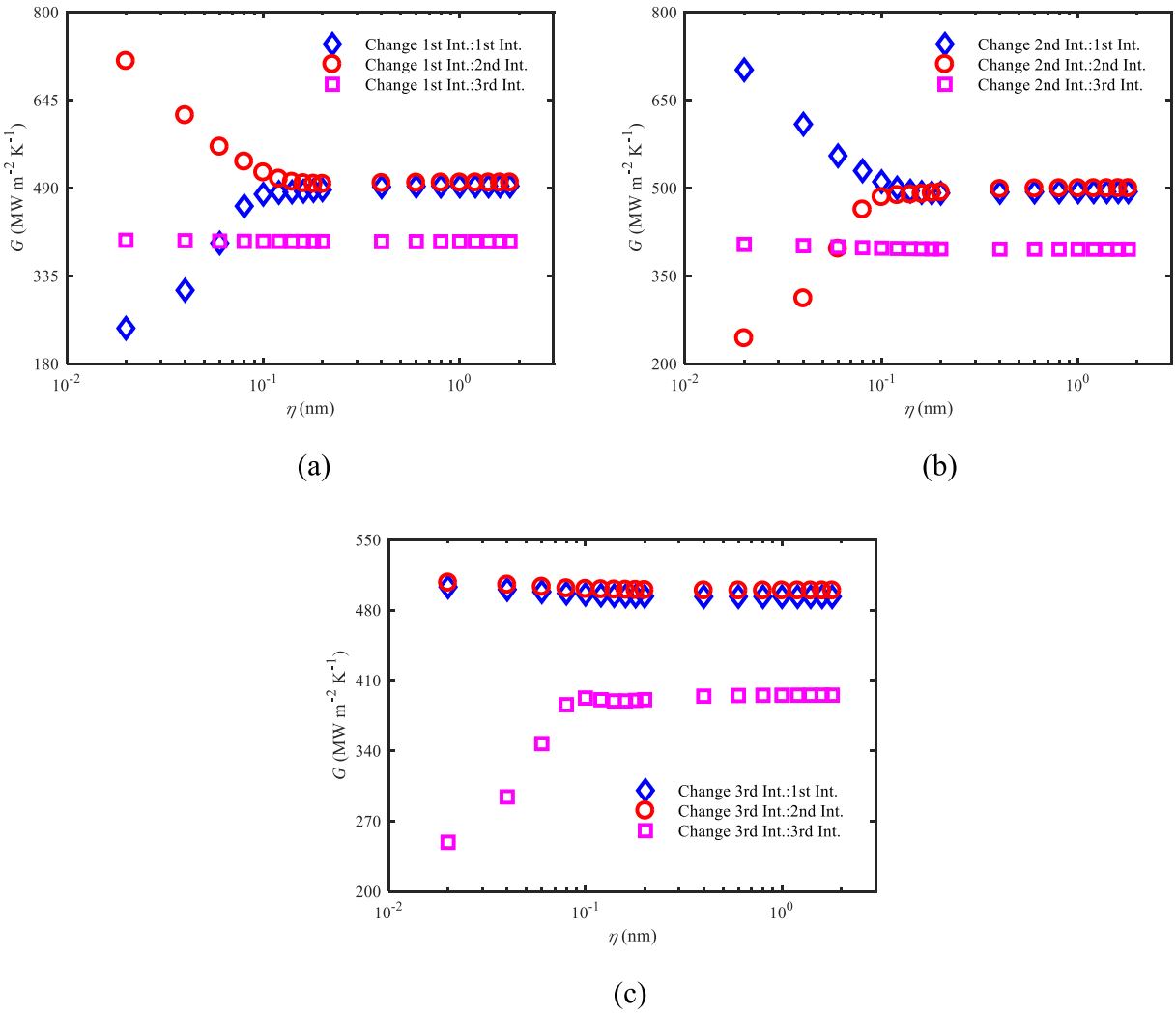

Fig. 35. The thermal boundary conductances of three interfaces in Al/Si multilayer films with the total thickness being 40 nm with nonidentical interface roughness: (a) changing the first interface roughness and fixing two other interface roughnesses at 1.8 nm, (b) changing the second interface roughness and fixing two other interface roughnesses at 1.8 nm, and (c) changing the third interface roughness and fixing two other interface roughnesses at 1.8 nm.

conductance and the cross-plane thermal conductivity of multilayer films to first increase and then decrease. On the other hand, the transmissivities of high-frequency phonons are small at the first and second interfaces owing to their interface roughnesses are small, hence most phonons transmitting across the first and second interfaces are low-frequency. With increasing the third interface roughness, the transmissivities of both low- and high-frequency phonons first decrease, and then those of low- and high-frequency phonons slightly decrease and dramatically increase, respectively. Thus many low-frequency phonons transmitting across the first and second interfaces are reflected by the third interface, causing the significant decrease of the cross-plane thermal conductivity. The above effects lead to the decrease of the cross-plane thermal conductivity of multilayer films.

For Ge/Si, when fixing two interface roughness at 0.14 nm and changing another interface roughness, as shown in Fig. 21 (b) and Fig. 22 (b), there are generally three conclusions with details as follows: (1) Increasing the first interface roughness, on the one hand, as Fig. 18 shows, the overall transmissivity of the first interface first increases and then decreases, resulting in its thermal boundary conductance and the cross-plane thermal conductivity of the multilayer film to first increase and then decrease. On the other hand, with increasing interface roughness, the transmissivities of both low- and high-frequency phonons first decrease, and then slightly decrease and dramatically increase, respectively. This means that the amount of low-frequency phonons transmitting across the first interface decreases, and that of high-frequency phonons first slightly decreases and then dramatically increases. Owing to the interface roughness is small, the transmissivities of high-frequency phonons are very small at the second and third interfaces. Thereby many high-frequency phonons transmitting across the first interface are reflected by the second and third interfaces, causing the decrease of the cross-plane thermal conductivity. The above effects lead to that the cross-plane thermal conductivity decreases at small interface roughness and increases at large interface roughness. (2) Increasing the second interface roughness, on the one hand, as Fig. 18 shows, the overall transmissivity of the second interface first increases and then decreases, resulting in its thermal boundary conductance and the cross-plane thermal conductivity of the multilayer film to first increase and then decrease. On the other hand, the transmissivities of low- and high-frequency phonons are comparable at the first interface owing to its moderate interface roughness, hence there are comparable low- and high-frequency phonons transmitting across the first interface. With increasing the second interface roughness, the transmissivities of both low- and high-frequency phonons first decrease, and then slightly decrease and dramatically increase, respectively. This makes the amounts of low- and high-frequency phonons transmitting across the second interface from the first interface first decease and then increase,

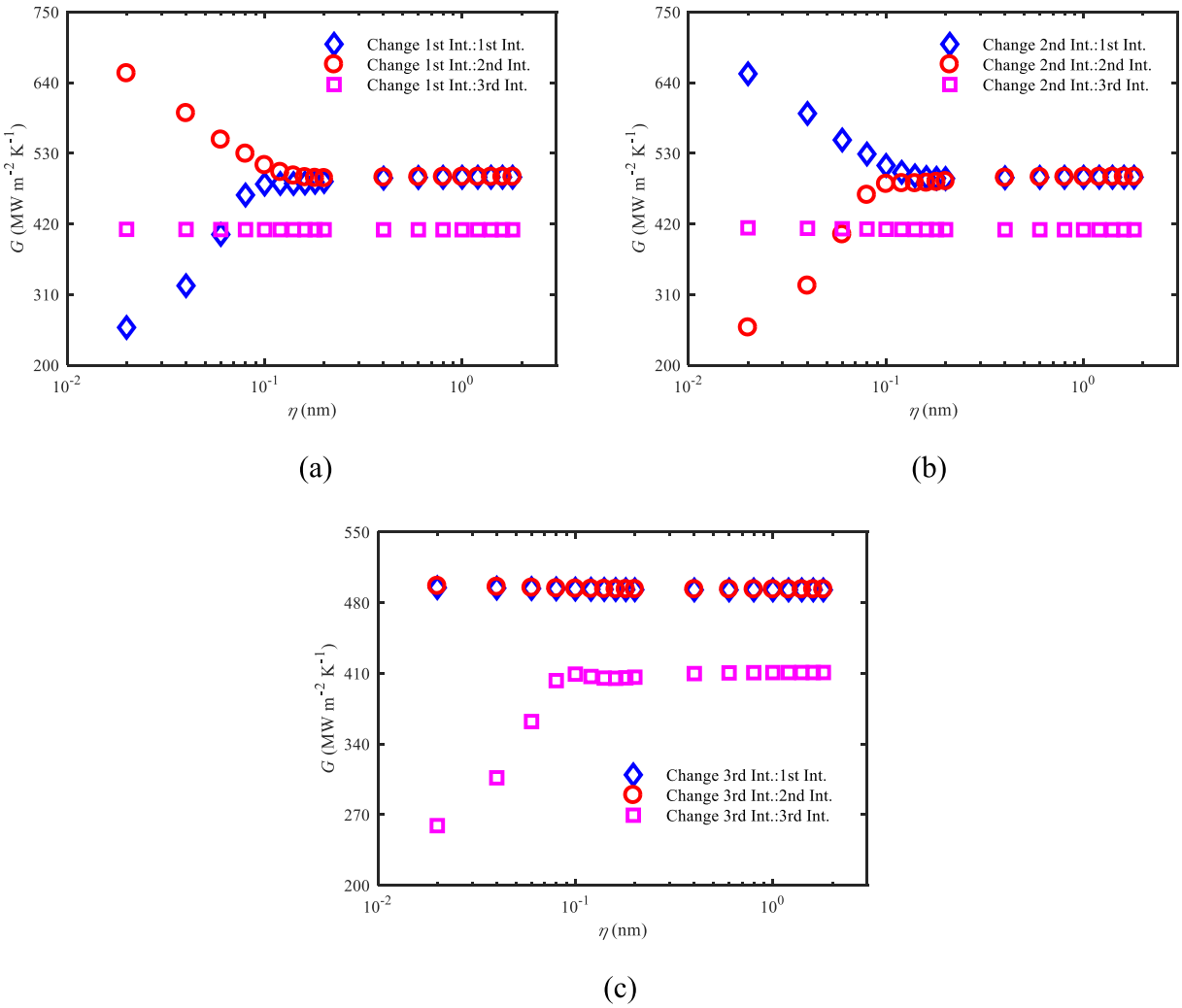

Fig. 36. The thermal boundary conductances of three interfaces in Al/Si multilayer films with the total thickness being 80 nm with the nonidentical interface roughness: (a) changing the first interface roughness and fixing two other interface roughnesses at 1.8 nm, (b) changing the second interface roughness and fixing two other interface roughnesses at 1.8 nm, and (c) changing the third interface roughness and fixing two other interface roughnesses at 1.8 nm.

causing the cross-plane thermal conductivity to first decrease and then increase. The above effects lead to the cross-plane thermal conductivity first decrease and then increase. (3) Increasing the third interface roughness, on the one hand, as Fig. 18 shows, the overall transmissivity of the third interface first increases and then decreases, resulting in its thermal boundary conductance and the cross-plane thermal conductivity of the multilayer film to first increase and then decrease. On the other hand, the transmissivities of low- and high-frequency phonons are moderate at the first and second interfaces owing to their interface roughnesses are moderate, hence the amount of low-frequency phonons transmitting across the first and second interfaces is comparable to that of high-frequency phonons. With increasing the third interface roughness, the transmissivities of both low- and high-frequency phonons first decrease, and then slightly decrease and dramatically increase, respectively. Thus the amounts of low- and high-frequency phonons transmitting across the third interface from the second interface first decease and then increase, causing a decrease followed by an increase of the cross-plane thermal conductivity. The above effects lead to the cross-plane thermal conductivity first decrease and then increase as well.

For Ge/Si, when fixing two interface roughnesses at 1.8 nm and changing another interface roughness, as shown in Fig. 21 (c) and Fig. 22 (c), there are also generally three conclusions. These conclusions and the corresponding explanation are same with the case when fixing two interface roughnesses at 0.14 nm and changing another interface roughness, hence no further elaboration is provided here. In addition, different from the Al/Si, all the present cross-plane thermal conductivities with nonidentical interface roughness of Ge/Si are larger than the cross-plane minimum thermal conductivities with the identical interface roughness. After analyses on the spectral transmissivity of Ge/Si, with the interface roughness increasing from 0 to 0.06 nm, the transmissivities of both low- and high-frequency phonons decrease, and further increasing the interface roughness, those of low- and high-frequency phonons decrease and increase, respectively. It is inferred that the interface roughness, 0.02 nm, for Al/Si should be replaced with 0.06 nm for Ge/Si. Therefore, to demonstrate the manipulation measure of the cross-plane thermal conductivity in Al/Si is still effective in Ge/Si, the interface roughnesses in Ge/Si multilayer film are reset as follows: Fixing two interface roughnesses at 0.06 nm, and changing another interface roughness. For simplicity, the case with fixing one interface roughness at 0.06 nm and changing other two interface roughnesses is not simulated here. With the same physical model, phonon properties, spatial step and isothermal boundary temperatures as before, two sizes are simulated, i.e. the total thickness being 40 nm with thickness of each layer being 10 nm and the total thickness being 80 nm with thickness of each layer being 20 nm. The results are shown in Fig. 23, and they give the minimum cross-plane thermal conductivities as 0.9777 $\left(\mathrm{W\,m^{-1}\,K^{-1}}\right)$ and 1.9101 $\left(\mathrm{W\,m^{-1}\,K^{-1}}\right)$ for the total thicknesses being 40 and 80 nm, respectively, smaller than 1.01 $\left(\mathrm{W\,m^{-1}\,K^{-1}}\right)$ and

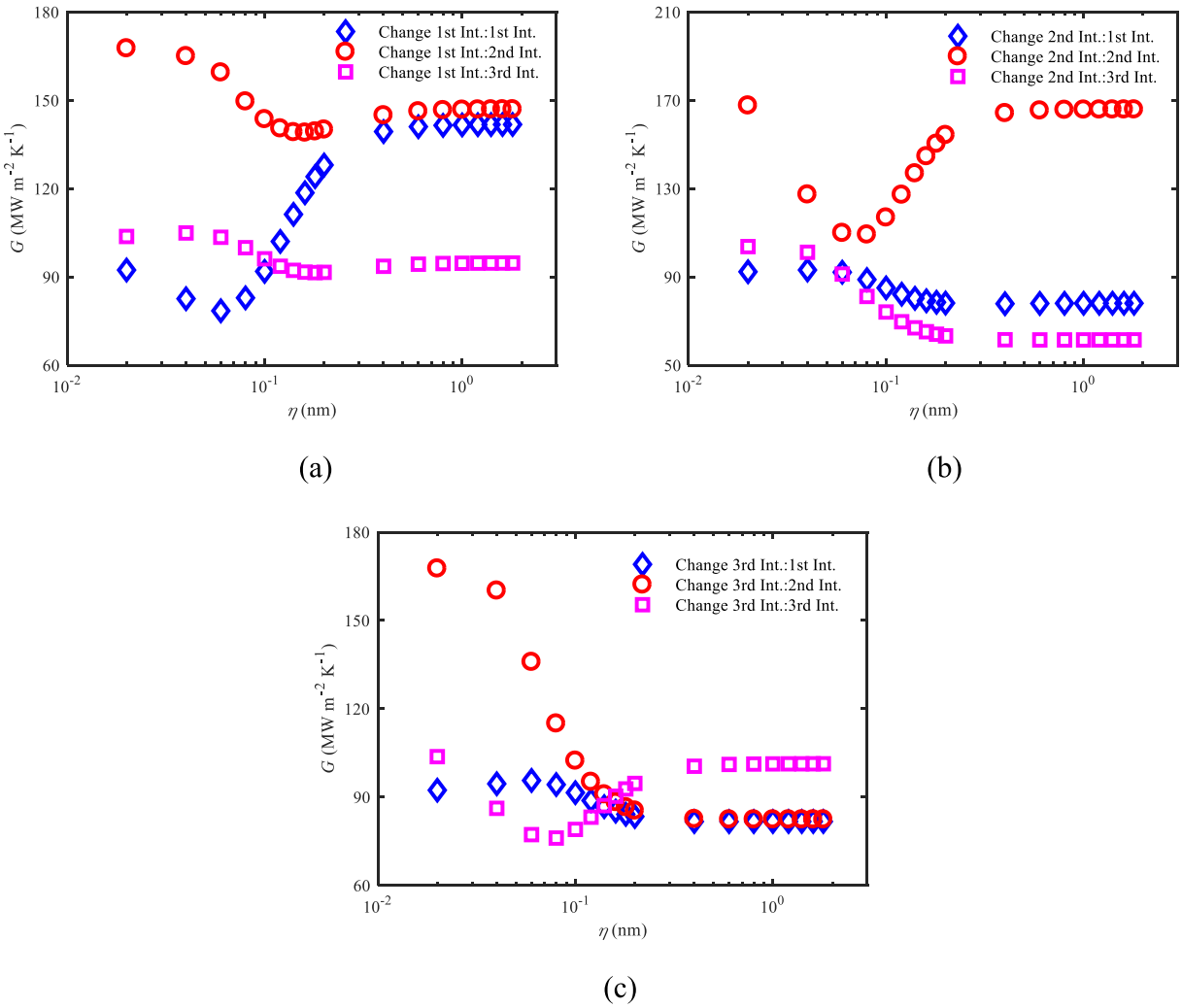

Fig. 37. The thermal boundary conductances of three interfaces in Ge/Si multilayer films with the total thickness being 40 nm with the nonidentical interface roughness: (a) changing the first interface roughness and fixing two other interface roughnesses at 0.02 nm, (b) changing the second interface roughness and fixing two other interface roughnesses at 0.02 nm, and (c) changing the third interface roughness and fixing two other interface roughnesses at 0.02 nm.

1.9664 $\left(\mathrm{W\,m^{-1}\,K^{-1}}\right)$ in Fig. 13 (d) and Fig. 14 (d). This means that the cross-plane thermal conductivity with nonidentical interface roughness can be smaller than that with the identical interface roughness, demonstrating that the previous manipulation measure is still effective in Ge/Si. The underlying mechanism is same with that for Al/Si, i.e. different roughness dependences of the spectral transmissivity at different interface roughnesses.

Finally, the above patterns of the cross-plane thermal conductivity varying with the interface roughness for Al/Si and Ge/Si also depend on the interface model adopted in the present work. Similar to the case with the identical interface roughness, when adopting the interface models considering the gray assumption, the conclusions resulted by the spectral feature of the transmissivity will be significantly different and even disappear. For instance, the patterns of cross-plane thermal conductivities varying with the interface roughness at different interfaces will be similar to each other. And the minimum cross-plane thermal conductivity will be obtained with the identical interface roughness, rather than with nonidentical interface roughness like in the present work. When considering the spectral transmissivity, elastic scattering and polarization conversion, the detailed variation of the cross-plane thermal conductivities for multilayer films with interface roughness is too difficult to be predicted in advance.

4.3. *Thermal boundary conductance with identical interface roughness*

The thermal boundary conductances in subsection 4.1 are calculated for both Al/Si and Ge/Si multilayer films. For Al/Si, the variation patterns of thermal boundary conductance with the interface roughness are similar for two total thicknesses, shown in Fig. 24, with the thermal boundary conductance of the bilayer film in Fig. 25 for comparisons. In multilayer films, the thermal boundary conductances of three interfaces first increase, and then decrease, and eventually tend to constants with increasing interface roughness. The explanation for this variation is as follows: When changing the interface roughness of three interfaces together, the variation of thermal boundary conductance of one interface is dominated by the variation of its transmissivity, similar to bilayer films. As shown in Fig. 17, the decrease of the transmissivity for low-frequency phonons is smaller and much larger than the increase of the high-frequency phonons for interface roughness from 0 to 0.06 nm and from 0.06 to 1.8 nm, respectively, which leads the thermal boundary conductance to first increase and then decrease. As shown in Fig. 24, the thermal boundary conductances of three interfaces are different at each interface roughness for both total thicknesses, that is, the thermal boundary conductances of the second, first and third interfaces decrease sequentially. To explain the difference, three types of bilayer films are introduced and shown in Fig. 26, obtained by separating the multilayer film from one of the interfaces. The difference among three films lies in

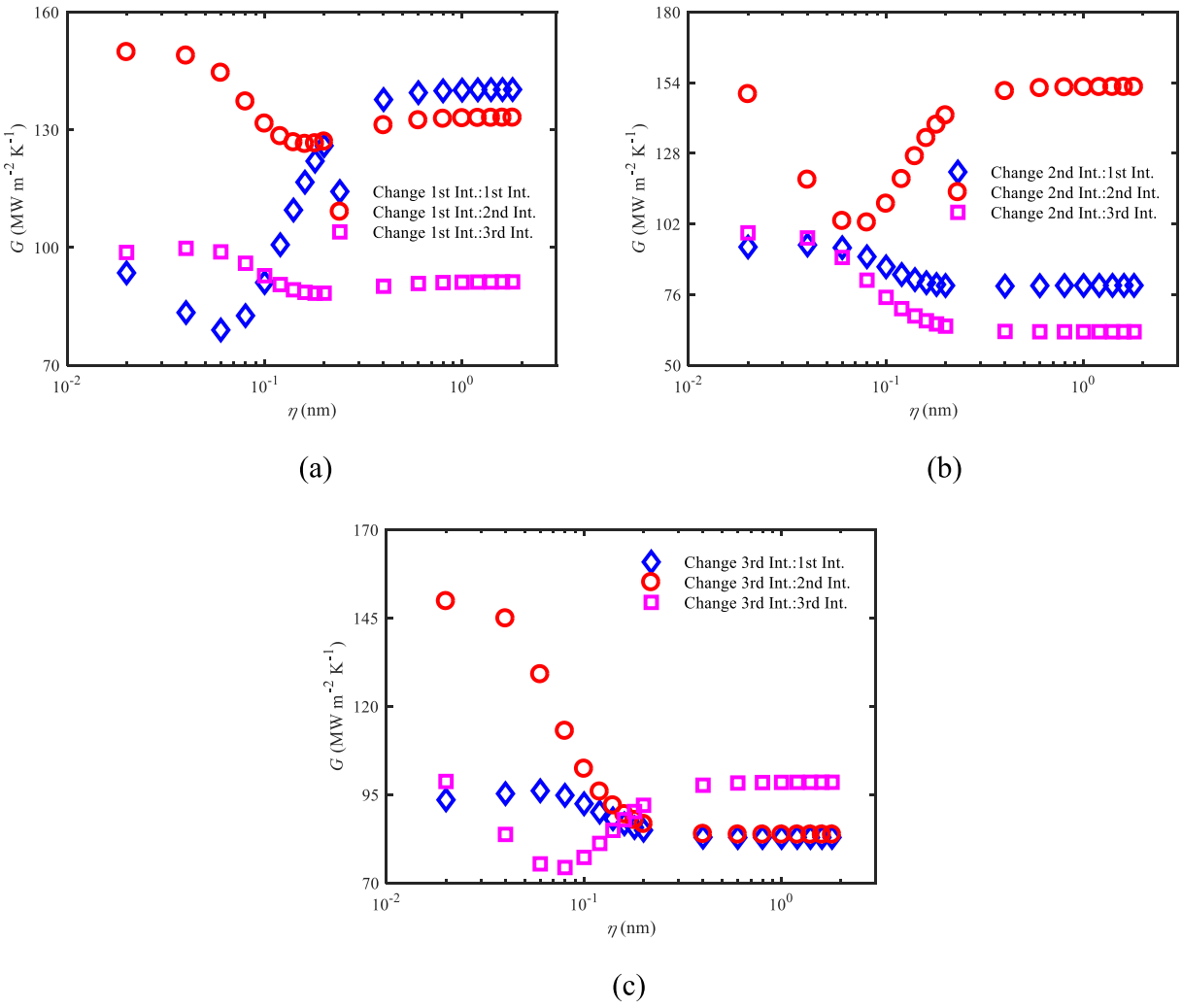

Fig. 38. The thermal boundary conductances of three interfaces in Ge/Si multilayer films with the total thickness being 80 nm with the nonidentical interface roughness: (a) changing the first interface roughness and fixing two other interface roughnesses at 0.02 nm, (b) changing the second interface roughness and fixing two other interface roughnesses at 0.02 nm, and (c) changing the third interface roughness and fixing two other interface roughnesses at 0.02 nm.

their different boundaries. Different boundaries result in different scattering strengths along the same and opposite directions of heat flux at the middle interface. The interface scattering results in the change of momentum and then poses the thermal resistance, and the stronger the interface scattering, the greater the change in momentum, and the larger the thermal resistance. And the interface scattering along the same direction of heat flux results in the increase of change of the momentum in this direction, and thus the increase of the thermal resistance and the decrease of thermal boundary conductance at the interface. On the contrary, the interface scattering along the opposite direction of heat flux results in the decrease of the momentum in this direction, and thus the decrease of the thermal resistance and the increase of the thermal boundary conductance at the interface. For the bilayer film in Fig. 26 (b), interface scattering strengths along both the same and opposite directions of heat flux at the middle interface are strong due to both the first and third interfaces reflect incident phonons. For other bilayer films in Fig. 26, Al and Si layers contact with the boundary heat sources in (a) and (c), respectively. On the one hand, since the mean free paths of phonons in Si are much larger than those in Al as shown in Fig. 27 (a), phonons emitted from the boundary heat sources in (c) are scattered more strongly at the middle interface along the same direction of heat flux than that in (a). Thereby, from this viewpoint, the thermal boundary conductance of the middle interface in Fig. 26 (c) is smaller than that in (a). On the other hand, since the transmissivities of phonons from Si to Al are larger than those from Al to Si as shown in Fig. 17, more phonons are reflected by the second interface in (c), and scattered more strongly at the middle interface along the opposite direction of heat flux than in (a). Thereby, from this viewpoint, the thermal boundary conductance of the middle interface in Fig. 26 (c) is larger than that in (a). Since the difference of the transmissivities among the phonons between two materials is smaller than that for the mean free paths of phonons for Al/Si, the effect caused by the former dominates, and thus the thermal boundary conductance of the middle interface in Fig. 26 (c) is smaller than that in (a). Totally, for Al/Si multilayer films, the thermal boundary conductances of the second and third interfaces are the largest and smallest at each interface roughness, respectively, and that of the first interface is in between.

For Ge/Si, the thermal boundary conductance also varies with the interface roughness similarly for two total thicknesses, shown in Fig. 28, with the thermal boundary conductance of the bilayer film in Fig. 29 for comparisons. In multilayer films, with increasing interface roughness, the thermal boundary conductances of three interfaces first decrease, and then increase, and eventually tend to constants. This variation can also be explained by the variation of the transmissivity with the interface roughness, similar to the Al/Si. As shown in Fig. 18, the decrease of transmissivity for both low- and high-frequency phonons leads to the decrease of the thermal boundary conductance from 0 to 0.06 nm, and then the decrease of the transmissivity for low-frequency phonons is

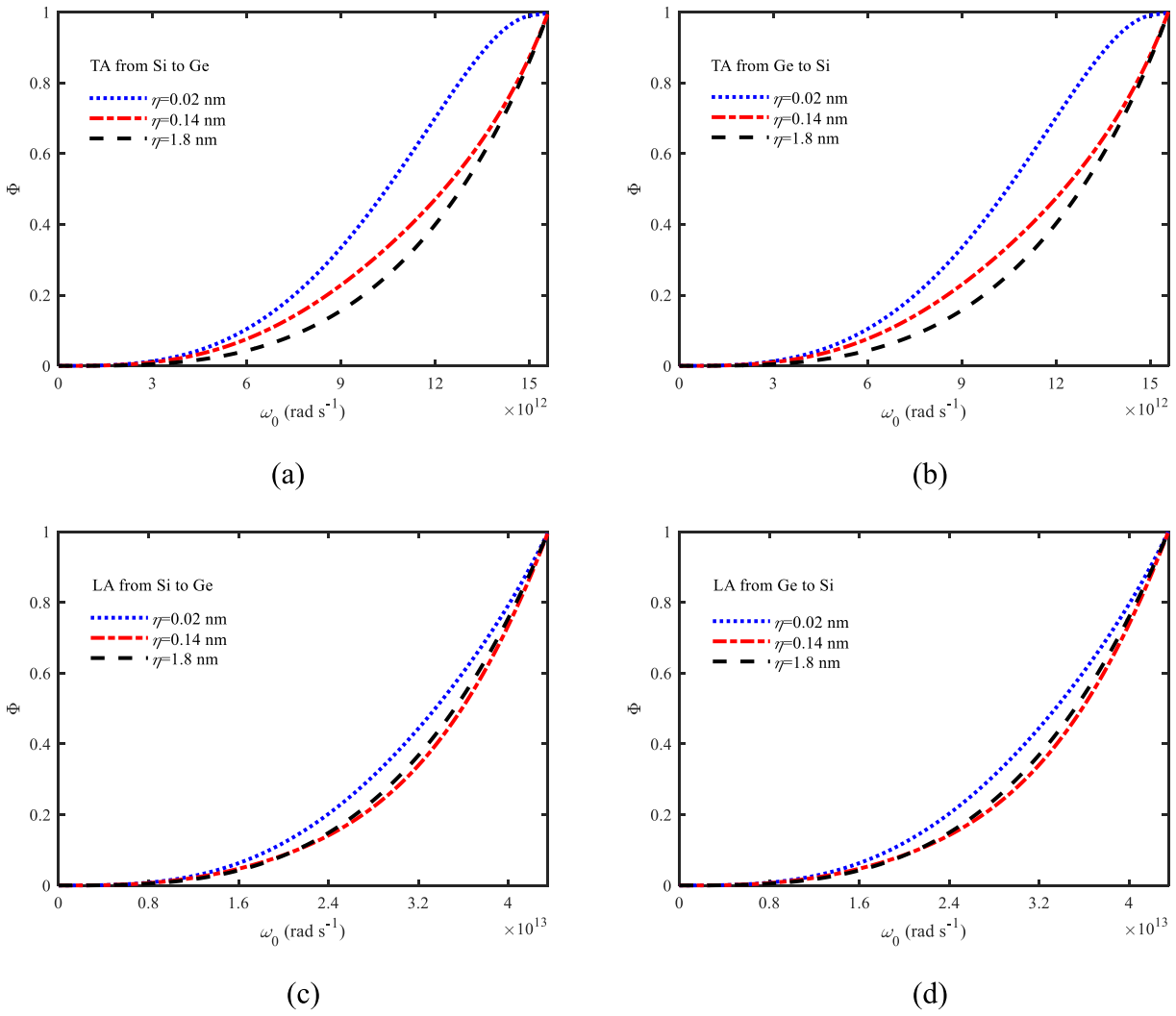

Fig. 39. The cumulative distributions of thermal boundary conductance of each polarization for Ge/Si at three interface roughnesses: (a) the transverse acoustic phonons from Si to Ge, (b) the transverse acoustic phonons from Ge to Si, (c) the longitudinal acoustic phonons from Si to Ge and (d) the longitudinal acoustic phonons from Ge to Si.

smaller than the increase of the high-frequency phonons from 0.06 to 1.8 nm, leading to the increase of the thermal boundary conductance. As shown in Fig. 28, the thermal boundary conductances of three interfaces are also different at each interface roughness for both total thicknesses, that is, the thermal boundary conductances of the second, third and first interfaces decrease sequentially at small interface roughnesses, whereas those of the second, first and third interfaces decrease sequentially at large interface roughnesses. The previous three types of bilayer films Fig. 26 are also introduced to explain these differences. Similar to Al/Si, for the bilayer film in Fig. 26 (b), interface scattering strengths along both the same and opposite directions of heat flux at the middle interface are strong owing to the reflections of incident phonons at the first and third interfaces. For the bilayer films in Fig. 26 (a) and (c), Ge and Si layers contact with the boundary heat sources in (a) and (c), respectively. On the one hand, the mean free paths of phonons in Si are larger than those in Ge as shown in Fig. 27 (b), hence the middle interface scatters the emitted phonons from the boundary heat sources more strongly in (c) along the same direction of heat flux than in (a). Thereby, from this viewpoint, the thermal boundary conductance of the middle interface in Fig. 26 (c) is smaller than that in (a). On the other hand, since the transmissivities of phonons from Si to Ge are much larger than those from Ge to Si as shown in Fig. 18, the second interface in (c) reflects more phonons, and its middle interface scatters phonons more strongly at the middle interface along the opposite direction of heat flux than in (a). Thereby, from this viewpoint, the thermal boundary conductance of the middle interface in Fig. 26 (c) is larger than that in (a). At small interface roughnesses, the difference for the transmissivity of phonons between two materials is larger than that for the mean free paths and the effect caused by the latter dominates. Hence the thermal boundary conductance of the middle interface in Fig. 26 (a) is smaller than that in (c). Whereas at large interface roughness, the difference of the transmissivities among the phonons between two materials is smaller than that for the mean free paths and the effect caused by the former dominates. Hence the thermal boundary conductance of the middle interface in Fig. 26 (c) is smaller than that in (a). Totally, for Ge/Si multilayer film at small interface roughnesses, the thermal boundary conductances of the second and first interfaces are the largest and smallest, respectively, and that of the third interface is in between. Whereas at large interface roughnesses, the thermal boundary conductance of the second and third interfaces are the largest and smallest, respectively, and that of the first interface is in between.

Finally, the above patterns of thermal boundary conductance varying with the interface roughness for Al/Si and Ge/Si are dependent on the interface model adopted in the present work. Similar to the cases for the cross-plane thermal conductivity, take two most typical and different interface scattering mechanisms here as the comparisons as well. When

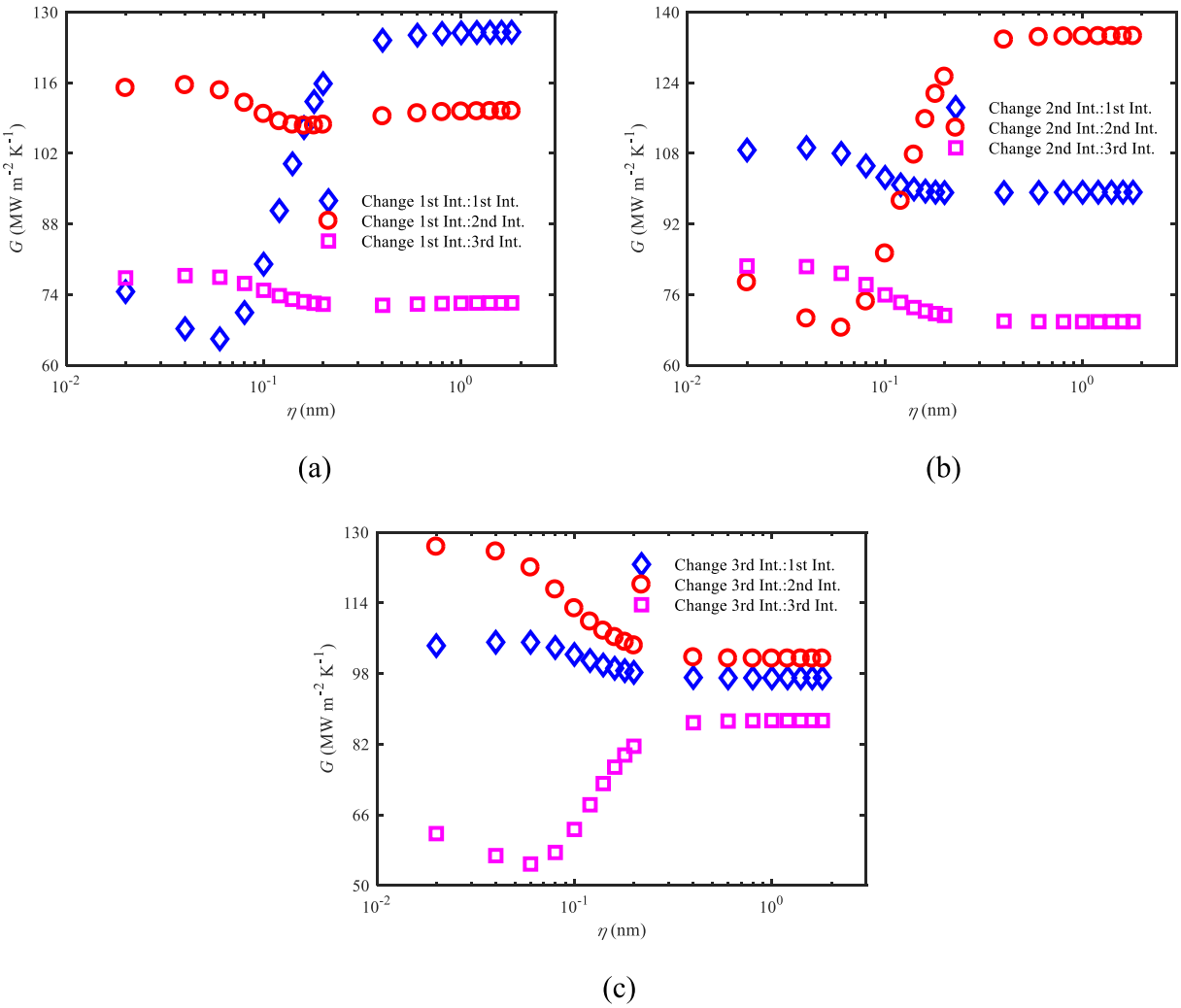

Fig. 40. The thermal boundary conductances of three interfaces in Ge/Si multilayer films with the total thickness being 40 nm with the nonidentical interface roughness: (a) changing the first interface roughness and fixing two other interface roughnesses at 0.14 nm, (b) changing the second interface roughness and fixing two other interface roughnesses at 0.14 nm, and (c) changing the third interface roughness and fixing two other interface roughnesses at 0.14 nm.

adopting the interface models considering the gray assumption, the variation patterns of thermal boundary conductances at different interfaces, and their sizes and size relationships should be different from the present calculations with the details to be predicted in advance difficultly. When considering the spectral transmissivity, elastic scattering and polarization conversion, this interface mechanism is very complicated, causing the detailed variation patterns of the thermal boundary conductances for multilayer films with the interface roughness too difficultly to be predicted in advance.

4.4. Thermal boundary conductance with nonidentical interface roughness

The thermal boundary conductances in subsection 4.2 are calculated for both Al/Si and Ge/Si multilayer films. The results of Al/Si multilayer films with changing one interface roughness and fixing two other interface roughnesses at 0.02 nm are given in Figs. 30 and 31 for both total thicknesses being 40 and 80 nm, respectively. Overall, the results are divided into three aspects.

(1) When increasing the first interface roughness shown in Fig. 30 (a) and Fig. 31 (a), the thermal boundary conductance of the first interface first increases, and then slightly decreases, and eventually tends to a constant. That of the second interface first decreases and then tends to a constant, and that of the third interface almost keeps constant. The corresponding explanation is given as follows: Increasing the first interface roughness, its thermal boundary conductance is dominated by its own transmissivity, which gives the first increase and then decrease of thermal boundary conductance. To explain the variation patterns of other two interfaces, the cumulative distribution of thermal boundary conductance is introduced:

$$\Phi = \frac{\int_0^{\omega_0} \int_0^{\frac{\pi}{2}} C_{\omega,\mathrm{p},1} v_{\mathrm{g},1}(\omega,\mathrm{p}) \alpha_{12}(\omega,\mathrm{p},\theta) \sin\theta \cos\theta d\theta d\omega}{\int_0^{\omega_{\max,\mathrm{p},1}} \int_0^{\frac{\pi}{2}} C_{\omega,\mathrm{p},1} v_{\mathrm{g},1}(\omega,\mathrm{p}) \alpha_{12}(\omega,\mathrm{p},\theta) \sin\theta \cos\theta d\theta d\omega}. \tag{78}$$

This distribution represents the contribution ratio of phonons with frequency less than ω_0 and polarization p to the total thermal boundary conductance contributed from phonons with polarization p. And as Fig. 32 shows, the main contribution on thermal boundary conductance of the second interface is from high-frequency phonons, with transmissivities increasing with increasing the first interface roughness. Thus more high-frequency phonons transport across the first interface and are scattered by the second interface, leading to the decrease of thermal boundary conductance of the second interface. The third interface is farthest from the first interface and minimally affected, hence its thermal conductance almost keeps constant.

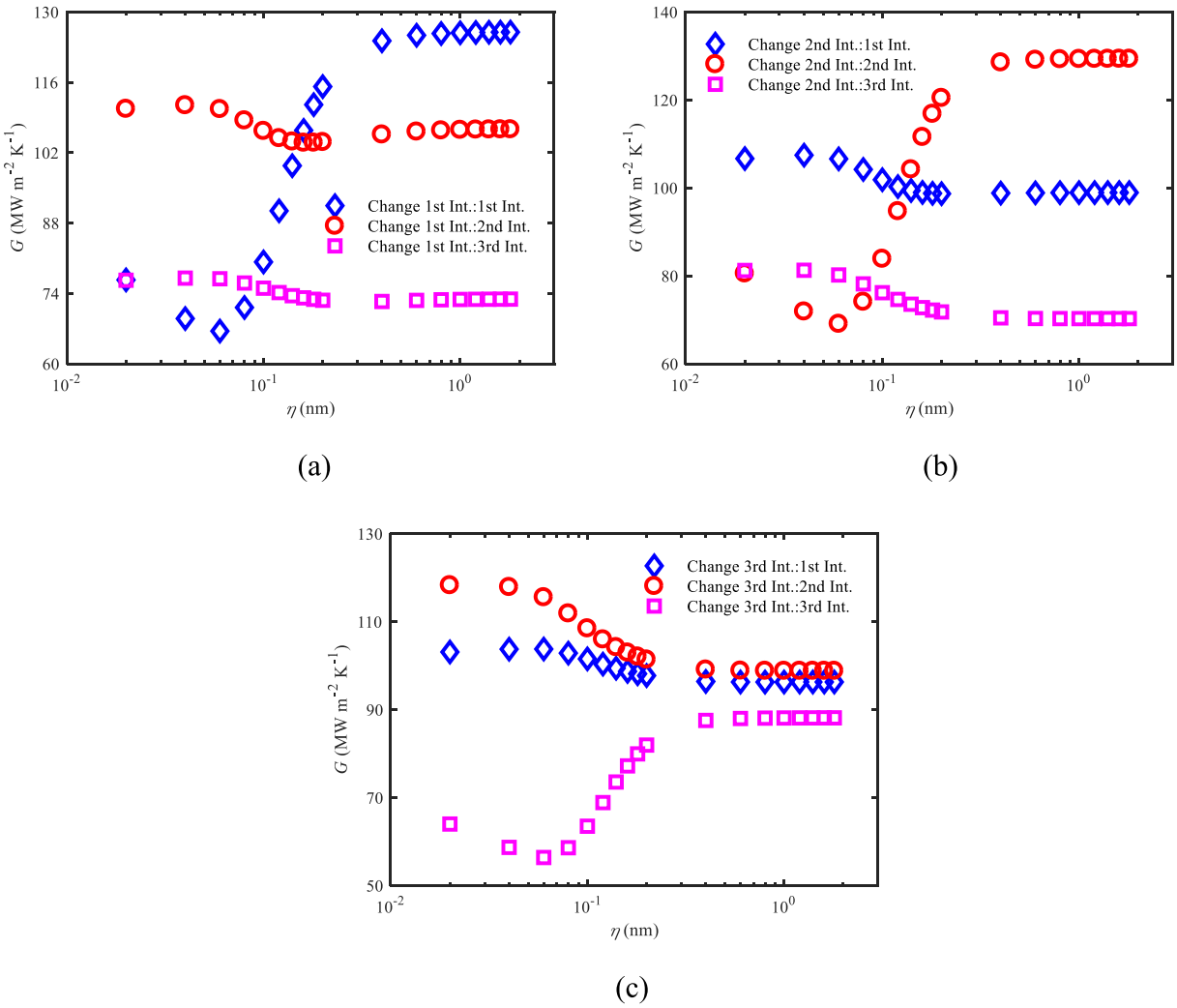

Fig. 41. The thermal boundary conductances of three interfaces in Ge/Si multilayer films with the total thickness being 80 nm with the nonidentical interface roughness: (a) changing the first interface roughness and fixing two other interface roughnesses at 0.14 nm, (b) changing the second interface roughness and fixing two other interface roughnesses at 0.14 nm, and (c) changing the third interface roughness and fixing two other interface roughnesses at 0.14 nm.

(2) When increasing the second interface roughness shown in Fig. 30 (b) and Fig. 31 (b), the thermal boundary conductance of the second interface also first increases, and then slightly decreases, and eventually tends to a constant. That of the first interface first decreases and then tends to a constant, and that of the third interface slightly decreases. The corresponding explanation is given as follows: Increasing the second interface roughness, its thermal boundary conductance is mainly affected by its own transmissivity, giving the first increase and then decrease of thermal boundary conductance. And as Fig. 32 shows, the main contribution on thermal boundary conductance is from high-frequency phonons, with transmissivities increasing with increasing the second interface roughness. Thus less high-frequency phonons are reflected by the second interface and scattered at the first interface along the opposite direction of heat flux, leading to the decrease of thermal boundary conductance of the first interface. Whereas for the third interface, more high-frequency phonons transport across the second interface and are scattered along the same direction of heat flux, leading to the slight decrease of its thermal boundary conductance.

(3) When increasing the third interface roughness shown in Fig. 30 (c) and Fig. 31 (c), same with before, the thermal boundary conductance of the third interface first increases, and then slightly decreases, and eventually tends to a constant. Those of the first and third interfaces decrease and slightly decrease, respectively. The corresponding explanation is given as follows: Increasing the third interface roughness, its own transmissivity is the leading factor of its thermal boundary conductance, resulting in the first increase and then decrease of thermal boundary conductance. And as Fig. 32 shows, the main contribution on thermal boundary conductance is from high-frequency phonons, with transmissivities increasing with increasing the third interface roughness. Thus less high-frequency phonons are reflected by the third interface and scattered at the first and second interfaces along the opposite direction of heat flux, which results in decrease and slight decrease of thermal boundary conductance of the first and second interfaces, respectively.

Figs. 33 and 34 present the results of Al/Si multilayer films with changing one interface roughness and fixing two other interface roughnesses at 0.14 nm for the total thicknesses being 40 and 80 nm, respectively, and Figs. 35 and 36 present those with changing one interface roughness and fixing two other interface roughnesses at 1.8 nm. The results are also divided into three aspects: (1) When increasing the first interface roughness shown in Fig. 33 (a) and Fig. 34 (a), or in Fig. 35 (a) and Fig. 36 (a), the thermal boundary conductance of the first interface first increases, and then slightly decreases, and eventually tends to a constant. That of the second interface first decreases and then

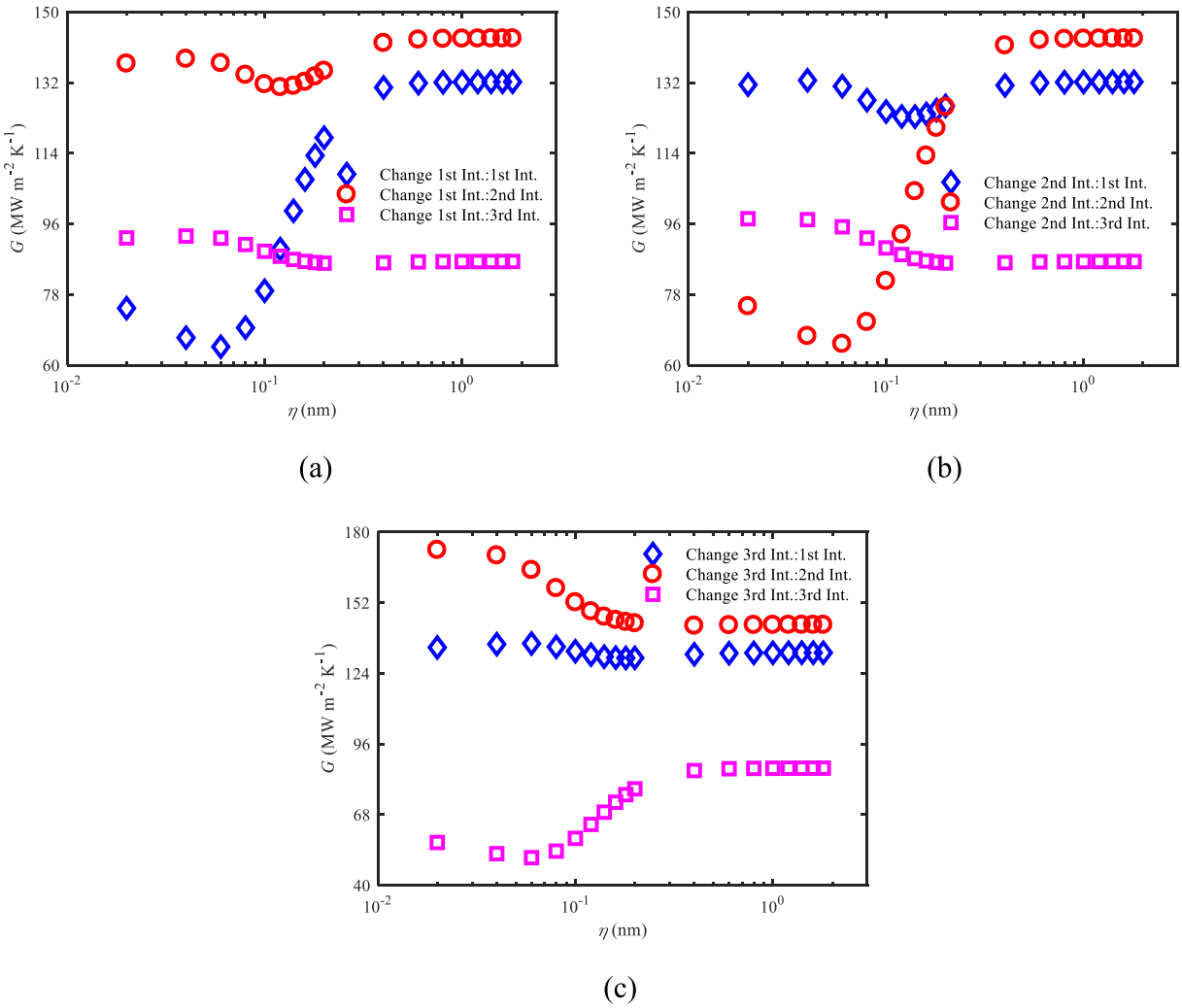

Fig. 42. The thermal boundary conductances of three interfaces in Ge/Si multilayer films with the total thickness being 40 nm with the nonidentical interface roughness: (a) changing the first interface roughness and fixing two other interface roughnesses at 1.8 nm, (b) changing the second interface roughness and fixing two other interface roughnesses at 1.8 nm, and (c) changing the third interface roughness and fixing two other interface roughnesses at 1.8 nm.

tends to a constant, and that of the third interface almost keeps constant. (2) When increasing the second interface roughness shown in Fig. 33 (b) and Fig. 34 (b), or in Fig. 35 (b) and Fig. 36 (b), the thermal boundary conductance of the second interface also first increases, and then slightly decreases, and eventually tends to a constant. That of the first interface first decreases and then tends to a constant, and that of the third interface slightly decreases. (3) When increasing the third interface roughness shown in Fig. 33 (c) and Fig. 34 (c), or in Fig. 35 (c) and Fig. 36 (c), same with before, the thermal boundary conductance of the third interface first increases, and then slightly decreases, and eventually tends to a constant. Those of the first and third interfaces decrease and slightly decrease, respectively. The explanation for the above variation patterns is same with the cases with changing one interface roughness and fixing two other interface roughnesses at 0.02 nm. Totally, the variation in one interface roughness changes its own transmissivity, which dominates the variation of the thermal boundary conductance of this interface and affect those of other interfaces.

The results of Ge/Si multilayer films with changing one interface roughness and fixing two other interface roughnesses at 0.02 nm are given in Figs. 37 and 38 for both total thicknesses being 40 and 80 nm, respectively. Overall, the results are divided into three aspects.

(1) When increasing the first interface roughness shown in Fig. 37 (a) and Fig. 38 (a), the thermal boundary conductance of the first interface first decreases, and then dramatically increases, and eventually tends to a constant. That of the second interface first slightly decreases, and then dramatically decreases, and next slightly increases, and eventually tends to a constant. And that of the third interface first slightly increases, and then decreases, and eventually tends to a constant. The corresponding explanation is given as follows: Increasing the first interface roughness, its own transmissivity dominates its thermal boundary conductance, giving the variation pattern of its thermal boundary conductance with interface roughness above. For the other two interfaces, the cumulative distribution of thermal boundary conductance in Eq. (78) for Ge/Si is also introduced to explain the variation patterns. And as Fig. 39 shows, the main contribution on thermal boundary conductance is from high-frequency phonons, with transmissivities first decreasing and then increasing when increasing the first interface roughness. Thus at small interface roughnesses, on the one hand, less high-frequency phonons transport across the first interface and are scattered by the second interface, leading to the increase of thermal boundary conductance of the second interface. On the other hand, less high-frequency phonons are reflected by the third interface and scattered at the second interface along the opposite direction of heat flux, leading to the decrease of thermal boundary conductance. Two effects above cause the thermal boundary conductance of the second interface

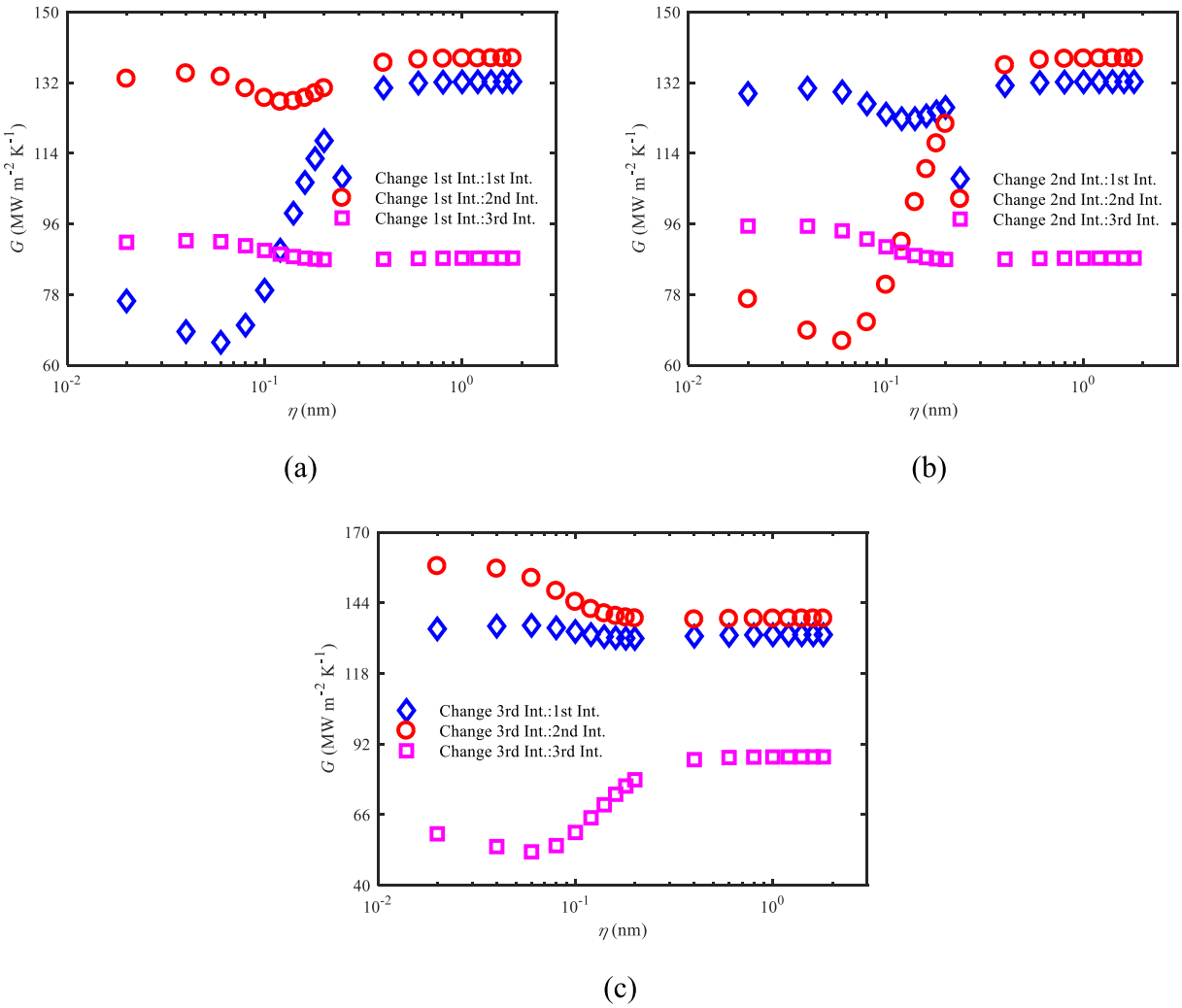

Fig. 43. The thermal boundary conductances of three interfaces in Ge/Si multilayer films with the total thickness being 80 nm with the nonidentical interface roughness: (a) changing the first interface roughness and fixing two other interface roughnesses at 1.8 nm, (b) changing the second interface roughness and fixing two other interface roughnesses at 1.8 nm, and (c) changing the third interface roughness and fixing two other interface roughnesses at 1.8 nm.

to slightly decrease at small interface roughnesses. And further increasing the first interface roughness, the transmissivity of high-frequency phonons increases a lot, and the first effect becomes more and more significant, leading to the dramatic increase of thermal boundary conductance. At large interface roughnesses, the transmissivities of all phonons are almost unchanged, hence the thermal boundary conductance tends to a constant. For the third interface, since the amount of high-frequency phonons first decreases and then increases, the scattering strength at this interface along the same direction of heat flux first decreases and then increases, leading to the first increase and then decrease of its thermal boundary conductance.

(2) When increasing the second interface roughness shown in Fig. 37 (b) and Fig. 38 (b), the thermal boundary conductance of the second interface also first decreases, and then dramatically increases, and eventually tends to a constant. That of the first interface first slightly increases, and then decreases, and eventually tends to a constant. And that of the third interface first slightly decreases, and then decreases, and eventually tends to a constant. The corresponding explanation is given as follows: Increasing the second interface roughness, its thermal boundary conductance is mainly affected by its own transmissivity, giving the variation pattern of its thermal boundary conductance with the interface roughness above. And as Fig. 39 shows, the main contribution on thermal boundary conductance is from high-frequency phonons, with transmissivities first decreasing and then increasing when increasing the second interface roughness. Thus at small interface roughnesses, high-frequency phonons are reflected by the second interface and scattered at the first interface along the opposite direction of heat flux, leading to the thermal boundary conductance of the first interface to slightly increase. And further increasing the second interface roughness, the transmissivity of high-frequency phonons increases a lot and less high-frequency phonons are reflected by the second interface and scattered at the first interface along the opposite direction of heat flux, leading to the decrease of thermal boundary conductance of the first interface. At large interface roughnesses, the almost unchanged transmissivities of all phonons cause that the thermal boundary conductance tends to a constant. For the third interface at small interface roughnesses, since the transmissivities of high-frequency phonons at the second interface are small, few phonons are reflected by the second interface and scattered at the third interface along the same direction of heat flux, leading to the thermal boundary conductance of the third interface to decrease. At large interface roughnesses, the transmissivities of high-frequency phonons at the second interface are large and many phonons transport across the second interface and scattered at the third interface along the same direction of heat flux,

leading to the thermal boundary conductance of the third interface to decrease.

(3) When increasing the third interface roughness shown in Fig. 37 (c) and Fig. 38 (c), same with before, the thermal boundary conductance of the third interface first decreases, and then increases, and eventually tends to a constant. That of the first interface first increases, and then decreases, and eventually tends to a constant. That of the second interface first dramatically decreases, and then tends to a constant. The corresponding explanation is given as follows: Increasing the third interface roughness, its own transmissivity is the leading factor of its thermal boundary conductance, resulting in the first decrease and then increase of thermal boundary conductance. And as Fig. 39 shows, the high-frequency phonons also contribute more to thermal boundary conductance, with transmissivities first decreasing and then increasing when increasing the third interface roughness. The amount of high-frequency phonons reflected by the third interface and scattered by the first interface along the opposite direction of heat flux first increases and then decreases. Thus the thermal boundary conductance of the first interface first increases and then decreases. At large interface roughnesses, the almost unchanged transmissivities of all phonons give the almost unchanged thermal boundary conductance. For the second interface at small interface roughnesses, many high-frequency phonons are reflected by the third interface and transport across the second interface. Then they are more likely reflected by the first interface back to be scattered at the second interface along the same direction of heat flux owing to the transmissivity at the first interface is small, leading to the thermal boundary conductance of the second interface to decrease. Further increasing the third interface roughness, the transmissivities of high-frequency phonons increase a lot. Thus few phonons are reflected by the third interface back to be scattered by the second interface, continually decreasing the thermal boundary conductance of the second interface. At large interface roughnesses, the almost unchanged transmissivities of all phonons also give the almost unchanged thermal boundary conductance.

Figs. 40 and 41 present the results of Ge/Si multilayer films with changing one interface roughness and fixing two other interface roughnesses at 0.14 nm for the total thicknesses being 40 and 80 nm, respectively, and Figs. 42 and 43 present those with changing one interface roughness and fixing two other interface roughnesses at 1.8 nm. Altogether, the results are also divided into three aspects: (1) When increasing the first interface roughness shown in Fig. 40 (a) and Fig. 41 (a), or in Fig. 42 (a) and Fig. 43 (a), the thermal boundary conductance of the first interface first decreases, and then dramatically increases, and eventually tends to a constant. That of the second interface first slightly increases, and then decreases, and next increases, and eventually tends to a constant. And that of the third interface first slightly increases, and then decreases, and eventually tends to a constant. (2) When increasing the second interface roughness shown in Fig. 40 (b) and Fig. 41 (b), or in Fig. 42 (b) and Fig. 43 (b), the thermal boundary conductance of the second interface also first decreases, and then dramatically increases, and eventually tends to a constant. That of the first interface first slightly increases, and then decreases, and next increases, and eventually tends to a constant. And that of the third interface first slightly decreases, and then decreases, and eventually tends to a constant. (3) When increasing the third interface roughness shown in Fig. 40 (c) and Fig. 41 (c), or in Fig. 42 (c) and Fig. 43 (c), same with before, the thermal boundary conductance of the third interface first decreases, and then increases, and eventually tends to a constant. That of the first interface first slightly increases, and then slightly decreases, and eventually tends to a constant. That of the second interface first decreases, and then tends to a constant. The explanation for the above variation patterns is same with the cases with changing one interface roughness and fixing two other interface roughnesses at 0.02 nm. Totally, the variation in one interface roughness changes its own transmissivity, which dominates the variation of the thermal boundary conductance of this interface and affect those of other interfaces.

Finally, the above patterns of thermal boundary conductance varying with the interface roughness for Al/Si and Ge/Si are also dependent on the interface model adopted in the present work. Similar to all above cases, take two most typical and different interface scattering mechanisms here as the comparisons as well. When adopting the interface models considering the gray assumption, the sizes and size relationships of thermal boundary conductance at different interfaces should be much different from the present calculations, since the spectral feature of their transmissivities disappears. When considering the spectral transmissivity, elastic scattering and polarization conversion, as concluded above, the result will be very complicated and the detailed variation of the thermal boundary conductances for multilayer films with the interface roughness is too difficult to be predicted in advance.

5. Conclusions

In summary, the present work has investigated the impact of interface roughness on cross-plane interfacial phonon transport in multilayer films with DOM. First, DOM schemes for interface treatement considering the spectral specularity and spectral transmissivity, and for cross-plane interfacial phonon transport across multilayer films are developed, and validated against Landauer formalism and experiments, and against MC, respectively. Then the roughness dependence of cross-plane interfacial phonon transport in multilayer films is studied by DOM with the validated schemes. Both cross-plane thermal conductivity and thermal boundary conductance are calculated in multilayer films with the identical and nonidentical interface roughnesses, mainly containing two aspects.

(1) Considering the identical interface roughness, the variation pattern of the cross-plane thermal conductivity of multilayer films with the roughness is similar to that of bilayer films. The size relationship between the cross-plane thermal conductivities of multilayer films at small and large interface roughnesses is different from that of bilayer films. This phenomenon is explained by the trends of the spectral transmissivity of low- and high-frequency phonons varying with the interface roughness. Considering the nonidentical interface roughness, there is a significant difference in the trend of the cross-plane thermal conductivity of multilayer films with changing the roughness of different interfaces. This is also attributed to the different trends of the spectral transmissivity of low- and high-frequency phonons varying with the interface roughness. Consequently, setting the nonidentical interface roughness is proposed to more effectively manipulate the cross-plane thermal conductivity of multilayer films, compared with the identical interface roughness.

(2) Considering the identical interface roughness, the variation of thermal boundary conductance of one interface is dominated by the variation of its roughness. The thermal boundary conductances of these interfaces are different at various interface roughnesses even for the same material pair. This phenomenon is attributed to different interface scattering strengths along the same and opposite directions of heat flux, caused by the different mean free paths of phonons in each material and different transmissivities in two directions. Considering the nonidentical interface roughness, the thermal boundary conductance of one interface varies with its roughness, and those of other interfaces are affected even their roughnesses are not changed. After analyses, the variation pattern of thermal boundary conductance of one interface is found to be mainly affected by the variation of its own roughness, determining the variation pattern of its transmissivity with the phonon frequency, similar to bilayer films.

Meanwhile the variation patterns of thermal boundary conductance of other interfaces are found to be affected by multiple reflections and transmissions at multiple interfaces when changing one interface roughness, which is a special process in multilayer films, different from bilayer films.

CRediT authorship contribution statement

Xin Ran: Writing – original draft, Validation, Investigation. **Bingyang Cao:** Writing – review & editing, Supervision, Project administration, Conceptualization.

Declaration of competing interest

The authors declare that they have no known competing financial interests or personal relationships that could have appeared to influence the work reported in this paper.

Acknowledgements

This study was financially supported by the National Natural Science Foundation of China (Nos. 52425601, 52327809), National Key Research and Development Program of China (No. 2023YFB4404104), and Beijing Natural Science Foundation (No. L233022).

Data availability

Data will be made available on request.

References

[1] M. Ahmad, K. Agarwal, S.G. Munoz, A. Ghosh, N. Kodan, O.V. Kolosov, B.R. Mehta, Engineering interfacial effects in electron and phonon transport of Sb2Te3/MoS2 multilayer for thermoelectric ZT above 2.0, Adv. Funct. Mater. 32 (49) (2022) 2206384, https://doi.org/10.1002/adfm.202206384.
[2] J. Chen, X. Xu, J. Zhou, B. Li, Interfacial thermal resistance: past, present, and future, Rev. Mod. Phys. 94 (2) (2022) 025002, https://doi.org/10.1103/RevModPhys.94.025002.
[3] X. Zhao, W. Hu, Progress in the semiconductor/diamond heterogeneous integrations: technical methods, interfacial phonon transport, and thermal characterizations, Surf. Interfaces 46 (2024) 104178, https://doi.org/10.1016/j.surfin.2024.104178.
[4] C. Chang, L.-D. Zhao, Anharmoncity and low thermal conductivity in thermoelectrics, Mater. Today Phys. 4 (2018) 50–57, https://doi.org/10.1016/j.mtphys.2018.02.005.
[5] Y.-C. Hua, Y. Shen, Z.-L. Tang, D.-S. Tang, X. Ran, B.-Y. Cao, Near-junction thermal managements of electronics, in: J.P. Abraham, J.M. Gorman, W.J. Minkowycz (Eds.), Advances in Heat Transfer, Elsevier, Amsterdam, 2023.
[6] I. Al Keyyam, X. Wang, Generalization of interfacial thermal conductance based on interfacial phonon localization, Mater. Today Phys. 46 (2024) 101516, https://doi.org/10.1016/j.mtphys.2024.101516.
[7] B.-Y. Cao, Non-Fourier Heat Conduction in Nanostrucutres, Science Press, Beijing, 2023.
[8] W. Little, The transport of heat between dissimilar solids at low temperatures, Can. J. Phys. 37 (3) (1959) 334–349, https://doi.org/10.1139/p59-037.
[9] E.T. Swartz, R.O. Pohl, Thermal boundary resistance, Rev. Mod. Phys. 61 (3) (1989) 605–668, https://doi.org/10.1103/RevModPhys.61.605.
[10] G. Chen, Thermal conductivity and ballistic-phonon transport in the cross-plane direction of superlattices, Phys. Rev. B 57 (23) (1998) 14958, https://doi.org/10.1103/PhysRevB.57.14958.
[11] C. Hua, X. Chen, N.K. Ravichandran, A.J. Minnich, Experimental metrology to obtain thermal phonon transmission coefficients at solid interfaces, Phys. Rev. B 95 (20) (2017) 205423, https://doi.org/10.1103/PhysRevB.95.205423.
[12] X. Li, R. Yang, Effect of lattice mismatch on phonon transmission and interface thermal conductance across dissimilar material interfaces, Phys. Rev. B 86 (5) (2012) 054305, https://doi.org/10.1103/PhysRevB.86.054305.
[13] H.-A. Yang, B.-Y. Cao, Mode-resolved phonon transmittance using lattice dynamics: robust algorithm and statistical characteristics, J. Appl. Phys. 134 (15) (2023) 155302, https://doi.org/10.1063/5.0171201.
[14] J.-Y. Lin, M.-J. Huang, An investigation into the roughness and film thickness effects on the interfacial thermal resistance, nanoscale microscale thermophys, Eng. 27 (3–4) (2023) 149–167, https://doi.org/10.1080/15567265.2023.2240877.
[15] Y. Zhang, D. Ma, Y. Zang, X. Wang, N. Yang, A modified theoretical model to accurately account for interfacial roughness in predicting the interfacial thermal conductance, Front. Energy Res. 6 (2018) 48, https://doi.org/10.3389/fenrg.2018.00048.
[16] X. Ran, B. Cao, Roughness dependence of phonon-interface thermal transport: theoretical model and Monte Carlo simulation, Phys. Rev. B 110 (2) (2024) 024302, https://doi.org/10.1103/PhysRevB.110.024302.
[17] B. Liu, Y. Guo, V.I. Khvesyuk, A.A. Barinov, M. Wang, Heat conduction of multilayer nanostructures with consideration of coherent and incoherent phonon transport, Nano Res. 15 (10) (2022) 9492–9497, https://doi.org/10.1007/s12274-022-4589-7.
[18] J. Ravichandran, A.K. Yadav, R. Cheaito, P.B. Rossen, A. Soukiassian, S. Suresha, J. C. Duda, B.M. Foley, C.-H. Lee, Y. Zhu, Crossover from incoherent to coherent phonon scattering in epitaxial oxide superlattices, Nat. Mater. 13 (2) (2014) 168–172, https://doi.org/10.1038/nmat3826.
[19] X. Wu, Q. Han, Transition from incoherent to coherent phonon thermal transport across graphene/h-BN van der Waals superlattices, Int. J. Heat Mass Tran. 184 (2022) 122390, https://doi.org/10.1016/j.ijheatmasstransfer.2021.122390.
[20] T. Ma, Y. Wang, Ex-situ modification of lattice thermal transport through coherent and incoherent heat baths, Mater. Today Phys. 29 (2022) 100884, https://doi.org/10.1016/j.mtphys.2022.100884.
[21] A. Malhotra, K. Kothari, M. Maldovan, Cross-plane thermal conduction in superlattices: impact of multiple length scales on phonon transport, J. Appl. Phys. 125 (4) (2019) 044304, https://doi.org/10.1063/1.5065904.
[22] K. Gordiz, A. Henry, Phonon transport at interfaces between different phases of silicon and germanium, J. Appl. Phys. 121 (2) (2017) 025102, https://doi.org/10.1063/1.4973573.
[23] X. Ran, Y. Guo, Z. Hu, M. Wang, Interfacial phonon transport through Si/Ge multilayer film using Monte Carlo scheme with spectral transmissivity, Front. Energy Res. 6 (2018) 28, https://doi.org/10.3389/fenrg.2018.00028.
[24] X. Ran, M. Wang, Manipulation of effective thermal conductivity of multilayer thin film by varying thickness ratio of layers using Monte Carlo simulation, Phys. Lett. 383 (1) (2019) 58–62, https://doi.org/10.1016/j.physleta.2018.09.011.
[25] Y. Guo, Z. Zhang, M. Bescond, S. Xiong, M. Nomura, S. Volz, Anharmonic phonon-phonon scattering at the interface between two solids by nonequilibrium Green's function formalism, Phys. Rev. B 103 (17) (2021) 174306, https://doi.org/10.1103/PhysRevB.103.174306.
[26] S. Tian, T. Wu, S. Hu, D. Ma, L. Zhang, Boosting phonon transport across AlN/SiC interface by fast annealing amorphous layers, Appl. Phys. Lett. 124 (4) (2024) 042202, https://doi.org/10.1063/5.0187793.
[27] H. Ali, B.S. Yilbas, Phonon transport in silicon-diamond thin film pairs: consideration of thermal boundary resistance due to cutoff mismatch and diffusive mismatch models, Numer. Heat Transf. A Appl. 68 (12) (2015) 1307–1330, https://doi.org/10.1080/10407782.2015.1023138.
[28] J.-P.M. Péraud, C.D. Landon, N.G. Hadjiconstantinou, Monte Carlo methods for solving the Boltzmann transport equation, Annu. Rev. Heat. Transf. 17 (2014) 205–265, https://doi.org/10.1615/AnnualRevHeatTransfer.2014007381.
[29] X. Ran, Y. Huang, M. Wang, A hybrid Monte Carlo-discrete ordinates method for phonon transport in micro/nanosystems with rough interfaces, Int. J. Heat Mass Tran. 201 (2023) 123624, https://doi.org/10.1016/j.ijheatmasstransfer.2022.123624.
[30] Z. Guo, K. Xu, Discrete unified gas kinetic scheme for multiscale heat transfer based on the phonon Boltzmann transport equation, Int. J. Heat Mass Tran. 102 (2016) 944–958, https://doi.org/10.1016/j.ijheatmasstransfer.2016.06.088.
[31] X.-P. Luo, H.-L. Yi, A discrete unified gas kinetic scheme for phonon Boltzmann transport equation accounting for phonon dispersion and polarization, Int. J. Heat Mass Tran. 114 (2017) 970–980, https://doi.org/10.1016/j.ijheatmasstransfer.2017.06.127.
[32] A. Nabovati, D.P. Sellan, C.H. Amon, On the lattice Boltzmann method for phonon transport, J. Comput. Phys. 230 (15) (2011) 5864–5876, https://doi.org/10.1016/j.jcp.2011.03.061.
[33] Y. Guo, M. Wang, Lattice Boltzmann modeling of phonon transport, J. Comput. Phys. 315 (2016) 1–15, https://doi.org/10.1016/j.jcp.2016.03.041.
[34] A. Giri, P.E. Hopkins, A review of experimental and computational advances in thermal boundary conductance and nanoscale thermal transport across solid interfaces, Adv. Funct. Mater. 30 (8) (2019) 1903857, https://doi.org/10.1002/adfm.201903857.
[35] M. Wang, Z. Li, Nonideal gas flow and heat transfer in micro-and nanochannels using the direct simulation Monte Carlo method, Phys. Rev. 68 (4) (2003) 046704, https://doi.org/10.1103/PhysRevE.68.046704.
[36] R. Yang, G. Chen, Thermal conductivity modeling of periodic two-dimensional nanocomposites, Phys. Rev. B 69 (19) (2004) 195316, https://doi.org/10.1103/PhysRevB.69.195316.
[37] X. Ran, Y. Guo, M. Wang, Interfacial phonon transport with frequency-dependent transmissivity by Monte Carlo simulation, Int. J. Heat Mass Tran. 123 (2018) 616–628, https://doi.org/10.1016/j.ijheatmasstransfer.2018.02.117.
[38] J. Chen, K. Wang, Z. Wang, Simulation study of phonon transport at the GaN/AlN superlattice interface: ballistic and non-equilibrium phenomena, Int. J. Therm. Sci. 206 (2024) 109334, https://doi.org/10.1016/j.ijthermalsci.2024.109334.
[39] A. Majumdar, Microscale heat conduction in dielectric thin films, J. Heat Tran. 115 (1993) 7–16, https://doi.org/10.1115/1.2910673.
[40] B.S. Yilbas, S.B. Mansoor, Phonon transport and equivalent equilibrium temperature in thin silicon films, J. Non-Equilibrium Thermodyn. 38 (2) (2013) 153–174, https://doi.org/10.1515/jnetdy-2012-0026.
[41] X. Ran, M. Wang, Efficiency improvement of discrete-ordinates method for interfacial phonon transport by Gauss-Legendre integral for frequency domain, J. Comput. Phys. 399 (2019) 108920, https://doi.org/10.1016/j.jcp.2019.108920.
[42] M.N. Özişik, H.R. Orlande, M.J. Colaço, R.M. Cotta, Finite Difference Methods in Heat Transfer, CRC press, Boca Raton, 2017.

[43] Ge - Germanium, available from: http://www.ioffe.ru/SVA/NSM/Semicond/Ge/mechanic.html, 2021. (Accessed 1 January 2021).
[44] Si - Silicon, available from: http://www.ioffe.ru/SVA/NSM/Semicond/Si/mechanic.html, 2021. (Accessed 1 January 2021).
[45] R. Stedman, G. Nilsson, Dispersion relations for phonons in aluminum at 80 and 300°K, Phys. Rev. 145 (2) (1966) 492–500, https://doi.org/10.1103/PhysRev.145.492.
[46] X. Ran, M. Wang, In-plane interfacial phonon transport through multi-layer thin films by theoretical analyses and Monte Carlo simulations, Int. J. Heat Mass Tran. 176 (2021) 121438, https://doi.org/10.1016/j.ijheatmasstransfer.2021.121438.
[47] A.J. Minnich, G. Chen, S. Mansoor, B. Yilbas, Quasiballistic heat transfer studied using the frequency-dependent Boltzmann transport equation, Phys. Rev. B 84 (23) (2011) 235207, https://doi.org/10.1103/PhysRevB.84.235207.
[48] J.-P.M. Péraud, N.G. Hadjiconstantinou, Extending the range of validity of Fourier's law into the kinetic transport regime via asymptotic solution of the phonon Boltzmann transport equation, Phys. Rev. B 93 (4) (2016) 045424, https://doi.org/10.1103/PhysRevB.93.045424.
[49] A. Jain, A.J. McGaughey, Thermal transport by phonons and electrons in aluminum, silver, and gold from first principles, Phys. Rev. B 93 (8) (2016) 081206, https://doi.org/10.1103/PhysRevB.93.081206.
[50] Y. Guo, M. Wang, Phonon hydrodynamics and its applications in nanoscale heat transport, Phys. Rep. 595 (2015) 1–44, https://doi.org/10.1016/j.physrep.2015.07.003.
[51] A.J. Minnich, J.A. Johnson, A.J. Schmidt, K. Esfarjani, M.S. Dresselhaus, K. A. Nelson, G. Chen, Thermal conductivity spectroscopy technique to measure phonon mean free paths, Phys. Rev. Lett. 107 (9) (2011) 095901, https://doi.org/10.1103/PhysRevLett.107.095901.
[52] P. Jiang, L. Lindsay, X. Huang, Y.K. Koh, Interfacial phonon scattering and transmission loss in >1 μm thick silicon-on-insulator thin films, Phys. Rev. B 97 (19) (2018) 195308, https://doi.org/10.1103/PhysRevB.97.195308.
[53] C. Monachon, L. Weber, C. Dames, Thermal boundary conductance: a materials science perspective, Annu. Rev. Mater. Res. 46 (1) (2016) 433–463, https://doi.org/10.1146/annurev-matsci-070115-031719.
[54] J. Chen, D. Ren, H. Hsu, L. Wang, X. He, C. Zhang, X. Feng, M. Ouyang, Investigating the thermal runaway features of lithium-ion batteries using a thermal resistance network model, Appl. Energy 295 (2021) 117038, https://doi.org/10.1016/j.apenergy.2021.117038.